Reprinted from Preprint Volume: 12th Conference on Severe Local Storms, Jan. 11-15, 1982; San Antonio, Tex. Published by the American Meteorological Society, Boston, Mass.

4.15

# THUNDERSTORM TOP STRUCTURE OBSERVED BY AIRCRAFT OVERFLIGHTS WITH AN INFRARED RADIOMETER

Robert F. Adler[1], Michael J. Markus[2,1], Douglas D. Fenn[2,1], and William E. Shenk[1]

[1]Goddard Laboratory for Atmospheric Sciences, NASA/Goddard Space Flight Center, Greenbelt, MD.

[2]GE/MATSCO, Beltsville, MD.

## 1. INTRODUCTION

During SESAME 1979, thunderstorms were overflown (at 18 km) with NASA's WB-57F equipped with a three channel (visible, 6.7 micron, and 11 micron) scanning radiometer, the Cloud Top Scanner (CTS). In addition to the CTS data, cloud top height information is available from a downward pointing lidar on the same aircraft and from side views of the thunderstorms photographed every 30 seconds from a second aircraft at 14 km. Also, for the case study day discussed here (June 7, 1979), two geosynchronous satellites were operated in the short-interval (3 minute) mode in a synchronized fashion for the calculation of stereo heights.

The general objective of the study is to examine and compare the high resolution aircraft observations (primarily the 11 micron channel) with GOES measurements to better understand and interpret the satellite observations of severe thunderstorms and to help determine sensing parameters for future satellite missions. Specifically, the objectives are to: 1) determine the relation between height deviations and IR temperature deviations of overshooting thunderstorm tops; 2) determine the effect of spatial resolution on estimates of thunderstorm height and on calculations of thunderstorm top ascent rate; and 3) attempt to determine the relation of storm maximum height (as determined from satellite or aircraft) and cloud top ascent rates, to vertical velocities estimated from one-dimensional cloud model runs.

## 2. MATURE STORM CHARACTERISTICS

### 2.1 General Characteristics

Seven successive overpasses were flown over a mature thunderstorm with a ten minute return time between passes. Fig. 1 displays a summary of cloud top equivalent blackbody temperature ($T_{BB}$) as viewed from the CTS (aircraft) and satellite with other pertinent data, including maximum radar reflectivity and height information from the aircraft lidar and satellite stereo calculations. Fig. 2 shows views of the storm at the time of the first overpass (line 3) from the CTS, satellite, and the Learjet aircraft at 14 km.

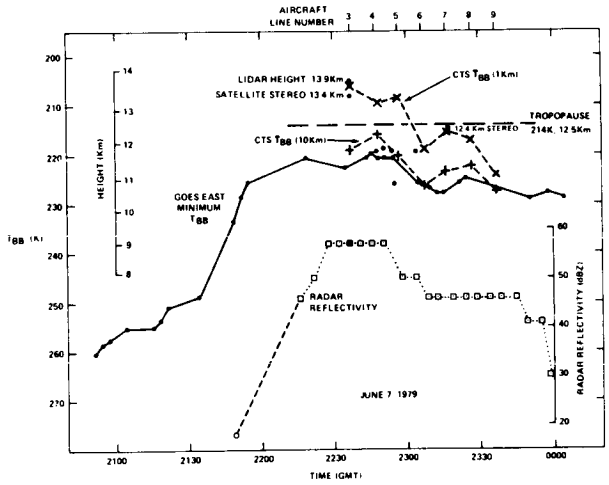


*Figure 1. Summary of equivalent blackbody temperatures ($T_{BB}$) as a function of time for mature storm.*

The storm began to build about 2140 GMT (1540 CST) an hour before the first overflight (see Fig. 1). The aircraft overflights began about the time of maximum storm intensity as indicated by the radar and satellite IR data. The CTS data are represented in Fig. 1 by spatial averages over the coldest 1 km and 10 km squares. While the satellite is indicating a minimum $T_{BB}$ of 220K, significantly warmer, or below, the tropopause, the CTS IR data is clearly indicating $T_{BB}$'s as low as 203K (-70C), with a 1 km average of 206K for line 3. These low values of $T_{BB}$ indicate thunderstorm tops significantly above the tropopause and this is verified by the aircraft lidar maximum height of 13.9 km and a satellite stereo estimate of 13.4 km. The average $T_{BB}$ over a 10 km square (approximately the satellite instantaneous field of view, IFOV) is much warmer and corresponds more closely to the satellite observation. The large satellite IFOV obviously leads to a significant underestimate of thunderstorm height.

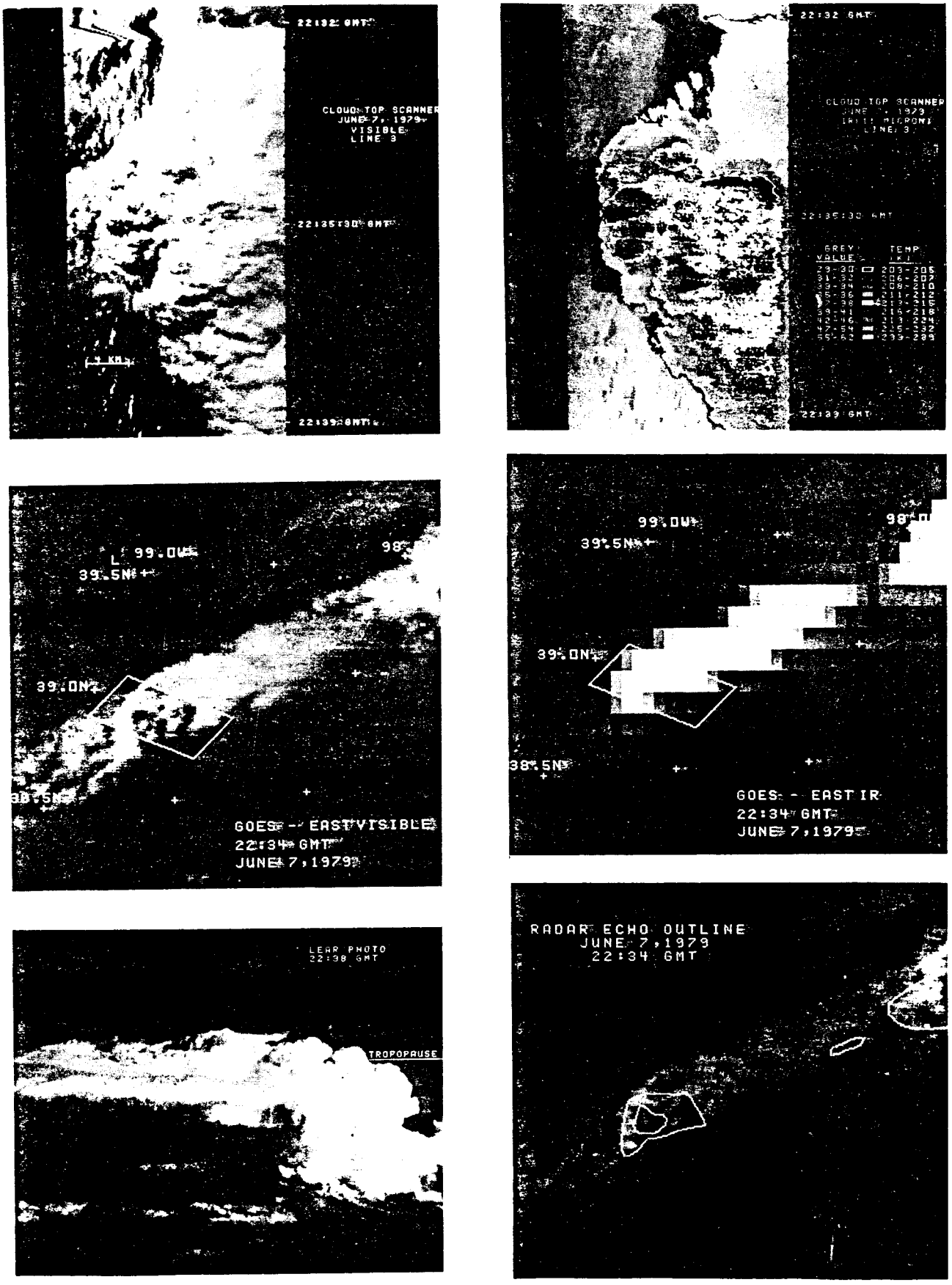


*Figure 2. Nearly simultaneous views of mature thunderstorm from aircraft overpass, geosynchronous satellite, and side-looking aircraft. Lowest $T_{BB}$ in satellite IR image is 223K.*



90B

## 2.2 Description of Line 3

Fig. 2 shows the various views of the storm at about the time of the line 3 overpass. The approximate lateral boundaries of the CTS and the position of the lower altitude aircraft (L) are displayed on the satellite images. A hand-remapped radar image is also shown.

The CTS visible image shows overshooting cumuliform features, each having its accompanying $T_{BB}$ relative minimum, or cold feature. Individual turrets observed in the CTS image can be identified in the side view photograph. The CTS data and the side look photography are clearly showing a multicell thunderstorm, although the satellite IR image has only one $T_{BB}$ minimum, because of its coarse resolution. The radar image also indicates only one rainfall core. The minimum $T_{BB}$ is 203K (-70C) at a lidar-determined height of 13.9 km (see Fig. 3), which is 11K colder than the tropopause and 5K colder than the ambient temperature at that altitude.

The downward pointing lidar gives cloud top height information along the centerline of the CTS image for comparison with the CTS IR data. Lidar data was only available for clouds above 12.8 km, i.e. above the tropopause. The lidar height-CTS $T_{BB}$ data are very well correlated (0.91) and have a regression slope of 9.2K $km^{-1}$, very close to adiabatic. The aircraft $T_{BB}$-height relation is shown in Fig. 3 as the dash-dot line above the tropopause. At temperatures colder than -60C the CTS $T_{BB}$ absolute values are accurate to approximately $\pm$2K, so it is possible the cloud top temperatures are slightly colder than indicated here. Because the cumuliform turrets are very dense, the radiation emitted from the cloud top is coming primarily from the first 100 m. Both the slope of the relation and the deviation from ambient indicate little mixing with the stratospheric environment. This appears to agree with the aircraft overpass data presented by Pitts et al. (1975) and disagrees with the ideas of Roach (1967), who postulated intense mixing at the cloud edge and cloud top $T_{BB}$'s close to ambient.

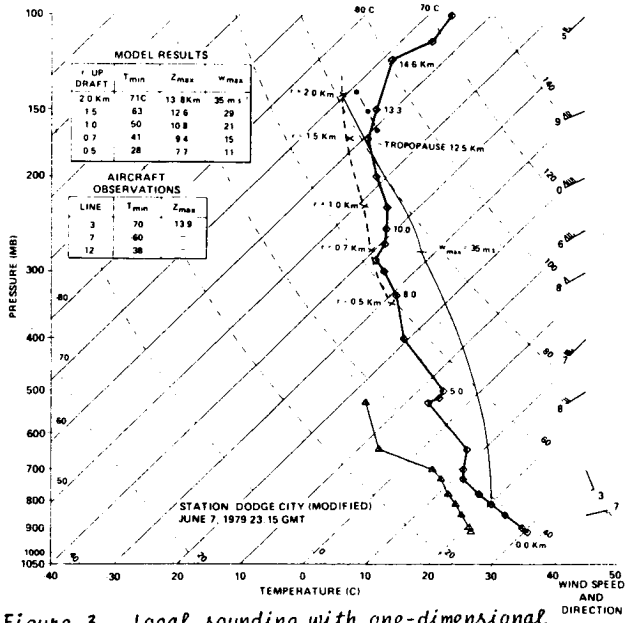


*Figure 3. Local sounding with one-dimensional model results plotted and presented in table insert.*

## 2.3 Cloud Model Analysis in Comparison to Aircraft and Satellite Observations

The aircraft overpass of line 3 was at the time of approximate maximum storm height. This is obvious from subsequent aircraft passes, although the satellite data shows minimum $T_{BB}$ 10-20 min later. A second updraft surge reached a lower maximum height at line 7 (Fig. 1), and a much weaker, separate storm (discussed in Section 4) reached about 9 km. A one-dimensional cloud model (Simpson and Wiggert, 1969) was run for various updraft radii (0.5 - 2.2 km) on the Dodge City, Kansas 2315 GMT sounding adjusted for local surface conditions in the area of the cloud (Fig. 3). The model run with an input updraft radius of 2.0 km approximately reproduces the observed maximum height (13.9 km) and minimum temperature (-70C). The solid line to the right of the temperature profile in the troposphere is the temperature trace produced by the ascending parcel in the model cloud for the 2 km radius. Because of the effect of entrainment, model clouds with smaller updraft radii grow to lower maximum heights as seen by the dashed line (to the left of the ambient temperature) which connects the maximum heights/minimum temperatures from the model runs. The cloud parcel ascends nearly adiabatically through the neutral point to its maximum height. However, when comparing different storms reaching different $T_{min}$'s, one must use a smaller lapse rate ($\sim$7K $km^{-1}$) to convert to height variations. A knowledge of the actual cloud top $T_{min}$ can be converted to height by using the dashed curve, not the ambient trace, and not an adiabat. However, the satellite overestimates the $T_{min}$ and must be corrected. A crude correction based on the CTS/GOES comparison in this case would be

$$T_{cloud} = T_{sat} - 15. \qquad (1)$$

From this estimate of $T_{cloud}$ an estimate of the updraft intensity can be made using the cloud model runs. The table in Fig. 3 gives the model results and the maximum height information from three aircraft overpasses. The line 3 height and temperature is roughly met by the model run with an updraft radius of 2 km. The associated maximum vertical velocity ($W_{max}$) is 35 m $s^{-1}$ at 275 mb. Therefore, although the storm is observed to penetrate only 1.5 km above the tropopause, it has, from this analysis, a very strong updraft, which agrees with the large radar reflectivities observed. The reason the cloud penetrates only the short distance above the tropopause is the effect of the relatively high static stability in the upper troposphere above 9 km which lessens the accelerating effect of the buoyancy term relative to water loading. The combined effect decelerates the model parcel significantly before hitting the tropopause. Therefore, in order to convert measures of storm maximum height to estimates of updraft intensity (a parameter better correlated with the occurrence of severe weather), the sounding structure must be taken into account beyond just a knowledge of tropopause temperature or height.

## 2.4 Satellite Observed Cloud Evolution

The solid line in Fig. 1 (GOES minimum $T_{BB}$) is the satellite observed minimum $T_{BB}$ over the area observed by the CTS. As the cloud passes its most intense stage, the coldest portion of the cloud shifts downwind over the central por-

tion of the anvil in the satellite image. This feature is indicated in Fig. 1 as the dotted line above the solid line from 2250-2310 GMT. From the side-looking photograph, the satellite cold point is related to smooth cirrus debris drifting downwind at an altitude at, or just above, the height of the now subsided convective area. The cirrus is at, or just above, the tropopause. The cirrus is not a candidate for producing a downwind warm spot sometimes observed in satellite images of intense thunderstorms because of its lack of height above the tropopause and the decrease with height of the ambient temperature above the tropopause (Fig. 3).

From the side photographs and the CTS overpasses, it is obvious that the convective area continually regenerates on the southwest end of the storm. However, following the coldest portion of the cloud from the satellite observations, one might incorrectly infer updraft movement into the middle of the anvil. A second updraft surge is obvious in the CTS data (lines 7 and 8) and side photographs and can be detected as a separate cold point in the satellite IR data (2250-2330 GMT).

## 3. GROWING STORM CHARACTERISTICS

A sequence of passes was also flown over a growing, but relatively weak, cumulonimbus cluster that reached a minimum CTS $T_{BB}$ of 235K (-38C), or a height of about 9 km. The trend of minimum $T_{BB}$ is shown in Fig. 4. Because of the rapidly changing features, continuity of individual towers is difficult in many cases (side photography was not available at this time) and Fig. 4 gives the minimum $T_{BB}$ anywhere in the cluster at each time. The concurrent satellite observations indicate observed $T_{BB}$'s much warmer (30-40K) than that observed with the CTS. This is due to field of view (beam filling) effects, along with the satellite "seeing" the side of the cloud.

The period of rapid cloud growth has a CTS-measured ascent rate of 2.2K $min^{-1}$. The minimum $T_{BB}$ (-38C) corresponds approximately with the cloud model run for 0.7 km radius (see Fig. 3). This model run has a vertical velocity peak of 15 m $s^{-1}$ at 500 mb (~-10C). Over the temperature layer spanned by lines 10 and 11 (-16C to -38C) the average model w is 10.1 m $s^{-1}$. Using the lapse rate following the parcel in the model run (8.3K $km^{-1}$), the CTS ascent rate of 2.2K $min^{-1}$ converts to a w of 4.4 m $s^{-1}$. Thus, the cloud top ascent rate appears to be only about half of the vertical velocity. This observation is in agreement with other studies for decelerating convective boundaries.

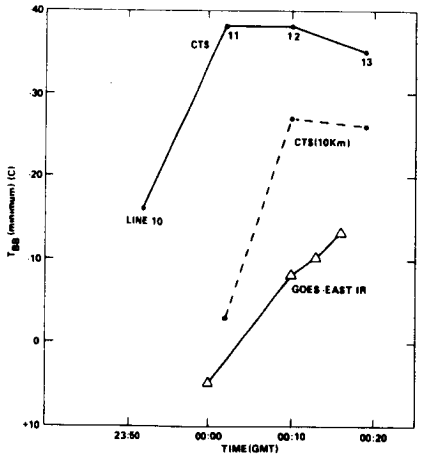


*Figure 4. Equivalent blackbody temperature ($T_{BB}$) as a function of time for growing storm as observed by aircraft and satellite radiometers.*

## 4. SUMMARY

Comparison of thunderstorm top observations made by aircraft overflights with a scanning radiometer and concurrent satellite observations indicate that:

1. Overshooting, cumuliform features on various scales appear as distinct cold areas in the high resolution (80 m) IR (11 micron) aircraft images.

2. Primarily because of field of view effects, the satellite IR observations overestimate $T_{BB}$ (minimum) by about 15K for storms significantly penetrating the tropopause. A satellite field of view of 1 km would alleviate this problem.

3. Profiles of height and $T_{BB}$ across overshooting features indicate an approximate adiabatic cloud surface lapse rate. However, one-dimensional cloud model runs point to using a lapse rate of ~7K $km^{-1}$ when comparing different storms reaching various $T_{min}$'s.

4. In order to convert measures of storm maximum height to estimates of updraft intensity (a parameter better correlated with the occurrence of severe weather) the sounding structure must be taken into account beyond just a knowledge of tropopause temperature or height.

5. During periods of updraft weakening, the lowest, satellite-observed $T_{BB}$ may occur downwind with cirrus debris.

6. For small, growing storms, the satellite will overestimate cloud top $T_{BB}$ by as much as 30-40K, again primarily because of field of view effects.

7. The cloud top ascent rate of a growing storm is approximately half the magnitude of the vertical velocity calculated from a one-dimensional cloud model.

## 5. FUTURE WORK

A detailed description of aircraft-observed features and storm evolution will be completed for this case study. Also, techniques are being developed to correct satellite-observed $T_{min}$'s for satellite field of view effects and other effects so that a better estimate of cloud top temperature (and height) can be made from the satellite data. The aircraft data, along with satellite stereo and high resolution IR data from low orbiting satellites will be used to verify and tune the techniques.

## 6. REFERENCES


Pitts, D. E., W. K. Reeser, and M. A. Mendlowitz, 1975: Equivalent blackbody temperature of the top of a severe storm. J. Appl. Met., 14, 609-618.

Roach, W. T., 1967: On the nature of the summit areas of severe storms in Oklahoma. Quart J. Roy. Meteor. Soc., 93, 318-336.

Simpson, J. and V. Wiggert, 1969: Model of precipitating cumulus towers. Mon. Wea. Rev., 97, 471-489.

Reprinted from JOURNAL OF APPLIED METEOROLOGY, Vol. 18, No. 4, April 1979
American Meteorological Society
Printed in U. S. A.

# Thunderstorm Intensity as Determined from Satellite Data[1]

ROBERT F. ADLER

*Laboratory for Atmospheric Sciences, NASA/Goddard Space Flight Center, Greenbelt, MD 20771*

DOUGLAS D. FENN

*GE/MATSCO, Beltsville, MD 20705*

(Manuscript received 28 June 1978, in final form 15 December 1978)

ABSTRACT

Digital infrared data from a geosynchronous satellite (SMS 2) on 6 May 1975 are used to study thunderstorm vertical growth rates and cloud top structure in relation to the occurrence of severe weather (tornadoes, hail and high wind) on the ground. All thunderstorms from South Dakota to Texas along a north–south oriented cold front are monitored for a 4 h period with 5 min interval data.

An examination of five cloud elements having eight tornadoes indicates that in seven of eight cases the first report of the tornado took place during, or just after, a period of cloud top ascent. This vertical velocity is applicable to an area of 15 km on a side.

Thunderstorm growth rate, as determined by the rate of blackbody temperature isotherm expansion and minimum cloud top temperature, are shown to be correlated with reports of severe weather on the ground. A time analysis indicates that the derived parameters reach critical values soon enough to provide a potential warning lead time of approximately 30 min.

Equations are derived relating the thunderstorm growth rate to vertical velocity and outflow layer divergence. Severe thunderstorm elements are shown to have mean vertical velocities approximately twice as large as the non-severe elements. The outflow layer divergence is calculated to be $1 \times 10^{-3}$ s$^{-1}$ for the severe thunderstorms.

## 1. Introduction

Information obtained from geosynchronous satellite data has the potential of leading to greater understanding of convective and other mesoscale activity and also the potential of being an important component in the detection and monitoring of thunderstorm activity in general, and of severe thunderstorms in particular. The detection of thunderstorms using satellite data has centered on the interpretation of images. For example, Purdom (1976) has noted that intersecting cloud lines can produce enhanced convection and thunderstorms. However, quantitative information on cloud growth rates can also be determined by examining a sequence of images. Sikdar *et al.* (1970), Purdom (1971) and Arn (1975) have used ATS 3 visible data to measure thunderstorm anvil expansion rates. Adler and Fenn (1976), Yuen (1977) and Negri *et al.* (1976) have used SMS data to make similar calculations. Adler and Fenn (1976) showed examples of cold area expansion rates related to thunderstorm growth using SMS window channel infrared data. These measurements were for areas smaller than entire cirrus anvils and provide a technique to monitor individual thunderstorms rather than a group of storms under a large cirrus shield. This last study also included an example of a tornado preceded by the rapid expansion of a cold area, implying rapid ascent. All of these studies indicated that there are parameters determinable from geosynchronous satellite data that tend to be related to the occurrence of severe weather.

## 2. Objective and approach of study

The objective of the research reported on in this paper is to develop techniques to use geosynchronous satellite data to help detect and monitor severe thunderstorms, and to study their characteristics. Specifically, the purpose is to determine if thunderstorm growth rates and characteristics observable with SMS infrared (IR) data can be correlated with the occurrence of severe weather on the ground. The occurrence of thunderstorm-related severe weather (tornadoes, hail, high winds) is highly correlated with the intensity of convection. Using SMS IR data one should be able to calculate parameters related to convection intensity, such as cloud top temperature and its rate of change.

A particular area is outlined and all thunderstorms,

[1] A preliminary version of this paper was presented at the Tenth Conference on Severe Local Storms at Omaha, Nebraska.

0021-8952/79/040502-16$08.00

or thunderstorm clusters, in that area for a given time period are monitored. Parameters derived from the satellite data are then compared to ground reports of severe weather. The discussion of the results in this paper concentrates on examples of tornado-bearing thunderstorms and comparisons between severe and non-severe thunderstorms. Vertical velocity and divergence estimates are also presented.

### 3. Data and method of calculation

SMS 2 digital IR data from the period 1803–2208 GMT 6 May 1975 were used in this study. This period was part of a limited-scan observation period wherein a relatively narrow swath, with its long axis oriented east–west, was observed by the satellite, but on a frequent basis. For this case the nominal period between observations was 5 min. The spatial resolution of the IR channel is about 9.4 km at 40°N. There is a sampling overlap in the left-to-right direction so that each data point is centered 4.7 km from the center of the next. Lines are repeated during the data processing to complement the left-to-right oversampling so that image distances, either left-to-right or up-to-down, correspond approximately to each other in terms of geographical distance. Because of the sampling overlap in the left-to-right direction and the repetition of lines, each data point in this study represents an area approximately 4.7 km on a side, or 22 km$^2$.

The calculations presented in the next section were performed on the Atmospheric and Oceanic Information Processing System (AOIPS), an interactive image processing system described by Billingsley (1976). With this system, an irregularly shaped area can be outlined on a color enhanced television image and a histogram of the digital counts inside the area obtained.

The temperature resolution of the IR data is 1 K in the range of equivalent blackbody temperatures ($T_{BB}$'s) of interest in this study. Due to the fixed point algorithm used in the transformation of raw counts into calibrated values, voids appear in histograms (Goddard and Remondi, 1975). In the range of $T_{BB}$ between 206–226 K, these voids appear every 3–5 K.

From the calculated histogram a cumulative histogram is compiled starting from the cold end of the temperature distribution. The number of points $N_i$ with $T_{BB} \leqslant T_i$ is obtained, with $T_i$ ranging from the lowest temperature in the area to the highest temperature $T_0$, where $T_0$ is defined as the warmest $T_{BB}$ that forms a closed isotherm around the element being defined. In the case of easily definable, individual thunderstorms or thunderstorm clusters, an entire cirrus anvil may be defined. Examination of cirrus anvils led to the subjective determination that the $T_{BB}=258$ K isotherm corresponds approximately to the anvil edge. Although this value is much warmer than the actual cloud temperature, the emissivity at the thin anvil edge is much less than unity, resulting in the warm $T_{BB}$. In addition, the response function of the sensor may result in a more gradual change in $T_{BB}$ than is actually occurring. Preliminary examination of expanding anvils indicated that the areal change within somewhat lower $T_{BB}$'s paralleled the areal change within 258 K. For this reason a lower temperature, $T_{BB}=226$ K, was chosen as the warmest cloud tops to be considered in the definition of areas. Therefore, the clouds studied here have already obtained a height of at least 9.5 km based on soundings for this day. The early development of the thunderstorms is thus not examined in this study. Satellite observations of earlier growth of thunderstorms is examined by Adler and Fenn (1978).

As the anvil of a thunderstorm or thunderstorm cluster expands, it eventually comes into contact with other anvils. When the warmer temperatures near the outer edge of the cloud can no longer be uniquely identified with the feature being examined, $T_0$ is decreased to a value such that the statistics of the data inside the area defined by $T_0$ now represent the feature being examined. In areas where a number of anvils have formed a continuous cirrus overcast, the object is to detect and monitor colder (higher) regions within the general cirrus background. In these cases $T_0$ is often very cold ($\sim$212 K) and the elements defined contain only a small range of $T_{BB}$.

The thunderstorms analyzed in this study lie along a generally north–south oriented cold front from Nebraska southward through Texas. This area contains all the reported tornadoes for this day during this time, other severe thunderstorms, and thunderstorms with no reported severe weather. A selection of SMS 2 images covering the time period studied is shown in Fig. 1. Especially late in the period there are areas of cirrostratus clouds which cannot be associated with individual thunderstorm anvils. Thunderstorm elements can still be identified by analyzing only the colder portions of a cloud. For example, Fig. 2 shows the distribution of selected $T_{BB}$ isotherms for the region outlined in the 2128 GMT panel of Fig. 1. The area of interest in Fig. 2 is the region of relatively cold temperatures below the center of each panel. At 2057 GMT there is only a small area having a temperature of 208 K. Over the next 30 min the 208 K isotherm expands rapidly and colder temperatures appear. These changes imply ascent. The element defined by the 208 and 206 K isotherms is typical of the small, cold cloud elements monitored in this case. This particular element (defined as cloud 8b) was associated with the Omaha tornado which touched down at 2133 GMT. The position of the Omaha tornado relative to the cloud top $T_{BB}$'s is shown in the last panel of the figure. A hail report is shown in the panel for 2118 GMT. A discussion of tornado reports relative

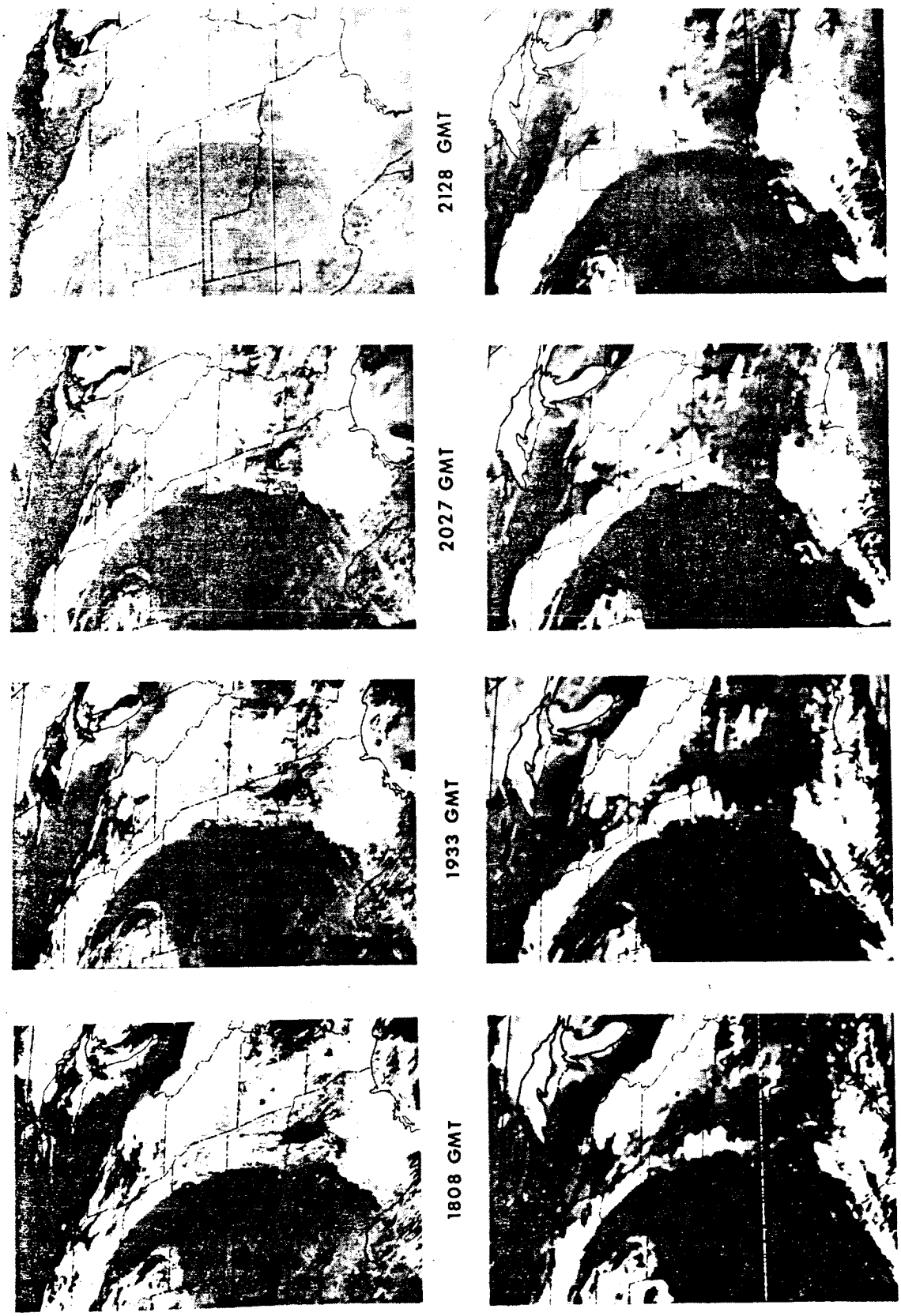


FIG. 1. Sequence of SMS 2 images over study area and period.

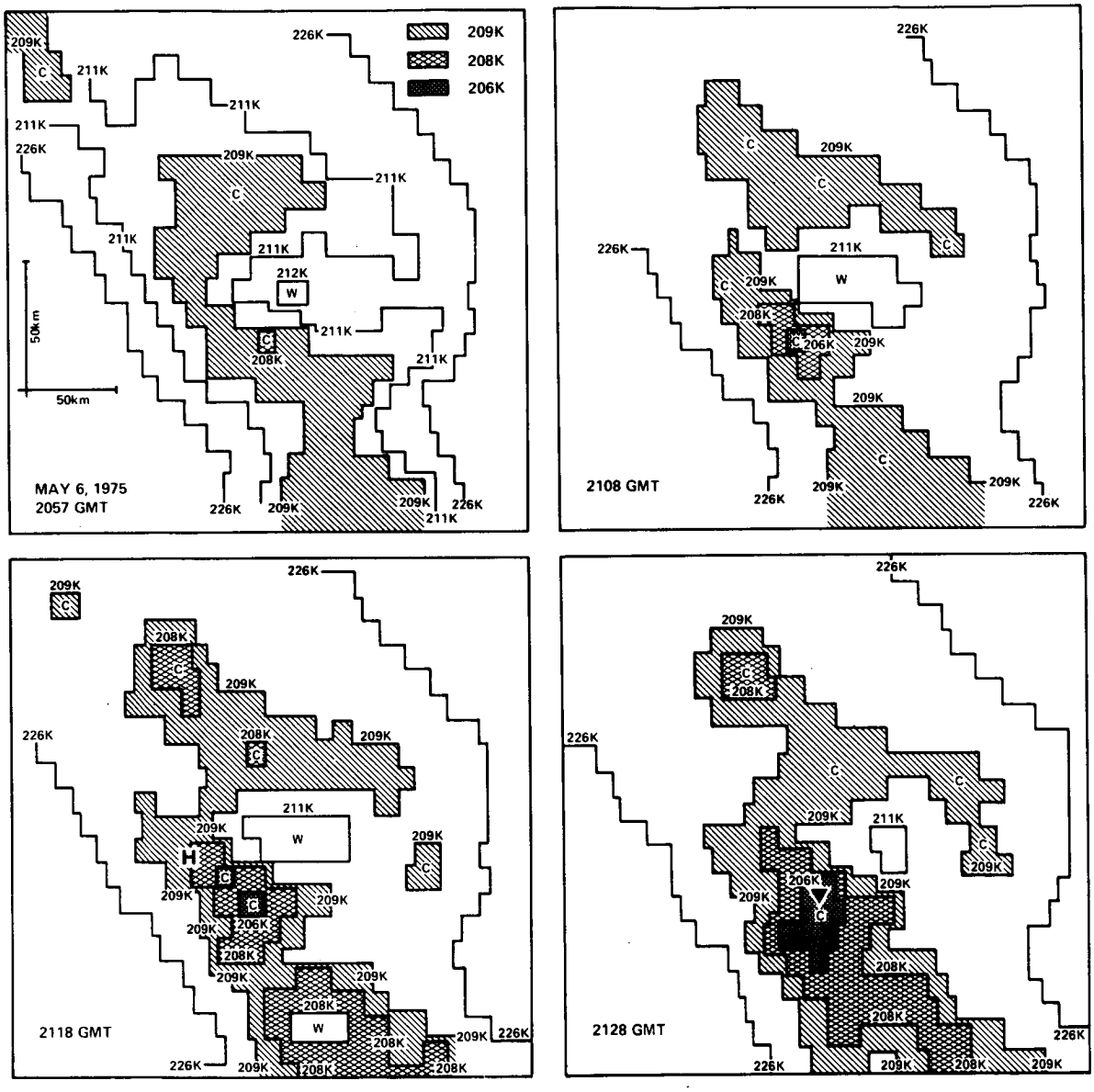


FIG. 2. Analyses of infrared $T_{BB}$ isotherms over a small area shown in Fig. 1. H marks location of hail reports; triangle marks tornado report.

to cloud top features is given in the next section. From Fig. 2 it can be seen that the expansion of the small cold areas cannot be interpreted as anvil expansion. Analysis of the cold area expansions in terms of vertical velocity and divergence is given in Section 7.

The occurrence of severe weather in this study is determined primarily from the Severe Weather Events Log compiled by the National Severe Storm Forecast Center (NSSFC) in Kansas City, with cross reference to the Environmental Data Service's *Storm Data*.

## 4. Results from tornado-bearing storms

Five clouds or elements in the area examined had tornadoes associated with them, with the total number of tornadoes being nine. The approximate locations of the tornadoes are given in Fig. 3. Four of these tornadoes can be considered relatively strong tornadoes. These are identified by nearby town names as the Pierce, Magnet, Winside and Omaha tornadoes, all occurring in Nebraska. The fifth tornado cloud is

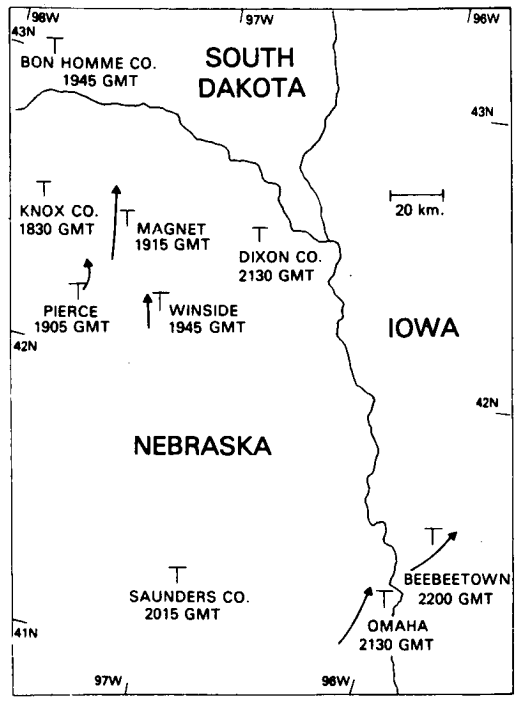


FIG. 3. Location of tornadoes on 6 May 1975 in area of interest. Arrows represent approximate tracks for relatively strong tornadoes.

associated with the relatively weak Saunders County (Nebraska) tornado.

Fig. 4 is the thunderstorm growth rate diagram for cloud 4. The cloud numbering system is the original one used in the study to identify approximately 60 clouds or elements from South Dakota to Texas. Eventually, only 39 elements were determined to be active thunderstorm areas. The eliminated elements could only be followed for a short time and indicated little or no growth. The cloud or element numbers will, therefore, not necessarily be sequential. The diagram indicates the relation between $N_i$ and time, where $N_i$ is the number of data points in the defined element with blackbody temperature $T_{BB} \leqslant T_i$. For example, the curve in Fig. 4 for $T_i = 218$ K exhibits an increase from $N = 14$ at 1808 GMT to $N = 60$ at 1823 GMT. Before 1808 the minimum $T_{BB}$ was warmer than 218 K. The curve is drawn to $N = 1$ at 1803 GMT, so that the growth from zero to 14 can be displayed. Because the $N$ axis is logarithmic, the slopes of the lines are proportional to $N^{-1}dN/dt$. Plotted points which are circled indicate that the area is not defined uniquely by that isotherm, but that a portion of the border is approximated. The approximation is usually small and does not significantly affect the count. The conversion from number to area is accomplished by multiplying the number of points by 22 km$^2$. The location in time of the severe weather events is shown across the top of the diagram.

Cloud 4 in Fig. 4 shows a rapid decrease in minimum blackbody temperature, or $T_{\min}$, and a rapid expansion of areas within isotherms. The decrease in temperature can be calculated by moving horizontally across the diagram at, for example, $N = 10$. The 216 and 212 K lines are separated by 20 min, indicating a rate of decrease of 0.2 K min$^{-1}$. The values of $N^{-1}dN/dt$ are of order of magnitude $10^{-3}$ s$^{-1}$. The decrease in temperature and expansion of isotherms, of course, implies ascent. The vertical velocity is related to the rate of temperature change by

$$w = \left(\frac{\partial T}{\partial z}\right)^{-1} \frac{dT}{dt}. \tag{1}$$

With a reasonable lapse rate, 8 K km$^{-1}$, the temperature change of 0.2 K min$^{-1}$ is equivalent to a vertical velocity of $w$ of 0.4 m s$^{-1}$. This is a reasonable vertical velocity estimate considering the area over which it is an average ($\sim$225 km$^2$) and considering it represents a time when the cloud top is decelerating as it approaches and penetrates the tropopause at approximately 12 km. Much larger values of vertical velocity are calculated for clouds whose tops are just 1 or 2 km lower. A more detailed examination of the vertical velocity estimates is given in Section 7.

Three tornadoes are associated with cloud 4 (Fig. 4). One in Bon Homme County (South Dakota) is in the

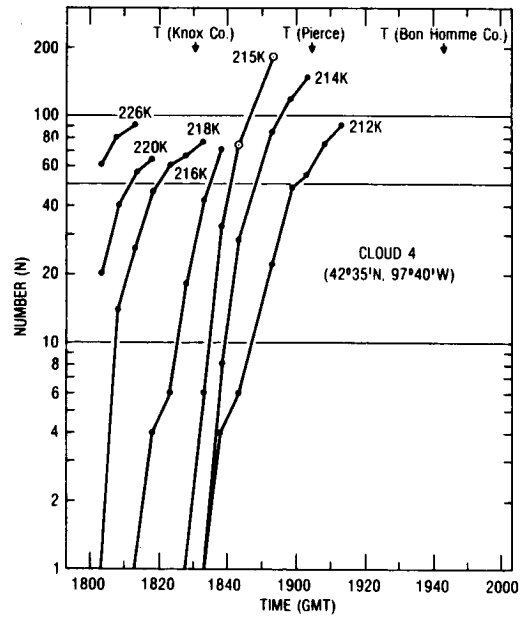


FIG. 4. Thunderstorm growth rate diagram for cloud 4. $N$ is the number of data points in the element with blackbody temperature $T_{BB} \leqslant T_i$, where $T_i$ is as identified in the diagram. Occurrence of severe weather is marked by arrow at time of report, with T indicating tornado.

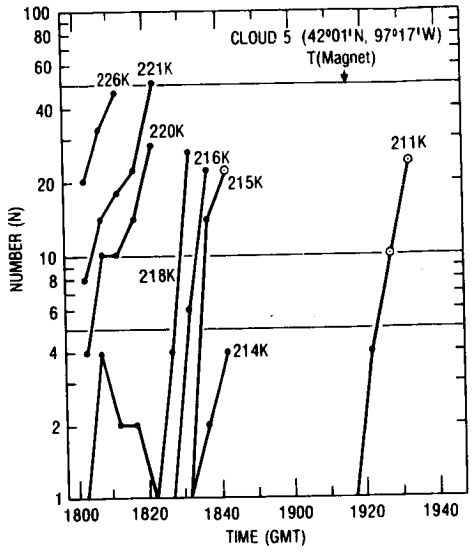


FIG. 5. Thunderstorm growth rate diagram for cloud 5.

vicinity of this element, but when no distinct cold area can be defined. The Pierce tornado, the strongest of the three, was first reported at 1905 GMT. At that time and immediately preceding it, during the tornado formation period, the element exhibits cold area expansion and decreasing temperature, indicating ascent. The same pattern also is associated with the Knox County tornado.

Fig. 5 shows the diagram for cloud 5 which is identified as having been associated with the Magnet tornado. At the beginning of the period, relatively slow growth is indicated for the 221 and 220 K areas. A few points with $T=218$ K appear and then disappear before a period of very rapid growth is observed between 1825–1840 GMT. The maximum of $N^{-1}dN/dt$ is $6.2\times10^{-3}$ s$^{-1}$ at 218 K. The minimum temperature also drops very rapidly during this period. After 1843 GMT no clearly defined cold area can be identified, although the cloud element can still be identified in the higher resolution visible images. In the IR data cloud 5 appears as an extension of an element immediately to the south, cloud 22. Not until 1923 GMT or 40 min later, is a definable cold area at 211 K observed for cloud 5. Over the next 10 min this isotherm expands swiftly. The initial report of the tornado is at 1915 GMT, as noted on the diagram, but the tornado hits the town of Magnet at 1945 GMT and lasts at least until 2000 GMT. It, therefore, appears that this tornado also formed and touched down during a time when the thunderstorm top was ascending at the spatial scale observable with the IR data.

Just to the south of the Magnet cloud is cloud 22 (Fig. 6). This element can be defined continuously for almost 3 h. Two tornadoes are associated with this element at two widely separated times. The first, at Winside, Nebraska, is reported at 1945 GMT. As with the tornadoes already examined, this tornado occurs during a period of rapid increase in cold area, which in this case lasts from about 1900 GMT until 2000 GMT. The maximum value of $N^{-1}dN/dt$ is $4.5\times10^{-3}$ s$^{-1}$, following the 211 K isotherm. The second, weaker

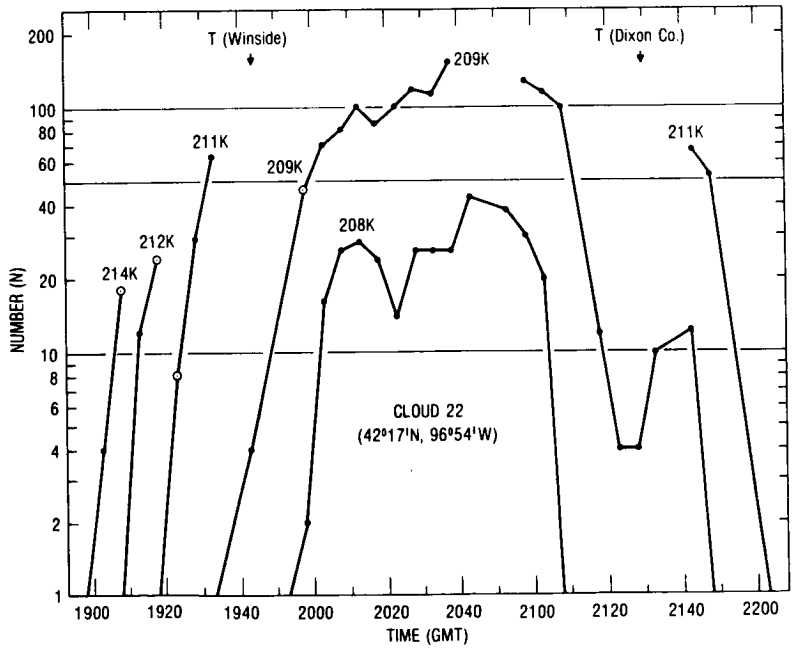


FIG. 6. Thunderstorm growth rate diagram for cloud 22.

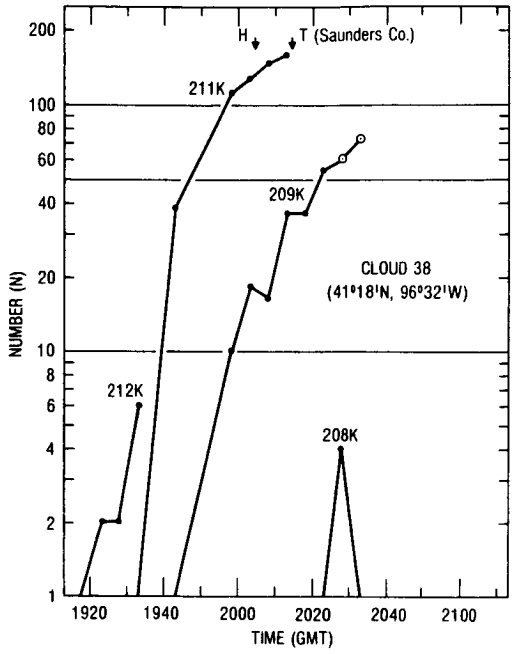


FIG. 7. Thunderstorm growth rate diagram for cloud 38. H indicates report of hail.

tornado, at 2130 GMT, is located in Dixon County, Nebraska. Although there is a brief period of expanding cold area between 2125–2145 GMT, this tornado occurs during a period of generally decreasing cold areas and warming temperatures. One can speculate that during the dying phase of element 22, one last vigorous thunderstorm penetrates the cirrus shield, showing up for a short time as the secondary maximum in the 209 K curve at 2140 GMT.

A tornado occurring in Saunders Country, Nebraska, is associated with cloud 38 (Fig. 7). Again, the reported time of the tornado is during a period of cold area expansion indicating ascent. The most rapid increase in $N$ is between 1930–1950 GMT at a rate of 6.7 $\times 10^{-3}$ s$^{-1}$. The minimum temperature reached is 208 K.

The curves for cloud 8b are shown in Fig. 8. Two tornadoes are associated with this cloud, including the severe Omaha tornado. This element is observed to go through two periods of rapid ascent during a 2 h period. Reports of hail and high wind (>50 kt) are associated with the first period of rapid expansion. The element is then observed to have a decrease in cold area between 2040–2055 GMT. After that there is a sharp increase in $N$(208 K) and colder temperatures appear. Although there is good continuity of the element during this cycle of inferred ascent and descent, the second period of ascent is probably brought about by a new thunderstorm penetrating the cirrus shield in approximately the same area.

Similar to previous cases, the growth rate of cloud 8b during the 30 min period prior to the first tornado report indicates ascent. During the lifetime of the tornado (2133–2150 GMT) no very sharp area increase is noted. In fact, the dip in the 206 K line could possibly be interpreted as a partial collapse of the thunderstorm top. This is the only element for which such a feature is evident. No data are available from 2150 to 2208 GMT. At the later time, 205 K temperatures appear, indicating more growth. The Beebeetown, Iowa, tornado is reported during the period 2200 to 2230 GMT.

During the time period examined, nine tornadoes were reported, eight of which could be clearly connected with a small, cold area in the IR data. The exception was the Bon Homme County tornado which was located in the vicinity of cloud 4, but long after it was no longer possible to define a small, distinct cold area in it. Of the remaining eight cases, all but one (Dixon County—cloud 22) occurred during, or just after, a rapid increase in cold area, indicating cloud top ascent. Therefore, it appears that the formation of tornadoes in a large majority of cases occurred during a period of increasing thunderstorm cloud top height. This upward vertical velocity applies on a spatial scale of approximately 15 km on a side.

The observations of increasing thunderstorm top heights at the time of, or just prior to, tornado touchdown in the present study seemingly contradict aircraft observations of overshooting tops discussed by Fujita (1973), Pearl (1974) and Umenhofer (1975). They relate collapsing cloud domes (above the anvil cirrus) to the occurrence of tornadoes. This discrep-

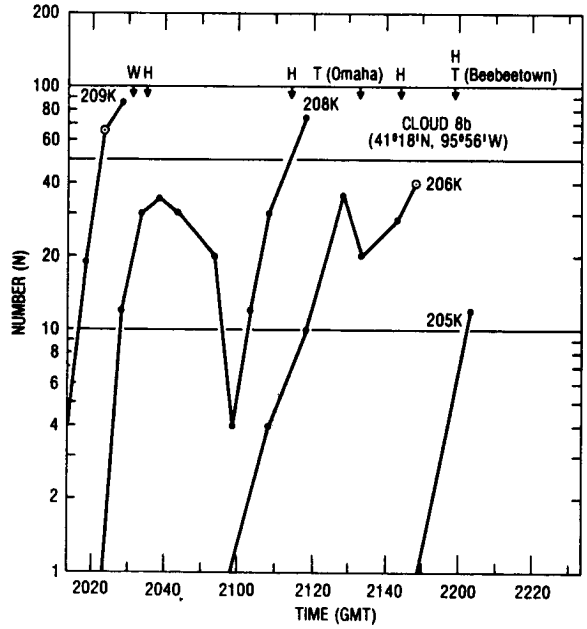


FIG. 8. Thunderstorm growth rate diagram for cloud 8b. W indicates high winds.

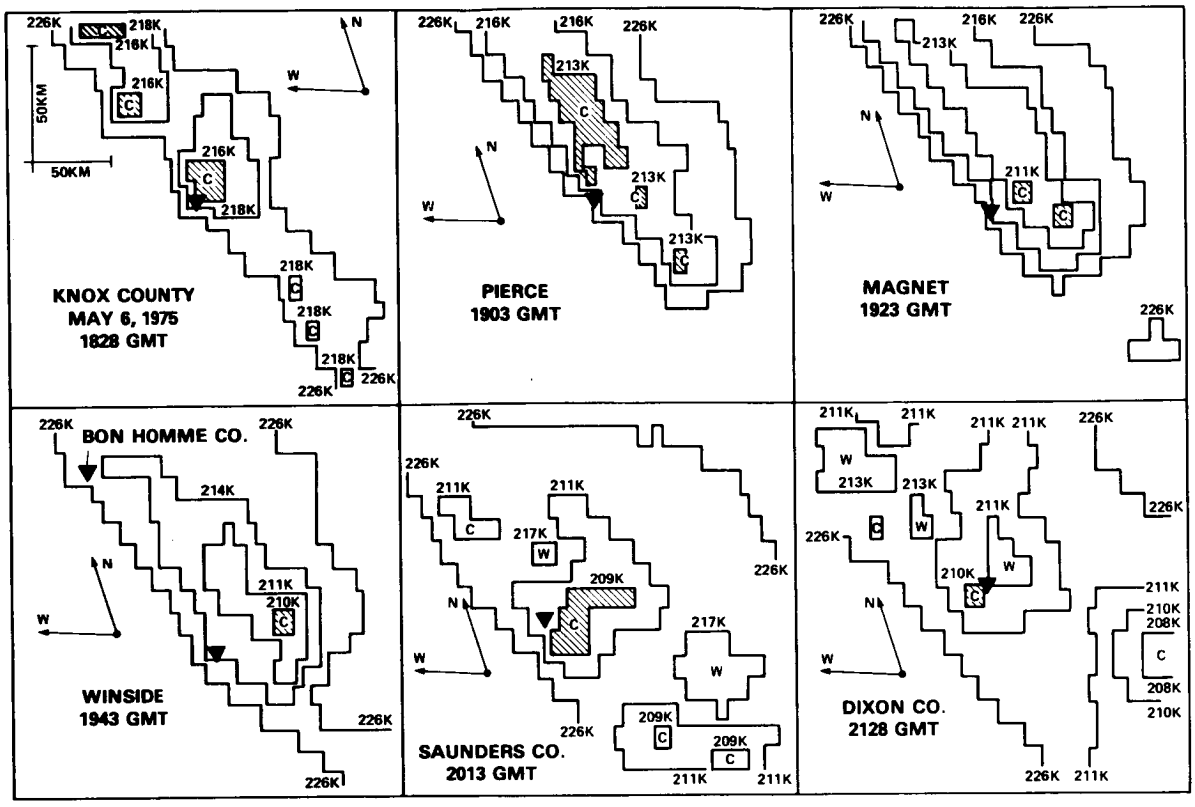


FIG. 9. Location of tornado reports relative to IR cloud top features.

ancy may be related to a difference in scale between the two types of observations. The satellite observations apply to a scale of about 15 km on a side. Shenk (1974) has examined the size distribution of overshooting domes or turrets and finds a median diameter of approximately 5 km. Therefore, the satellite vertical motions are applicable to an area approximately an order of magnitude larger than that observed with the aircraft. Comparison of results is therefore difficult.

Radar observations also do not show a sharp increase in echo top height prior to tornado touchdown. For example, Lemon *et al.* (1978) show nearly steady or slightly decreasing radar heights for the 30 min prior to the Union City, Oklahoma, tornado. A rapid decrease of the radar top follows the tornado touchdown. Again these observations are on a small scale compared to the satellite-based cloud top changes. A full understanding of the relation of satellite-inferred cloud top changes, radar echo height and actual cloud changes on various scales must await closer coordination in the observations.

Locations of six tornado reports relative to cloud top features observed in the satellite IR data are shown in Fig. 9. A similar diagram for the Omaha tornado is given in Fig. 2. The surface tornado locations have been shifted to cloud top relative positions for a cloud height of 12 km to compensate for the satellite viewing angle. The tornado reports tend to be located to the west or southwest of the coldest temperatures, in an area of large gradient of $T_{BB}$. Early in the 4 h period (before 2000 GMT) the tornado reports are located near the 226 K $T_{BB}$ isotherm, which is near, but inside, the upwind cirrus anvil edge. Later, after the cloud has expanded and the anvil edge is farther from the cold center, the tornado reports are located more distant from the cloud edge.

## 5. Example comparison of a severe and non-severe case

Two adjacent thunderstorm elements which developed in southeast Nebraska at about the same time provide an excellent comparison of clouds with and without accompanying severe weather. The diagrams for these elements (clouds 8 and 9) are shown in Figs. 10 and 11, respectively.

Both elements reach a temperature of 226 K a little after 1800 GMT and continue to grow to higher heights and colder temperatures during the next two hours. However, there are significant differences in the rate of growth and the final temperature reached. Cloud 9, with no accompanying severe weather reports, has lower values of normalized growth rate $N^{-1}dN/dt$ and an associated less rapid decrease of minimum

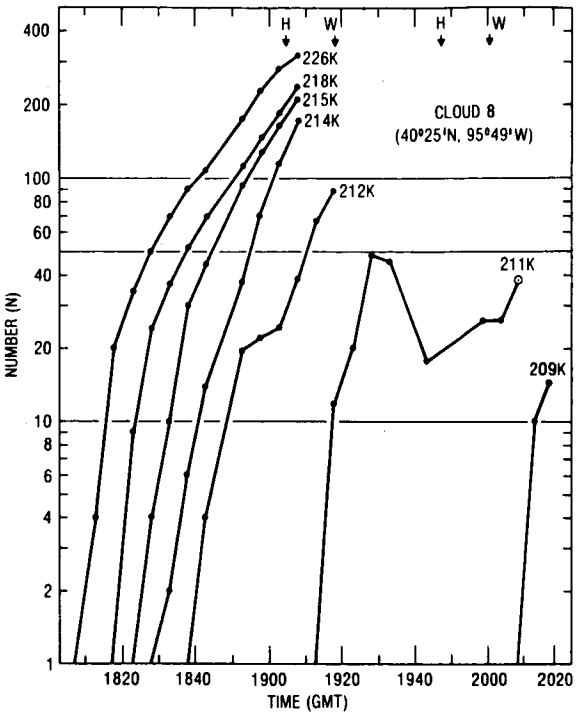


FIG. 10. Thunderstorm growth rate diagram for cloud 8.

temperature. Its eventual coldest temperature is 212 K compared to 209 K for cloud 8. Two reports of hail and two reports of high wind are associated with cloud 8. The first pair of hail and wind reports occur near the end of the period of rapid growth; the second pair happen during a relatively stable period. This second pair may be due to a thunderstorm growing rapidly from below, but hidden by the already high and dense cirrus anvil of the previous cell. Finally, at the end of the period the new thunderstorm penetrates the anvil and becomes observable as the 209 K area at 2015 GMT.

The comparison of cloud elements 8 and 9 is the best available of those analyzed. These two clouds began about the same time, lasted a substantial amount of time and were easily defined. Other elements were sometimes obscured by anvils of more rapidly growing storms and other weak elements often became undefined in a general cirrostratus shield. In general, however, the strong thunderstorms are easily observable.

## 6. Results for all storms

Results from the analysis of 39 thunderstorms or thunderstorm clusters are discussed in this section. There are 15 elements associated with severe weather and 24 with no reported severe weather. In the area analyzed these 39 elements are all the clouds defined as growing thunderstorms. A few other elements were defined but lasted only a short time, showed minimal change, and no severe weather reports were associated with them.

An examination of the thunderstorm growth diagrams and the patterns of digital data gave the impression that two simple characteristics were correlated with the occurrence of severe weather. These characteristics are minimum cloud top temperature and thunderstorm growth rate as given by the normalized rate of cold area expansion.

Fig. 12 displays the results of plotting the minimum temperature during an element's lifetime ($T_{min}$) against the thunderstorm growth rate. The dots represent non-severe cases, while T's and H's represent tornadoes and hail respectively. The following procedure was used to arrive at a single value of $N^{-1}dN/dt$ to represent each element. The maximum $N^{-1}dN/dt$ value, for any temperature $\leqslant 226$ K, is determined by examining the time change between $N=6$ and $N=30$ for each temperature. These two values were chosen so that the rate of increase is for relatively small areas, but that there are enough data points (6) to establish the lower threshold without being affected severely by instrument noise. A few elements had no curves of $N$ lasting from $N=6$ to 30, so the parameter was calculated using the largest range available.

An examination of Fig. 12 indicates that the severe weather elements tend to have cold minimum cloud top temperatures and large rates of growth. A series of discriminant analyses (Panofsky and Brier, 1963) were performed, using the data displayed in Fig. 12. Table 1 shows the results. For $T_{min}$ by itself a severe,

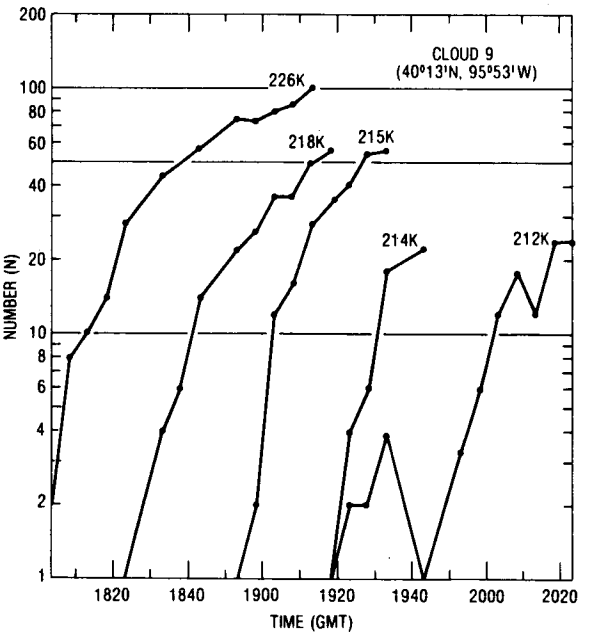


FIG. 11. Thunderstorm growth rate diagram for cloud 9.

non-severe dividing line of 212.8 K was derived. For temperatures above 213 K only one out of 12 elements had severe weather, while 14 out of 27 with temperatures colder than 213 K had associated severe weather reports. For maximum rate of growth the derived dividing line is $3.5\times10^{-3}$ s$^{-1}$ with severe and non-severe events distributed around that value as shown in the table. A combined discriminant analysis using $T_{min}$ and $N^{-1}dN/dt$ produced the results shown in the last row in the table and by the diagonal line in Fig. 12. Based on the two variable discriminant analysis a probability of detection (POD) equal to 0.73 was calculated along with a value of 0.31 for the false alarm rate (FAR) and 0.55 for the critical success index (CSI). The definition of these variables follows Donaldson *et al.* (1975). There are five elements with associated tornadoes, and their relations to the derived critical values are given by the fractions in parentheses in Table 1.

Statistical tests were also performed to determine if there was a significant difference between the means for severe thunderstorms and non-severe thunderstorms. For $T_{min}$ the mean values were 209.5 and 212.3 K for severe and non-severe cases. Using a $t$-distribution test, the difference of means was shown to be significant at the 5% level, with the value of $t$ just missing the value for the 1% level. For $N^{-1}dN/dt$ the means were $4.5\times10^{-3}$ and $3.1\times10^{-3}$ s$^{-1}$. This difference of means also is significant at the 5% level, again barely missing the 1% value.

It is not surprising that $T_{min}$ and thunderstorm growth rate ($N^{-1}dN/dt$) are correlated with occurrences of severe weather. Both parameters are obvious indicators of the intensity of convection. Colder temperatures imply higher thunderstorm heights, which have long been related to thunderstorm severity through radar observations. All 39 elements involved in this analysis were associated with vigorous thunderstorms. The very weakest, as indicated in the bottom, left-hand corner of Fig. 12, had a minimum temperature of 219 K, which is equivalent to a height of 11.1 km, using the nearby 0000 GMT 7 May Omaha sounding. The coldest cloud had a temperature of 205 K, or a height of 13.0 km. The 0000 GMT 7 May

TABLE 1. Discriminant analysis summary for cloud top minimum temperature, maximum rate of growth, and the two variables combined. The parameter $L$ is positive for predicted severe weather.

| Variable(s) | Value for $L=0$ | Fraction of elements with severe weather* $L<0$ | $L>0$ |
|---|---|---|---|
| Cloud top minimum temperature ($T_{min}$) | 212.8 K | $\frac{1}{12}\left(\frac{0}{12}\right)$ | $\frac{14}{27}\left(\frac{5}{27}\right)$ |
| Maximum rate of growth $\left(\frac{1}{N}\frac{dN}{dt}\right)$ | $3.5\times10^{-3}$ s$^{-1}$ | $\frac{5}{22}\left(\frac{1}{22}\right)$ | $\frac{10}{17}\left(\frac{4}{17}\right)$ |
| Combined $T_{min}$ and $\frac{1}{N}\frac{dN}{dt}$ | $L=9.75+91\left(\frac{1}{N}\frac{dN}{dt}\right)-0.048\ T_{min}$ | $\frac{4}{23}\left(\frac{0}{23}\right)$ | $\frac{11}{16}\left(\frac{5}{16}\right)$ |

* Values in parentheses indicate tornado cases.

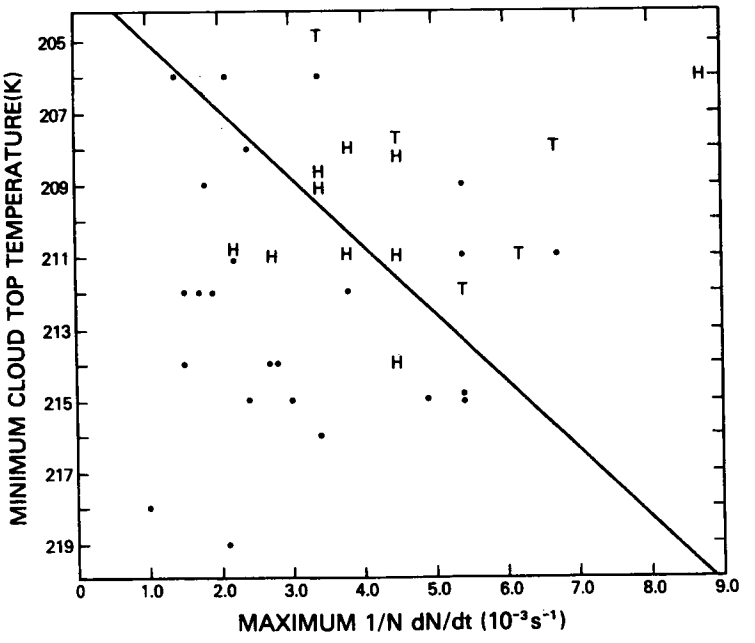


FIG. 12. Relation of thunderstorm rate of growth (cold area expansion) to cloud top minimum temperature and the occurrence of severe weather for all 39 thunderstorm elements in analysis area. T indicates tornado, H represents reported hail.

TABLE 2. Median warning lead time for all elements with severe weather.

| Criterion | Number of cases | Median value of lead time (min) |
|---|---|---|
| $T_{min}$ | 14 | 24 |
| $\frac{1}{N}\frac{dN}{dt}$ | 10 | 27.5 |
| Combined | 11 | 7 |

sounding has a minimum temperature of 206 K. The tropopause is probably located at 222 mb at a temperature of 215 K, although there is another sharp increase in static stability above that, at a pressure of 168 mb and at a minimum temperature of 206 K. Twelve hours earlier the Omaha sounding has the tropopause located at 200 mb and 213 K. Farther south along the area studied the tropopause temperature was also in the vicinity of 213 K. At Monett, Missouri, the tropopause temperature values were 211 and 215 K at 1800 GMT 6 May and 0000 GMT 7 May. Thus an approximate tropopause temperature for this region on this day was 213 K, which is the threshold temperature in the discriminant analysis discussed earlier. This result may be accidental, but is supported by similar observations by Pryor (1978). Additional studies are needed to ascertain the relations among the temperature structure and tropopause height, the satellite-observed cloud-top temperatures and storm severity.

The thunderstorm heights estimated from the satellite data in this study are substantially lower than the corresponding radar estimates. A cursory comparison of the satellite-based heights with the radar-estimated storm tops as analyzed on the National Weather Service's radar summary chart, indicates a mean 2 km underestimate from the satellite information.

The reason for the radar-satellite differences is probably related to the scale of the observations and the limitations of the satellite data. The satellite-observed cloud top temperatures are for a larger horizontal area. The instantaneous field of view (IFOV) of the satellite IR sensor at this latitude is approximately 9 km on a side. The radar observations are probably representative of a smaller region.

The satellite data are also limited by the temperature structure. For elements of the size with which we are dealing, the cloud top probably takes on a temperature which is a combination of updraft temperature (from the moist adiabat) and the ambient air at that altitude. This will have the effect of somewhat limiting the greatest indicated height. Clouds penetrating into the lower stratosphere will have their height underestimated.

In addition, Negri *et al.* (1976) have already noted that SMS IR temperatures underestimate thunderstorm height, especially for small elements. They attribute this effect to inadequate sensor response when going from a warm to a cold target. This is also a probable contributor to the radar-satellite difference noted in this study. Because of these factors the satellite-based estimates of thunderstorm height should be treated cautiously, although relative heights are probably valid.

The thunderstorm growth rate parameter $N^{-1}dN/dt$ is an indicator of the magnitude of the upward vertical velocity and the upper level divergence. The relation of these three variables is explored in the next section. One interesting point from Fig. 12 is that $T_{min}$ and $N^{-1}dN/dt$ appear to be almost uncorrelated. One would expect that faster growing storms would penetrate to higher heights and colder temperatures, and therefore that the two parameters would be correlated. It is believed that this lack of correlation arises because the thunderstorm elements in many cases were hidden by thick cirrus produced by other convection and, consequently, could not be monitored early in their history when the growth rates were most likely the most rapid. By the time the element penetrates the cirrus shield and growth rates can be calculated, the rate of growth has slowed. Such elements reaching cold temperatures, however, are represented by points on Fig. 12 with low temperatures and low growth rates. Another problem is the comparison of $N^{-1}dN/dt$ values irrespective of at what temperature or height they are calculated. Thus values of $N^{-1}dN/dt$ of $5\times10^{-3}$ s$^{-1}$ calculated at $T_{BB}=220$ K may not reflect as large a relative velocity as $5\times10^{-3}$ s$^{-1}$ at 210 K. With the addition of more cases these types of refined analysis will be possible.

The parameters calculated appear to have the potential to be positive contributors to a severe storm warning system. To test what type of warning lead times might be achieved, the following calculations were made. Based on the criteria in Table 1, the time difference between when the element met the criterion and the time of the first report of severe weather was calculated for each element that met the criterion. The median values are displayed in Table 2. The median lead times are ~25 min for the one-variable criteria, but only 7 min for the combined criterion.

TABLE 3. Median warning lead time for elements with tornadoes.

| Criterion | Number of cases | Median value of lead time (min) |
|---|---|---|
| $T_{min}$ | 5 | 33 |
| $\frac{1}{N}\frac{dN}{dt}$ | 4 | 35 |
| Combined | 5 | 29 |

A second calculation was made using the first report of tornadoes only and the results are shown in Table 3. The median lead time is ~30 min. The results of Tables 2 and 3 point out that the parameters calculable from the SMS data are not only correlated with reports of severe weather, but usually meet the severe thunderstorm criteria before the actual severe weather (hail, tornadoes) occurs.

## 7. Vertical velocity and divergence estimates

### *a. Interpretation of $N^{-1}dN/dt$*

The parameter chosen in this study to indicate thunderstorm rate of growth is the areal expansion of blackbody temperature isotherms in the window channel infrared data. This parameter has been chosen in place of rate of temperature change because many instances arise where this rate is difficult to calculate due to poor temperature resolution. Figs. 7 and 8 are examples of this situation. The calculated values of $N^{-1}dN/dt$ also appeared to be relatively independent of the temperature or height.

If a blackbody temperature isotherm is chosen so that it nearly coincides with the edge of the thunderstorm anvil, normalized expansion of the area within the isotherm is a direct measure of outflow divergence. That is,

$$D\ (\text{divergence}) = \frac{1}{A}\frac{dA}{dt}, \tag{2}$$

disregarding any dissipation of the anvil edge. In the present study, however, the isotherm expansions ($N^{-1}dN/dt$) calculated were usually chosen for areas well within the anvil edge. There are two reasons for this choice. First, the emphasis here is on obtaining parameters which are applicable on a spatial scale as close as possible to thunderstorm scale. This is why the $N^{-1}dN/dt$ values in Fig. 12 are calculated between $N=6$ and $N=30$. The anvil would cover an area two orders of magnitude larger. Second, it is often difficult to define an anvil edge because of complex interactions between thunderstorms.

The calculations of $N^{-1}dN/dt$ from $N=6$ to $N=30$ are applicable to an area of about 15 km on a side and definitely do *not* represent anvil expansion. The results of this section will show that vertical velocity estimates can be made from the isotherm expansion values.

The interpretation of $N^{-1}dN/dt$ in terms of vertical velocity and divergence is shown schematically in Fig. 13. The cross-sectional or side view in upper part of the diagram shows the curved surface of the cloud top at two times, $t_1$ and $t_2$. The vertical coordinate is temperature. The emissivity of the cloud top is assumed to be unity. This should be a good assumption in the inner part of the thunderstorm top where this analysis applies. From times $t_1$ to $t_2$ the

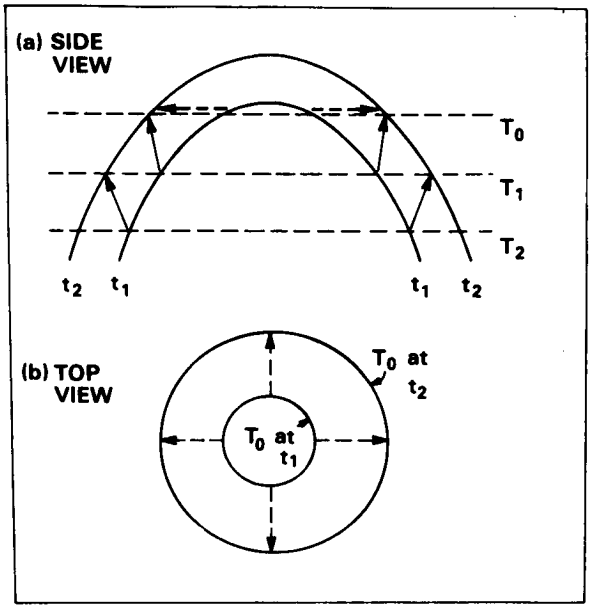


FIG. 13. Schematic views of idealized cloud top at two different times. Temperatures are indicated by $T_0$, $T_1$ and $T_2$. Solid arrows represent actual air motion, while dashed vectors represent the expansion of blackbody temperature isotherms, as viewed by the satellite.

area inside the $T_0$ isotherm expands. This is seen by the horizontal dashed arrows in the upper part of the figure and is also indicated in the top view in the lower part of the diagram. This areal expansion is equivalent to the $N^{-1}dN/dt$ which is measured with the satellite data.

The actual flow of air, however, is given by the solid arrows. The air ascends and therefore cools (moist adiabatically) and is somewhat divergent. If this simple schematic diagram is basically correct then the expansion of cold areas as denoted by $N^{-1}dN/dt$ is really a combination of vertical velocity and divergence effects.

### *b. Derivation of equations*

The relationships of $N^{-1}dN/dt$, divergence and vertical motion can be shown through the following derivation. A point on the cloud surface is represented by the position vector

$$\mathbf{r} = x\mathbf{i} + y\mathbf{j} + z\mathbf{k}, \tag{3}$$

and the motion of the point is given by

$$\frac{d\mathbf{r}}{dt} = \mathbf{V} = \frac{dx}{dt}\mathbf{i} + \frac{dy}{dt}\mathbf{j} + \frac{dz}{dt}\mathbf{k}. \tag{4}$$

The horizontal motion in the $x$ direction (Fig. 13a is in the $x$-$z$ plane) of a point on the cloud surface is

given by

$$u=\frac{dx}{dt}=\frac{\partial x}{\partial t}\bigg|_z+w\frac{\partial x}{\partial z}\bigg|_t, \tag{5}$$

where $\partial x/\partial t|_z$ is the horizontal movement of the cloud edge at a particular altitude or temperature. In Fig. 13a this is represented by the horizontal, dashed vector. The term $\partial x/\partial z|_t$ is the slope of the cloud surface. Differentiating Eq. (5) with respect to $x$ and adding the result to a similar expression for $v$ differentiated with respect to $y$ results in

$$\frac{\partial u}{\partial x}+\frac{\partial v}{\partial y}=\frac{\partial}{\partial x}\left(\frac{\partial x}{\partial t}\bigg|_z\right)+\frac{\partial}{\partial y}\left(\frac{\partial y}{\partial t}\bigg|_z\right)+w\nabla_2\cdot\frac{\partial \mathbf{r}}{\partial z}, \tag{6}$$

if $w$ is assumed to be constant in the horizontal. The left-hand side of Eq. (6) is the horizontal divergence $D$ and the sum of the first and second terms on the right side is equivalent to the rate of isotherm expansion and the sum is equal to $N^{-1}dN/dt$. Therefore Eq. (6) can be expressed as

$$D=\frac{1}{N}\frac{dN}{dt}+w\nabla_2\cdot\frac{\partial \mathbf{r}}{\partial z}. \tag{7}$$

The second term on the right side of Eq. (7) is a product of the vertical velocity and a divergence term which is a function of the slope of the cloud surface. By incorporating a vertical lapse rate into the expression, the vertical coordinate is shifted to temperature in Eq. (8):

$$D=\frac{1}{N}\frac{dN}{dt}-w\left(-\frac{\partial T}{\partial z}\right)\nabla_2\cdot\frac{\partial \mathbf{r}}{\partial T}. \tag{8}$$

Information about the shape of the cloud top can be inferred from the satellite data, by determining the area encompassed by the then coldest isotherm when the next, still colder isotherm appears. If the area of the first isotherm is large the slope is small and if the area is small, this implies a relatively steep slope.

By defining a shape parameter $s$, such that

$$s=\left[\nabla_2\cdot\frac{\partial \mathbf{r}}{\partial T}\right]^{-1}, \tag{9}$$

one modifies Eq. (8) to become

$$D=\frac{1}{N}\frac{dN}{dt}-\frac{w}{s}\left(-\frac{\partial T}{\partial z}\right). \tag{10}$$

Using Eq. (1) to substitute into Eq. (14) a useful alternate expression,

$$D=\frac{1}{N}\frac{dN}{dt}+\frac{1}{s}\frac{dT}{dt}, \tag{11}$$

is derived. Eq. (10) states the relation among divergence, isotherm expansion, and vertical velocity. As will be shown, divergence is small compared to the other terms. The parameter $s$ is large when the cloud has steep slopes and small when the slope is shallow. An expression for $s$, which can be used with SMS/GOES IR data, is derived in the next section. Although not used in this study, information from the higher resolution visible channel could be used to help infer cloud top shape during daylight hours, especially near sunrise and sunset.

*c. Formulation for parameter s*

Information concerning the shape of the cloud top and therefore the shape parameter $s$ can be determined from the satellite IR data. The term in Eq. (9) is first expanded to obtain

$$\nabla_2\cdot\frac{\partial \mathbf{r}}{\partial T}=\frac{\partial}{\partial x}\left(\frac{\partial x}{\partial T}\bigg|_t\right)+\frac{\partial}{\partial y}\left(\frac{\partial y}{\partial T}\bigg|_t\right). \tag{12}$$

Assuming symmetry in the two directions results in

$$\nabla_2\cdot\frac{\partial \mathbf{r}}{\partial T}=2\frac{\partial}{\partial x}\left(\frac{\partial x}{\partial T}\bigg|_t\right). \tag{13}$$

The slope $\partial x/\partial T$ is approximated by

$$\frac{\partial x}{\partial T}\approx\frac{\xi N_w^{\frac{1}{2}}}{2\Delta T}, \tag{14}$$

where $\xi$ is the length represented by each satellite data point or pixel and $N_w$ the number of data points at $T_1$ when the next coldest temperature $T_0$ first appears. The expression assumes a square area. Therefore $\xi N_w^{\frac{1}{2}}/2$ is an estimate of the distance from the center of the isotherm area to the edge of the area. Divided by $\Delta T$ this produces an estimate of the slope in Eq. (14). The term $\Delta T$ is not always 1 K but is often approximated by 1.2 or 1.3 K because of the temperature void problem mentioned in Section 3.

The finite difference approximation for Eq. (13) is simply

$$2\frac{\partial}{\partial x}\left(\frac{\partial x}{\partial T}\right)\approx 2\frac{(\partial x/\partial T)_1-(\partial x/\partial T)_2}{\Delta x}, \tag{15}$$

where the derivatives at positions 1 and 2 are the slopes at opposite sides of the cloud top, and $\Delta x$ is the width of the area enclosed by the isotherm. Assuming they are equal in magnitude and opposite in sign and substituting Eq. (14) for the slope gives

$$2\frac{\partial}{\partial x}\left(\frac{\partial x}{\partial T}\bigg|_t\right)=\frac{2\xi N_w^{\frac{1}{2}}}{\Delta T\Delta x}. \tag{16}$$

Because the calculations to follow are for areas of

the size of $N=6$ to $N=30$ satellite data points, an intermediate value of $N=16$ was chosen as an appropriate size for the application of these formulas. Therefore, $\Delta x$ in Eq. (16) is assigned a value of $\sqrt{16}\xi$ or $4\xi$. Thus

$$\nabla_2 \cdot \frac{\partial \mathbf{r}}{\partial T} = 2\frac{\partial}{\partial x}\left(\frac{\partial x}{\partial T}\right) \approx \frac{N_w^{\frac{1}{2}}}{2\Delta T}. \tag{17}$$

A number of assumptions and approximations were needed to arrive at Eq. (17). A preliminary set of calculations using Eq. (11) with $s$ equal to the inverse of $N_w^{\frac{1}{2}}/2\Delta T$ from Eq. (17) resulted in an average value of divergence $D$ unrealistically small ($5\times10^{-5}$ s$^{-1}$). The calculations also indicated that because $D$ was the small difference between the two relatively large values [see Eq. (11)], a small bias in $s$ could drastically change the results for divergence. Therefore, the parameter $s$ is defined as

$$s = \alpha \frac{2\Delta T}{N_w^{\frac{1}{2}}}, \tag{18}$$

where $\alpha$ is a constant to be determined empirically through an analysis of Eq. (11).

The value for $\alpha$ was determined in the following manner. The terms $N^{-1}dN/dt$ and $dT/dt$ in Eq. (11) could both be calculated from the satellite data in a limited number of cases. Thirty-eight sets of variables were available for 19 elements. The parameter $s$ could also be calculated for these 38 cases from Eq. (18), at least in terms of $\alpha$. The average divergence $\bar{D}$ in Eq. (11) was calculated using the continuity equation for an incompressible fluid,

$$\bar{D} = -\frac{\partial \bar{w}}{\partial z}, \tag{19}$$

and a composite $w$ profile derived from the 38 cases using Eq. (1). The resulting $\bar{D}$ is $0.5\times10^{-3}$ s$^{-1}$. The mean value for $N^{-1}dN/dt$ over the 38 cases is $3.4\times10^{-3}$ s$^{-1}$. For $s^{-1}dT/dt$ the average magnitude is $(3.4\times10^{-3})/\alpha$, where $\alpha$ is the proportionality constant from Eq. (18). Using these average values to substitute into Eq. (11) results in

$$0.5 = 3.4 - \frac{3.4}{\alpha}, \tag{20}$$

or

$$\alpha = \frac{3.4}{2.9} = 1.2. \tag{21}$$

With $\alpha$ set equal to 1.2, the shape parameter $s$ can be calculated from satellite data from Eq. (18) in some cases. Fig. 14 displays the distribution of $s$ as a function of temperature for the 38 cases. The values span an order of magnitude with smaller values (flatter tops) predominating at lower temperatures (higher heights), as expected. The fitted curve was determined by first dividing the data set into five approximately interval-equal groups based on temperature. Average $s$ and temperature were calculated for each temperature interval and the linear regression curve was based on these five average points. This regression approach was adopted to reduce the effect of the relatively large number of points in the center region of the temperature range.

*d. Calculation of vertical velocity*

In Eq. (10), divergence is small compared to the other two terms, and to a rough approximation can be ignored to allow a direct relation between $w$ and $N^{-1}dN/dt$. However, the effects of divergence in Eq. (10) can be partially taken into account by noting that, in the 38 cases previously examined where we estimate all of the terms in Eq. (10), $D$ and $N^{-1}dN/dt$ appeared to be correlated. This is reasonable since $D$ is the horizontal expansion rate of a physical area and $N^{-1}dN/dt$ is the expansion rate of area within $T_{BB}$ isotherms. Thus $D$ can be approximated by

$$D \approx \beta \frac{1}{N}\frac{dN}{dt}, \tag{22}$$

where $\beta$ is set at 0.15, based on the average values for $D$ and $N^{-1}dN/dt$ for the 38 cases. Substituting Eq. (22) into Eq. (10) and solving for $w$ results in

$$w = \frac{0.85s}{(-\partial T/\partial z)}\frac{1}{N}\frac{dN}{dt}. \tag{23}$$

Eq. (23) provides a quick method of estimating vertical velocity even where there are no rapid decreases in temperature, or where an element can only be viewed for a short time.

Calculations of $w$ using Eq. (23) are made for each of the 39 elements at particular temperatures. A lapse rate midway between a smoothed ambient sounding and a constant (9 K km$^{-1}$) moist adiabatic rate is used. The $s$ values are selected from the fitted curve in Fig. 14 for the various temperatures. For temperatures $<T_{\min}$ a $w$ of zero is assigned. The calculated $w$ values are then averaged for the severe and non-severe elements and displayed in Fig. 15. The curves are fitted subjectively.

The mean $w$ for the severe elements is over 2.3 m s$^{-1}$ at 226 K or 10 km and decreases rapidly with height. The non-severe elements have nearly a factor of 2 smaller vertical velocity values. Divergence values calculated for the two curves from 10–12 km using the continuity equation are $1.0\times10^{-3}$ and $5.0\times10^{-4}$ s$^{-1}$ for the severe and non-severe elements, respectively.

These vertical velocity and divergence estimates are reasonable when it is recognized they are applicable

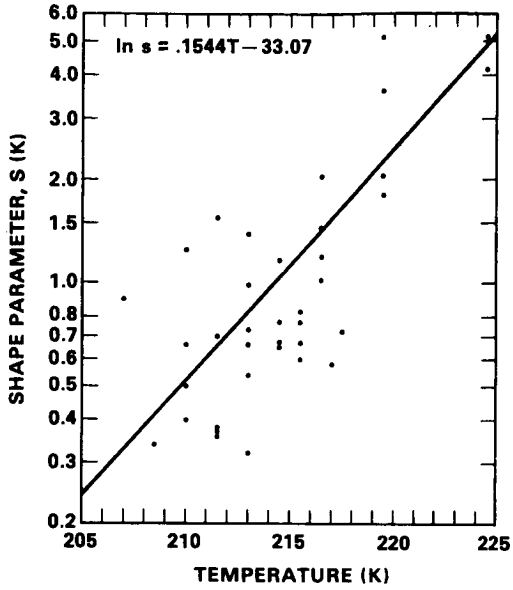


FIG. 14. Cloud top shape parameter $s$ as calculated using Eq. (18) as a function of temperature. The 38 points are from 19 elements.

to areas ~15 km in a side. Vertical velocity estimates are very scale-dependent, and it is difficult to find values applicable on a scale equal to that determined from the satellite data. Cloud top vertical velocities estimated from aircraft observations and radar data provide at least a starting point. Observing penetrating or overshooting domes from aircraft produces vertical velocity estimates of the order of 1 m $s^{-1}$. For example, Umenhofer (1975) calculates the ascent of an overshooting dome to be approximately 2 m $s^{-1}$ over a 5 min period before the Ethel, Texas, tornado of 14 May 1974 and Shenk (1974) shows another example with a $w$ of about 3 m $s^{-1}$. According to Shenk the mean diameter of the overshooting domes is approximately 5.5 km which corresponds to a circular area of 24 $km^2$. This area is an order of magnitude smaller than the appropriate satellite area of $15^2$ or 225 $km^2$. An example of $w$ determined from radar top ascent can be determined from Burgess and Lemon (1976; see their Fig. 5.6). Prior to the Union City, Oklahoma, tornado, the supercell top ascended at ~3 m $s^{-1}$. This velocity is applicable to an area about 1–2 km on a side.

From the preceding comparisons it is obvious that the vertical velocities at cloud top derived in this paper are smaller than those derived from other sources, but because they are applicable to an area much larger, they are still reasonable. Closer comparison between the satellite information and radar, aircraft or other observations is necessary for full validation.

## 8. Conclusions

Digital infrared data from a geosynchronous satellite (SMS 2) have been used to study thunderstorm growth rates on 6 May 1975 in relation to the occurrence of tornadoes and other severe weather. Areal expansions of cold areas, delineated by blackbody temperature isotherms, are shown to be useful in monitoring thunderstorm growth rates, even when there is minimal decrease with time of the lowest cloud top temperature.

An examination of five cloud elements having eight tornadoes clearly associated with them indicates that in seven of the eight cases the first report of the tornado took place during, or just after, a rapid expansion of cold areas indicating rapid ascent to the thunderstorm top on the scale observed by the satellite. The rate of ascent is estimated to be approximately 0.4 m $s^{-1}$, averaged over an area of about 15 km on a side.

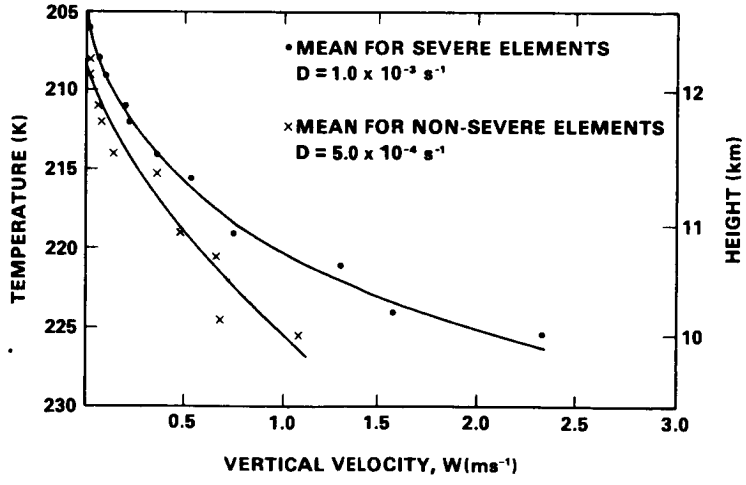


FIG. 15. Mean vertical velocity and divergence for severe and non-severe thunderstorm elements.

Thirty-nine thunderstorm elements in the analysis area were compared in relation to various parameters derived from the satellite data and the occurrence of severe weather. Although the ground truth used for defining the occurrence of severe weather may have errors, in this study two satellite-based variables are correlated with tornadoes and hail. These variables are the minimum cloud top temperature during the lifetime of the element and the logarithmic rate of increase of cloud top cold area.

The severe thunderstorm elements tend to be colder in terms of blackbody temperature and grow more rapidly than non-severe elements. For both variables the frequency distributions for severe and for non-severe elements were shown to be significantly different. A discriminant analysis using both variables showed that on one side of the discrimination boundary four out of 23 cases had severe weather, while on the cold temperature, fast growth rate side 11 out of 16 elements had reported severe weather. Therefore, based on this limited, dependent sample, these parameters, which are indicative of intense convection, are correlated with severe weather on the ground. A potential warning lead time of 30 min was estimated by comparing times of severe weather reports and times the satellite information met the derived criteria.

Equations were derived relating the areal expansion of blackbody temperature isotherms to vertical velocity and divergence. Mean vertical velocity profiles were calculated for severe and non-severe elements, with the results showing that the severe elements have a mean vertical velocity twice as large as the non-severe elements. The technique developed allows vertical velocities and divergence to be calculated from the satellite data on a horizontal spatial scale approaching that of individual thunderstorms. Information such as this will be useful in future work on tornado cloud top comparisons, further comparison of severe and non-severe elements, and for comparison with and verification of various types of cumulus models.

In summary, convection intensity information derived with short interval (~5 min) infrared digital data from a geosynchronous satellite can be statistically related to severe weather reports on the ground. Reasonable vertical velocity and divergence estimates can also be made from the data. The satellite data and the techniques developed have the potential to be a part of a severe thunderstorm detection and monitoring system.

## REFERENCES


Adler, R. F., and D. D. Fenn, 1976: Thunderstorm monitoring from a geosynchronous satellite. *Preprints 7th Conf. Aerospace and Aeronautical Meteorology*. Melbourne, Amer. Meteor. Soc., 307–311.

——, and ——, 1978: Thunderstorm vertical velocities estimated from satellite data. *Preprints Conf. Weather Forecasting and Analysis and Aviation Meteorology*, Silver Spring, Amer. Meteor. Soc., 206–210.

Arn, R. M., 1975: Anvil area and brightness characteristics as seen from geosynchronous satellites. M.S. thesis, Dept. of Atmospheric Science, Colorado State University.

Billingsley, J. B., 1976: Interactive image processing for meteorological applications at NASA/Goddard Space Flight Center. *Preprints 7th Conf. Aerospace and Aeronautical Meteorology and Symposium on Remote Sensing from Satellites*, Melbourne, Amer. Meteor. Soc., 268–275.

Burgess, D. W., and L. R. Lemon, 1976: Union City storm history. Union City, Oklahoma Tornado of 24 May 1973. NOAA Tech. Memo. ERL NSSL-80, 35–51.

Donaldson, R. J., R. M. Dyer and M. J. Kraus, 1975: An objective evaluator of techniques for predicting severe weather events. *Preprints Ninth Conf. Severe Local Storms*, Norman, Amer. Meteor. Soc., 321–326.

Fujita, T. T., 1973: Proposed mechanism of tornado formation from rotating thunderstorms. *Preprints Eighth Conf. Severe Local Storms*, Amer. Meteor. Soc., Denver, 191–196.

Goddard, B., and B. Remondi, 1975: Diagnostic tools for quality assessment of VISSR data. Central processing and analysis of geostationary satellite data. NOAA Tech. Memo. NESS 64, 48–58.

Lemon, L. R., D. W. Burgess and R. A. Brown, 1978: Tornadic storm airflow and morphology derived from single-doppler radar measurements. *Mon. Wea. Rev.*, **106**, 48–61.

Negri, A. J., D. W. Reynolds and R. A. Maddox, 1976: Measurements of cumulunimbus clouds using quantitative satellite and radar data. *Preprints Seventh Conf. Aerospace and Aeronautical Meteorology*, Melbourne, Amer. Meteor. Soc., 119–124.

Panofsky, H. A., and G. W. Brier, 1963: *Some Applications of Statistics to Meteorology*. The Pennsylvania State University Press, 224 pp.

Pearl, E. W., 1974: Characteristics of anvil-top associated with the Poplar Bluff tornado of May 7, 1973. SMRP Res. Pap. No. 119, The University of Chicago, 12 pp.

Pryor, S. P., 1978: Measurement of thunderstorm cloud-top parameters using high frequency satellite imagery. M.S. thesis, Dept. of Atmospheric Science, Colorado State University, 91 pp.

Purdom, J. F. W., 1971: Satellite imagery and severe weather warnings. *Preprints 7th Conf. Severe Local Storms*, Amer. Meteor. Soc., Kansas City, 120–137.

——, 1976: Some uses of high-resolution GOES imagery in the mesoscale forecasting of convection and its behavior. *Mon. Wea. Rev.*, **104**, 1474–1483.

Shenk, W. E., 1974: Cloud top height variability of strong convective cells. *J. Appl. Meteor.*, **13**, 917–991.

Sikdar, D. N., V. E. Suomi and C. E. Anderson, 1970: Convective transport of mass and energy in severe storms over the United States—an estimate from a geostationary altitude. *Tellus*, **22**, 521–532.

Umenhofer, T. A., 1975: Overshooting top behavior of three tornado-producing thunderstorms. *Preprints Ninth Conf. Severe Local Storms*, Norman, Amer. Meteor. Soc., 96–104.

Yuen, C.-W., 1977: Observations of severe convective storms from SMS-1 satellite. Studies of Soundings and Imaging Measurements, Final Scientific Report, Contract NAS5-21798, University of Wisconsin, 1–64.

Reprinted from JOURNAL OF APPLIED METEOROLOGY, Vol. 20, No. 3, March 1981
American Meteorological Society
Printed in U. S. A.

# Relation of Satellite-Based Thunderstorm Intensity to Radar-Estimated Rainfall

ANDREW J. NEGRI AND ROBERT F. ADLER

# Relation of Satellite-Based Thunderstorm Intensity to Radar-Estimated Rainfall[1]

ANDREW J. NEGRI AND ROBERT F. ADLER

*Laboratory for Atmospheric Sciences (GLAS), Goddard Space Flight Center, NASA, Greenbelt, MD 20771*

(Manuscript received 28 August 1980, in final form 13 December 1980)

ABSTRACT

Quantitative observations of thunderstorms in the midwest United States made with short-interval (5 min) geosynchronous satellite data are examined in relation to concurrent digital radar observations for one case study over a limited area. Individual thunderstorms are defined in the satellite infrared (IR) data by the location of relative minima in the equivalent blackbody temperature ($T_{BB}$) field. In a large majority of cases, these satellite-defined thunderstorms coincide with individual radar echoes. This agreement allows comparison of digital satellite and radar data for individual thunderstorms.

The evolution of individual thunderstorms in terms of radar echo and satellite-observed cloud features is examined. An examination of a number of storms indicated that the first low-level radar echo (18 dBZ) appeared when the satellite observed cloud-top minimum $T_{BB}$ had a mean of 246 K (7.4 km). As the storms evolve, larger reflectivities appear as the cloud tops penetrate upward to colder temperatures. Larger reflectivity values (>50 dBZ) begin as the storms approach and penetrate the tropopause.

Maximum radar reflectivity is shown to be correlated with satellite-based estimates of thunderstorm intensity. Thunderstorm top ascent rates in the 235–240 K (~8.8 km) region indicate the intensity of the initial storm updraft and are correlated with the maximum storm reflectivity with weak cells ($-dT_{BB}/dt$ of 1 K min$^{-1}$) having maximum reflectivity of 30–40 dBZ and strong cells (3–4 K min$^{-1}$) having echoes of ≥50 dBZ. The minimum $T_{BB}$ observed during the lifetime of the storm ($T_{\min}$), indicative of maximum storm top height, is also correlated to maximum storm rainfall. Storms with tops colder (higher) than the tropopause (212 K) have the highest rainfall rates in the severe storm situation examined here. The parameter $T_{\min}$ is also very well related to maximum volume rain rate as estimated from the radar data. Storms observed to reach temperatures lower than the tropopause temperature had volume rain rates of the order $10^3$ m$^3$ s$^{-1}$, compared to $10^2$ m$^3$ s$^{-1}$ for weaker storms.

## 1. Introduction

In this study the evolution of thunderstorms is investigated using 5 min interval geosynchronous satellite data and concurrent digital radar data. The objective of the research is twofold: to determine the evolution of rainfall in individual thunderstorms in relation to satellite-observed cloud characteristics; and second, to determine the potential and limitations of using this type of satellite data to estimate convective precipitation on a storm-by-storm basis.

The detection (and estimation) of convective rainfall from visible and infrared (IR) image data is a complex problem; precipitation must be inferred from measurements of the radiative properties of the cloud top without any direct information on the precipitation particles within the cells. Several schemes have been developed to use 30 min interval geosynchronous data to follow *cloud masses* and estimate their precipitation through empirical relations developed through comparison of satellite-observed cloud parameters and radar-observed precipitation. Arkin (1979) has found correlations as high as 0.89 between 6 h rainfall accumulation and the fractional coverage of the GATE B-scale array by clouds of varying (IR determined) heights. In more involved schemes Griffith *et al.* (1978) and Stout *et al.* (1979) have derived empirical relations between cloud area and echo area. Lovejoy and Austin (1979) found that a combination of IR and visible data was good for determining raining areas in convective regimes, but poor for determining rain rates, a conclusion also reached by Wylie (1979).

The satellite-based precipitation estimation schemes already mentioned have primarily been tested over large areas ($10^5$ km$^2$) and appear to produce better results over longer time periods (e.g., Woodley *et al.*, 1980). This latter technique follows the evolution of thunderstorms as depicted in the 30 min data based on the outline of the 253 K isotherm. For the analysis of individual, rapidly changing thunderstorms higher time frequency is needed.

In the current study, measurements of thunderstorm intensity determined from short-interval geosynchronous digital satellite data are compared to precipitation measurements from digital radar data. Adler and Fenn (1979a) have shown that satel-

[1] A preliminary version of this paper was presented at the AMS Nineteenth Conference on Radar Meteorology, Miami, FL.

lite-based thunderstorm intensity estimates, such as the rate of blackbody temperature isotherm expansion and minimum cloud top temperature, are correlated with ground reports of severe weather. They also have found a significant difference in the mean calculated cloud top ascent rates between cloud elements associated with severe weather reports and those with no such reports (Adler and Fenn, 1979b). Severe weather reports represent isolated events, often not well located in space and time. The use of simultaneous digital radar information, remapped into the coordinate system of a geosynchronous satellite, allows a direct comparison to be made between radar-observed precipitation and visible and infrared (IR) signatures at cloud top. Therefore, the evolution of precipitation in individual thunderstorms can be followed and compared to cloud evolution as observed with the satellite data.

## 2. Data and methodology

On 24 April 1975 intense, isolated convective storms developed in an area extending from central Oklahoma eastward to western Arkansas and Missouri during the late afternoon and early evening. The synoptic and mesoscale analyses will not be presented here, but are available in Negri and Vonder Haar (1980) and Maddox *et al.* (1980). The radar data consisted of reflectivities at 0° elevation angle for WSR-57 radars at Monett, MO; Kansas City, MO; and Oklahoma City, OK collected through the National Weather Service's Digitized Radar Experiment (D/ RADEX) program. The use of D/RADEX and its products is discussed in more detail by Saffle and Greene (1978)[2]. Areal resolution was 1.85 km by 2° of radar azimuth, and data were available nominally every 12 min in the form of nine discrete reflectivity levels. Conversion of radar reflectivity to rainfall rate was accomplished using the relation $Z = 200R^{1.6}$ (Marshall and Palmer, 1948), where $Z$ is the radar reflectivity factor ($mm^6\ m^{-3}$) and $R$ the rainfall rate ($mm\ h^{-1}$).

Utilizing the image processing capabilities of NASA's Atmospheric and Oceanographic Information Processing System (AOIPS), D/RADEX reflectivities were transformed from polar (radar) coordinates to a Cartesian array, retaining a resolution of $\sim 10\ km^2$ and were subsequently remapped into the geosynchronous satellite's coordinate system for direct comparison with cloud top features. The remapping was performed using bilinear interpolation with nearest neighbor resampling. The accuracy of the remapped echo positions is ~4 km and the areal extent of the remapped echoes is ~10% greater than the unremapped echoes, primarily in areas of low reflectivity.

The satellite data set consisted of 5 min interval (rapid scan) imagery from 2200 GMT on 24 April to 0100 GMT on the 25th. Visible channel (0.6 $\mu$m) radiances at 1 km resolution were used for navigation and for the detection of overshooting domes against the cirrus anvil background. Quantitative use of the imagery involved the use of infrared (11.5 $\mu$m) radiances at 8 km resolution. Radiances were converted to equivalent blackbody temperatures ($T_{BB}$) and for each storm two parameters were noted: the rate of minimum cloud-top temperature decrease ($dT_{BB}/dt$) and the minimum cloud-top temperature ($T_{min}$) observed during the thunderstorm's lifetime.

Examples of imagery used in this trispectral approach to thunderstorm evolution are given in Figs. 1 and 2. The first panel in each figure is a 1 km resolution visible image which delineates an area ~ 500 km on a side that encompassed most of the storms studied on this day. Fig. 1b and 2b contain radar reflectivities from the three D/RADEX sites, combined and remapped into the perspective of the SMS/GOES satellite. The third and fourth panels are two different representations of the infrared images for these storms. Figs. 1c and 2c have been enhanced by the digital enhancement used operationally by NOAA/NESS in the convective season. The definition of *individual thunderstorms* in the IR imagery often requires the contouring of every grey level (1 K) of temperature. Selected IR isotherms based on this approach are presented in the final panel.

The visible image at 2247 GMT (Fig. 1a) indicates three storms developing in south-central Oklahoma with several smaller storms forming on a flanking line to the west (refer to complex labeled C in Fig. 1a). As viewed in the IR (Figs. 1c and 1d) these main cells have corresponding $T_{BB}$ minima of 213, 214 and 220 K, respectively. Subsequent calculations are based on defining thunderstorm cells in terms of features often as small as those observed in Fig. 1c (the smallest resolvable feature represents an area of $\sim 100\ km^2$). The corresponding radar display remapped into satellite coordinates (Fig. 1b), indicates the precipitating portions of these storms, where grey represents reflectivities in excess of 25 dBZ and black represents those in excess of 46 dBZ or equivalent rainfall rates of 1.3 and 27 $mm\ h^{-1}$, respectively. In these young storms there is a one-to-one correspondence between the centers of maximum precipitation and the $T_{BB}$ minima. An analysis of satellite IR features versus radar imagery for these storms also is given by Adler and Fenn (1979b). Other young storms (north of B) also show the

[2] Saffle, R. E., and D. R. Greene, 1978: The role of radar in the flash flood watch warning system: Johnstown examined. *Preprints 18th Conf. Radar Meteorology*, Atlanta, Amer. Meteor. Soc., 468–473.

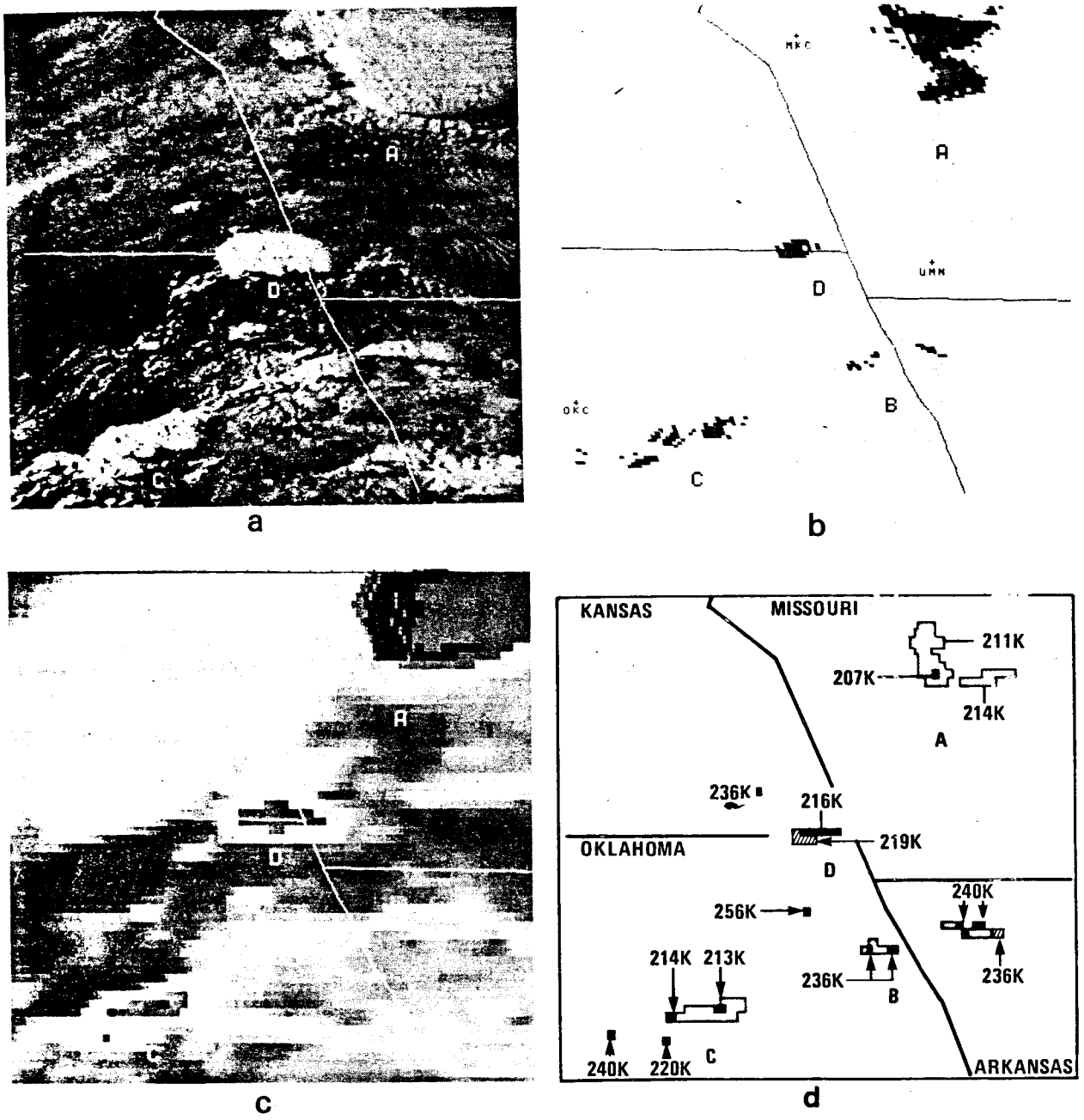


FIG. 1. (a) 1 km resolution visible image at 2247 GMT 24 April 1975. Area is ~500 km on a side. (b) Reflectivity from radars at Monett, Missouri; Oklahoma City, Oklahoma; and Kansas City, Missouri; 2248–2252 GMT, remapped to match satellite geometry. Grey: 24–45 dBZ, black: >46 dBZ. (c) 8 km resolution IR image enlarge to scale of visible image. Gray scale used is the digital enhancement used by NOAA-NESS (Mb curve). (d) Selected $T_{BB}$ isotherms from Fig. 1c utilizing the one degree temperature resolution available.

unique correspondence between individual echo and $T_{BB}$ minima. In a more mature storm (D) the relation is less obvious with the coldest $T_{BB}$ (216 K) located downwind of both the intense portion of the radar echo and the cumuliform towers seen in the visible image. The area of 219 K temperature over the precipitation maximum may be an overestimate of cloud-top temperature due to the response of the IR sensor along the thermal gradient between the hot cloud-free environment and the cold cloud top.

The coldest (207 K) and most intense storm at this time was the circularly shaped storm labeled A. The intense echo in this storm is located beneath a V-shaped pattern at cloud top (Fig. 1c), possibly re-

913

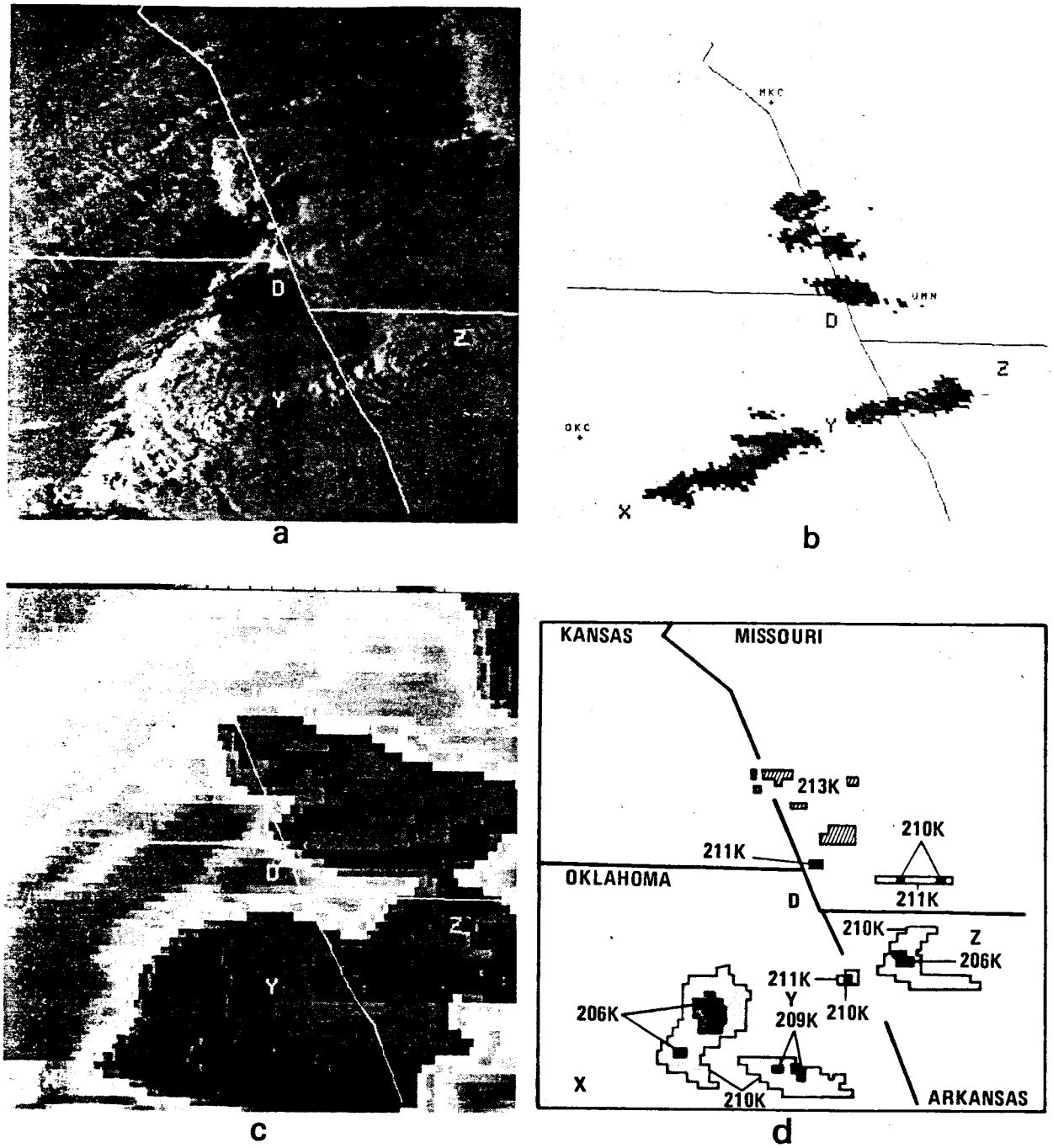


FIG. 2. (a)–(d) Composite data as in Fig. 1, except 0012 GMT 25 April 1975.

lated to blocking flow around the top of the storm. Other examples of this phenomena will be discussed subsequently.

The later stages of these storms is illustrated in Fig. 2, the corresponding imagery 85 min later at 0012 GMT on the 25th. The storms at C in Fig. 1 have evolved into the line of convective towers X-Y (Figs. 2a and 2b), while those at B have expanded to form the line Y-Z. The storm at D has moved eastward and new convection has taken place to its north. Storm A has moved rapidly southeastward out of the area of interest.

Between X and Y in Fig. 2, there is good agreement between the orientation of radar echoes and the line of overshooting tops in the visible image. However, one of the two IR cold features (the larger

92

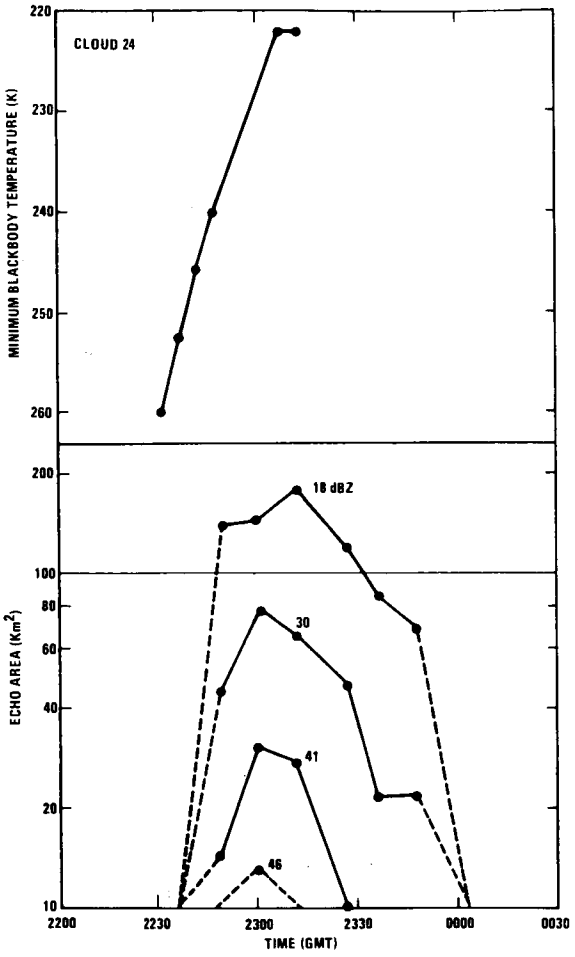


FIG. 3. Top: minimum blackbody temperature (K) versus time (GMT) for cloud 24. Bottom: Echo area (km²) at selected dBZ thresholds versus time (GMT) for cloud 24.

one) at 206 K is centered north of the X-Y axis, thereby giving a false impression of storm alignment. The storm associated with the large 206 K area has passed its maximum intensity, and the center of the cold area may not be colocated with the remaining updraft and rainfall. To the southeast of this area, a large, enclosed area of 209 and 210 K is also not apparently associated with any precipitation. The visible channel is particularly useful here in delineating these minima as smooth anvil material, however, it is evident that for mature storms the location of intense precipitation and the apportionment of precipitation by satellite estimation schemes cannot be based solely on infrared observations of the cirrus anvil.

Often, storms cannot be observed by the satellite until they penetrate the cirrus anvil generated by previous convection. Such is the case with the line of tops Y-Z, which is spatially correlated with the line of echoes and defined by two $T_{BB}$ minima of 206 and 210 K, both colder than the tropopause temperature and in this case are also colocated with the twin intense echo maxima. The 206 K storm between Y and Z also exhibits a V-notch pattern in the $T_{BB}$ field frequently associated with intense thunderstorms (Adler *et al.*, 1981). This type of feature is probably related to obstacle flow at anvil level around a strong, erect updraft. There is much evidence for such an effect (Browning and Foote, 1976). The warm (in terms of $T_{BB}$) area downwind is probably caused by the subsiding flow to the rear of the storm top, although there is a possibility it is related to the presence of lower stratospheric cirrus clouds formed downwind of the overshooting top. If these clouds were present, they would appear warmer than the anvil background.

In this study individual thunderstorms were defined in the satellite data using a sequence of IR and visible images and a technique described by Adler and Fenn (1979a,b). Points of relative minimum in $T_{BB}$ were tracked and defined as thunderstorms if they displayed good temporal continuity, a cumuliform appearance in the visible data, and a period of rapid change in the cloud top $T_{BB}$. These subjective parameters are indicators of deep convection and eliminate anvil debris and other anvil perturbations from consideration as thunderstorms. The thunderstorms so defined in the satellite data agreed very well with individual radar echoes, especially in the growing and maximum rainfall rate stages. During later stages, when the light rain areas on the periphery of the echoes merge as the storms form into lines, the identified IR features still are well associated with radar reflectivity maxima, although they are often not as well colocated as during earlier stages. Infrequent (in this study) mergers of storms are handled by defining the merged storms to be a continuation of most intense of the two previous storms. The defined lifetime of the weaker storm ends at the time of merger.

The high time-resolution satellite data are important in the identification and tracking of individual thunderstorms. From a solitary image, or from coarse time resolution (e.g., 30 min) data, it would become very difficult to eliminate $T_{BB}$ anvil features not associated with thunderstorm updrafts and it would also be more difficult to determine whether features on successive images, in fact, are manifestations of the same thunderstorm.

## 3. Evolution of individual thunderstorms

In this section three examples of evolving thunderstorms will be discussed with respect to satellite infrared and digital radar observations. The results of the analysis of a weak storm are shown in Fig. 3. The specific thunderstorm, cloud 24, is evident in

Fig. 1 in the extreme southwest corner of the images with a cloud top $T_{BB}$ of 240 K at 2247 GMT. The growing thunderstorm is noted in the IR data as an ascending cloud top (decreasing IR $T_{BB}$ values) going from 260 to 222 K over a 40 min period (Fig. 3). The time rate of $T_{BB}$ decrease ($-dT_{BB}/dt$) was approximately 1 K min$^{-1}$, a small value indicating a weak storm (Adler and Fenn, 1979b). After 2315 GMT the storm could no longer be identified in the IR data due to anvil cirrus from a stronger storm. The first echo (18 dBZ) appeared at 2236 GMT at a satellite-observed cloud-top temperature of 254 K (Fig. 3). Echo area expanded sharply and the maximum reflectivity increased from 2230 to 2300 GMT. Then a slower decrease began until the echo essentially disappeared at approximately 0000 GMT. Cloud 24 had a small, relatively weak echo and also appeared weak in the sequence of satellite digital data with slow (1 K min$^{-1}$) cloud top ascent rates and no observed temperatures lower than 222 K, 10° above tropopause temperature. Somewhat lower temperatures may possibly have been observed if the cloud top had not become blocked from the view of the satellite by anvil cirrus from an adjacent, stronger thunderstorm, but the minimum observed $T_{BB}$ is coincident with the radar-observed maximum intensity.

A second example is cloud 22, an intense hailstorm (7 cm diameter hail), which is evident in Fig. 1 as the easternmost cell in area C with a $T_{BB}$ of 213 K at 2247 GMT. Cloud 22 was a very intense thunderstorm with values of $-dT_{BB}/dt$ of 3.5 K min$^{-1}$ in the 235–240 K region (see Fig. 4a), putting it into the severe thunderstorm range (Adler and Fenn, 1979b). The first radar echo (18 dBZ) appeared at a $T_{BB}$ of 238 K at 2236 GMT, increased rapidly in magnitude to a reflectivity of 46 dBZ at 2248 GMT and to a storm maximum of 50 dBZ at 2300 GMT (Fig. 4b). Maximum reflectivity decreased after 2315 GMT. The satellite data indicate a thunderstorm top rapidly ascending through the upper troposphere until the tropopause (212 K) is approached and penetrated. Expansion of $T_{BB}$ isotherms in the anvil is displayed in Fig. 4c. During the period of rapid echo expansion and intensification (2240–2300 GMT) there is also a decrease in minimum $T_{BB}$ and an expansion of $T_{BB}$ isotherms in the storm's anvil. Nearly simultaneous with the maximum intensity of the radar echo (2300–2312 GMT) is the satellite observed highest (coldest) cloud top (206 K) at 2316 GMT. After this time the echo magnitude drops and by 2335 GMT the distinct $T_{BB}$ relative minimum associated with cloud 22 has disappeared into the broad background of the anvil. This would seem to indicate a weakening of the updraft. Significant rain, although not the heaviest, continues to fall even after the storm top sinks back into the cirrus background. This may be a persistent problem in any attempt to relate storm-scale satellite observations with convective rainfall in the mature phase of storms. On the other hand, the heavy rain did not begin until about the time the tropopause was reached by the cloud. This may be important because many storms cannot be observed until they penetrate the cirrus shield produced by previous convection (Adler and Fenn, 1979a). Thus, even these storms, only observable in their mature stage, can be identified near the time the heavy rain begins.

A third example, cloud 19, was a very intense storm in its mature stage, as can be seen in Fig. 2, where it is located in extreme northwest Arkansas. However, as shown in Fig. 5a, it began as a weak storm with a $-dT_{BB}/dt$ of approximately 1 K min$^{-1}$ in the 235–240 K height region. During the early portion of the storm, the radar echo also remained weak in agreement with the slow cloud-top ascent rate. At approximately 2300 GMT, the character of the thunderstorm as viewed by both the satellite and the radar changed, with a rapid intensification of the echo and a rapid expansion of the anvil edge and the $T_{BB}$ contours within it (Figs. 5b and 5c, respectively). The reason for this abrupt change from weak to intense storm is unclear, but may be due to a merger of updrafts, an enhancement of the low-level convergence through storm superposition over a low-level boundary, or other effect. The cloud temperature continues to decrease during this rapid echo growth period and finally reaches a minimum temperature of 204 K (~8 K below tropopause temperature), slightly before the appearance of the storm's maximum reflectivity, 62 dBZ.

In summary, the three example storms show the range of thunderstorms analyzed in this case study. Cloud 24 is a weak, short-lived storm with a small satellite-observed growth rate and a resultant small maximum height (minimum temperature). Moderate rain is only apparent for a short time and the entire life cycle of the radar echo is <90 min. The small size of the echo and the moderate rain values combine to produce a small volume rain rate. Cloud 22 is an intense, rapidly evolving severe thunderstorm with a large cloud-top ascent rate in the upper troposphere, a low minimum $T_{BB}$, and a large maximum reflectivity. The period of heaviest rain (50 dBZ) was relatively short (20 min). Cloud 19 evolved into one of the heaviest raining storms on this day, despite appearing initially as a slow growing, weak storm in both the radar and satellite data. The heaviest rain in cloud 19 was long-lived producing an enormous total storm rainfall.

## 4. Results for all storms

A total of 15 thunderstorms were analyzed with both the radar and satellite data on this day. While a majority of storms were observed in the data

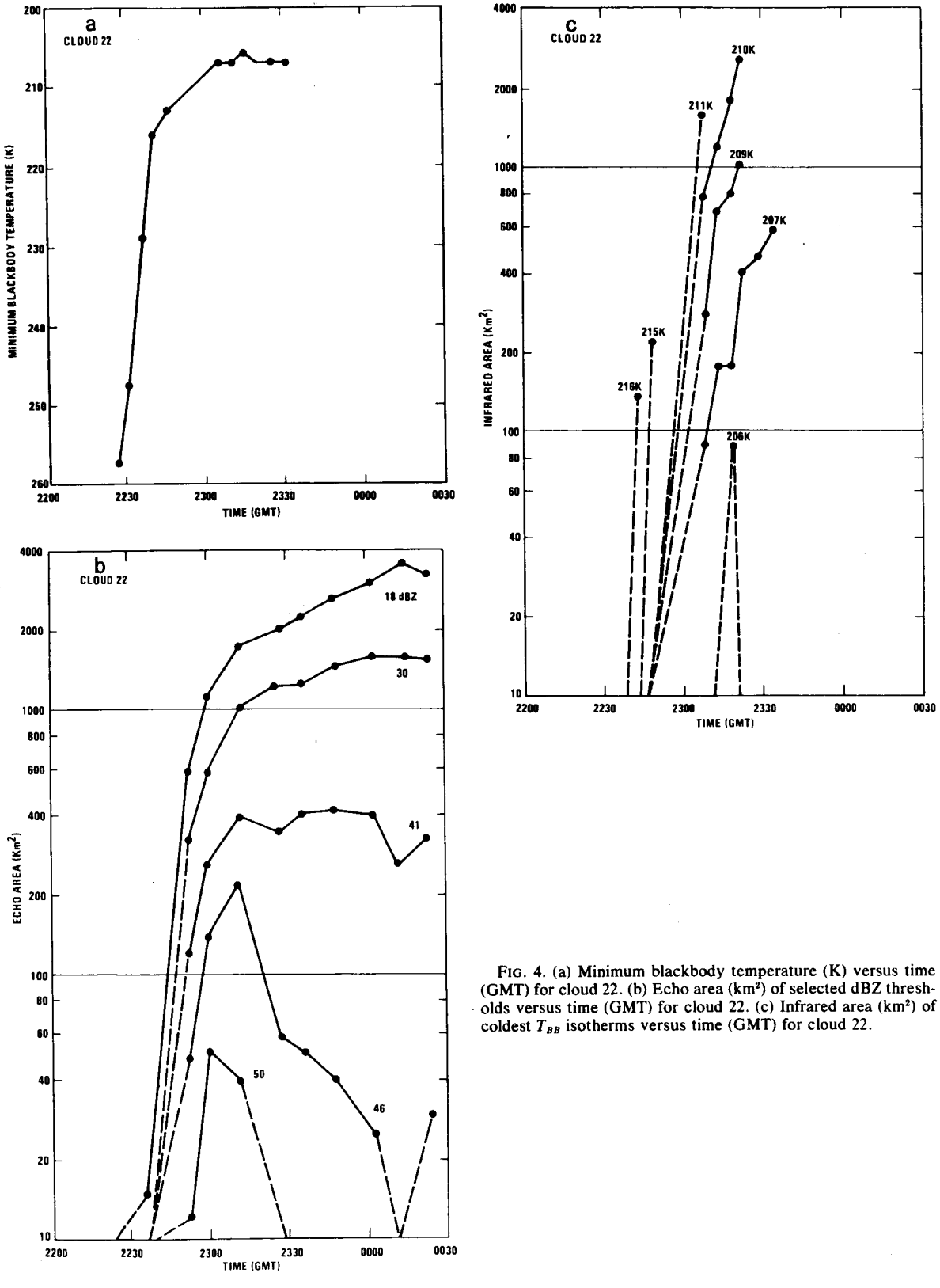


FIG. 4. (a) Minimum blackbody temperature (K) versus time (GMT) for cloud 22. (b) Echo area (km²) of selected dBZ thresholds versus time (GMT) for cloud 22. (c) Infrared area (km²) of coldest $T_{BB}$ isotherms versus time (GMT) for cloud 22.

throughout their entire lifetime, a few could only be identified after they penetrated a cirrus cloud deck. Other weaker cells became obscured during their later stages by anvil cirrus from other storms.

Fig. 6 is a scatter diagram showing the thunderstorm top $T_{BB}$ value at the time when the storm's reflectivity initially reached a particular magnitude. The correlation coefficient between these two parameters was −0.85. First echo (18 dBZ) was noted between 229 and 260 K with a mean temperature of 246 K. This mean temperature is equivalent to a height of ~7.4 km. Browning and Atlas (1965) and Atlas (1966) have examined this question of first echo height observationally and theoretically, respectively. The former study found the midpoint of the first echo in a Oklahoma severe storm to be at or above the −30°C (243 K) level, significantly colder than the similar level (~0°C) in non-severe convective clouds (Battan, 1963). Although the regression line in Fig. 6 also points to a first-echo height relationship, the results are not strictly comparable. As previously mentioned, the IR measurements tend to overestimate the true cloud temperature due to field of view and response problems. In addition, the D/RADEX data were available only at 0° elevation and 12 min intervals and archived with a minimum reflectivity of 18 dBZ. Thus, the derivation of a first-echo height relationship in the manner of Browning and Atlas (1965) was not possible.

As the storms evolve, greater reflectivities appear as the storms penetrate the upper troposphere to colder temperatures. Larger reflectivity values (>46 dBZ) begin as the storms approach and penetrate the tropopause. The large scatter of points along the $T_{BB}$ axis at the warm temperature end of Fig. 6 is partly due to the time resolution of the radar data (12 min). With rates of change of $T_{BB}$ of 2 K min$^{-1}$, a time error of 6 min in the appearance of a reflectivity value will translate into a 12 K error. At colder temperatures, where $-dT_{BB}/dt$ is smaller, the radar time resolution is less critical and the magnitude of the scatter decreases.

Adler and Fenn (1979b) have shown that one measure of thunderstorm intensity is the cloud top ascent rate ($-dT_{BB}/dt$) of storms in the 235–240 K (8.8 km) region. Storms with large ascent rates (>2 K min$^{-1}$) tend to have associated severe weather reports. Fig. 7 shows the relation of this satellite based intensity value and the maximum D/RADEX reflectivity, where each data point is an individual (numbered) thunderstorm. The reflectivity value used in the diagram must have existed in the storm for three successive scans (≥24 min); this eliminates short-lived higher values. For those storms observed by the satellite in their immature stage, there is a weak correlation (−0.66) between cloud-top ascent rate (proportional to updraft magnitude) and maximum reflectivity (Fig. 7), however, this correlation becomes 0.9 if the outlier (cloud 19) is excluded. This was an intense thunderstorm which *began* as an apparently weak cell and whose satellite and radar growth curves were presented in the preceding section.

The four storms viewed by the Oklahoma City radar with growth rates of <2 K min$^{-1}$ are clearly weak thunderstorms (clouds 24, 30, 31 and 32). These storms also had relatively light rain (as indicated by low maximum reflectivity). The more intense storms had progressively larger maximum reflectivity as the satellite parameter varied from 2 to 4 K min$^{-1}$.

Another satellite parameter that indicates storm severity (Adler and Fenn, 1979a) is the minimum blackbody temperature ($T_{min}$) achieved by the storm during its lifetime, observed by following an individual thunderstorm with rapid interval IR imagery. A plot of $T_{min}$ versus the corresponding observed maximum radar reflectivity for the 15 identifiable storms is presented in Fig. 8. Again the reflectivity maxima had to exist for at least 24 min. In addition, the occurrence of $T_{min}$ and maximum reflectivity was not necessarily simultaneous, but occurred on the average within 15 min of one another. Despite the small sample size, there is an excellent correlation (−0.92) between $T_{min}$ and maximum reflectivity. In addition, all storms observed to penetrate the tropopause (212 K) had reflectivities in excess of 50 dBZ. However, the relationship of rainfall intensity to storm intensity on the heavy rain side is probably more complicated and is influenced by such things as precipitation efficiency, entrainment, and interactions with the environment and neighboring storms.

A parameter particularly useful in identifying the flash-flood-producing thunderstorm is the volumetric rain rate (VRR). The VRR is computed from the radar data as follows: For every *isolated* radar echo, the Marshall-Palmer relation $Z = 200R^{1.6}$ is applied to each reflectivity value to obtain the equivalent rain rate (mm h$^{-1}$). The product of that rain rate with its areal extent (km$^2$) is then formed and summed over the nine possible reflectivity levels present in a storm. When echoes merge, the procedure remains the same, except that a subjective determination of the boundaries of the defined rain area is made with the point of maximum reflectivity remaining well inside the defined boundaries. This does not introduce significant bias because the lower reflectivities that exist on the edges of these subjectively defined echoes have small equivalent rain rates (0.5–10 mm h$^{-1}$) and hence comprise only a small percentage of the total VRR.

The comparison between VRR (m$^3$ s$^{-1}$), plotted on a logarithmic scale, and minimum $T_{BB}$ (Fig. 9) reveals a remarkably linear relationship. Each data point represents an individual thunderstorm defined

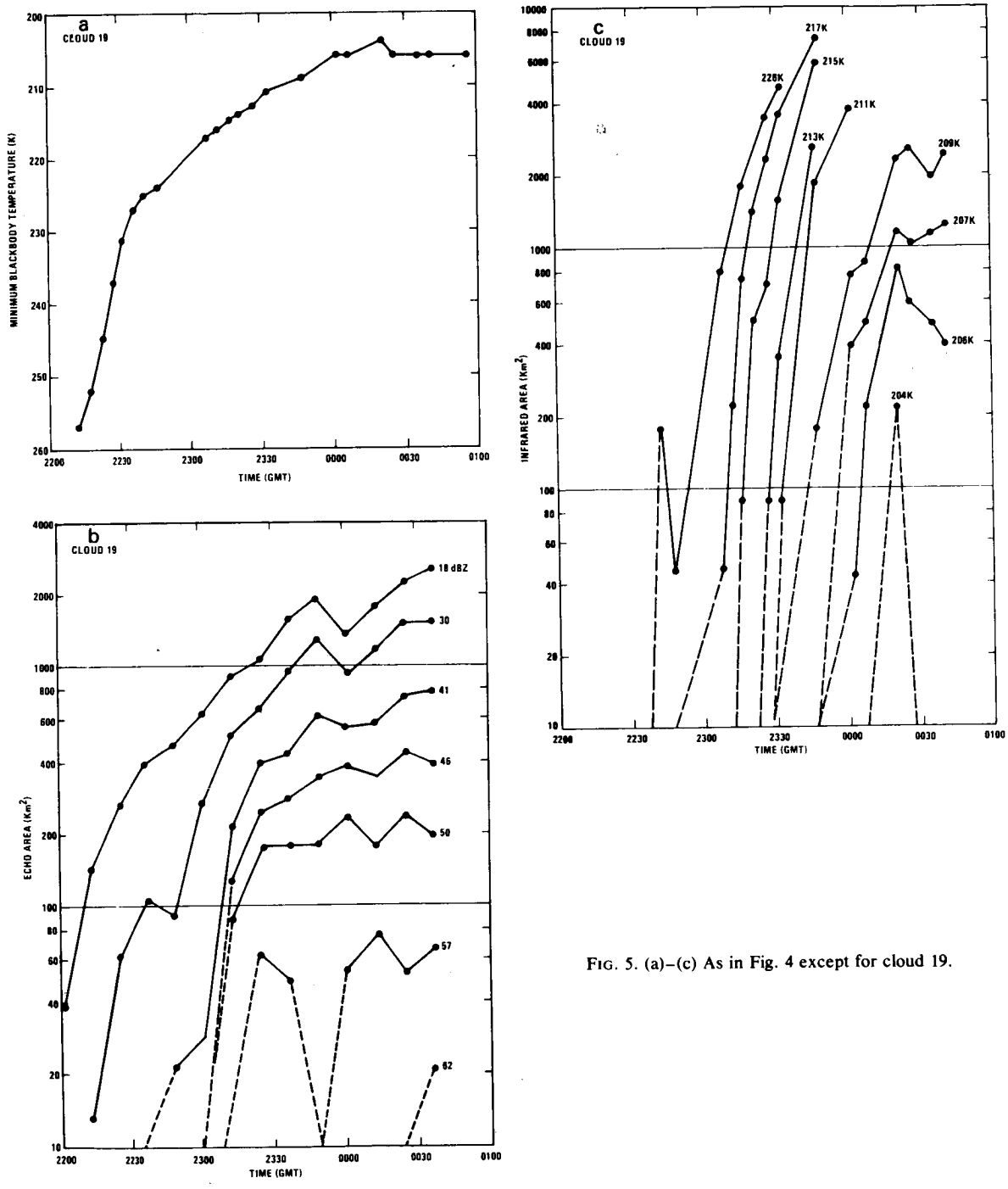


FIG. 5. (a)–(c) As in Fig. 4 except for cloud 19.

by a subjectively defined area centered on a reflectivity maximum and a $T_{BB}$ minimum determined to be associated with active convection. In general, the maximum VRR occurred nearly simultaneously with the maximum reflectivity. Storms that were observed to penetrate the tropopause had VRR values that, in general, were an order of magnitude larger than the warmer (lower) storms. The extremely good correlation ($-0.95$) suggests that we are relating two meaningful parameters in a physically sensible way. The $T_{\min}$ reached in each storm is a measure of the maximum updraft intensity averaged over a substan-

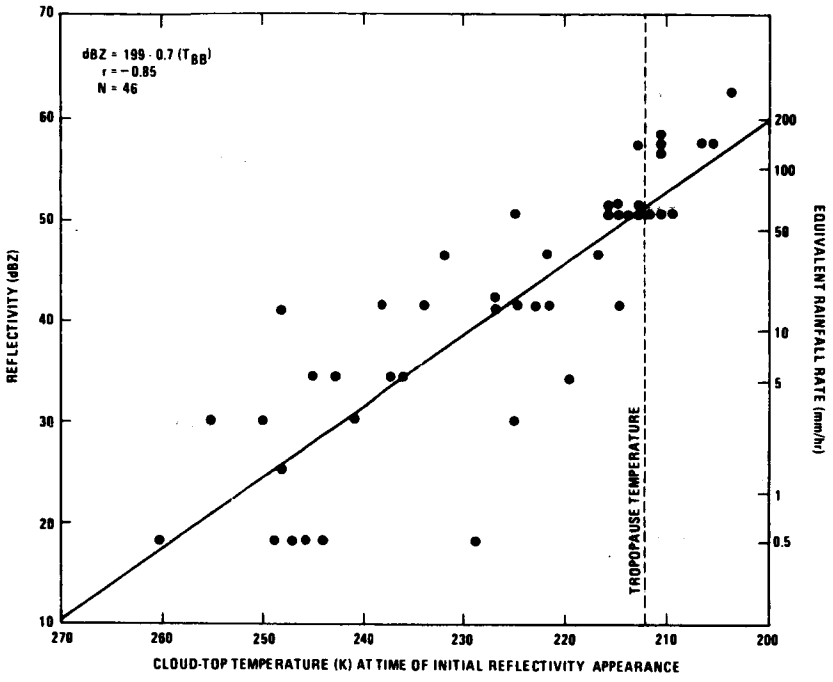


FIG. 6. Satellite-observed, thunderstorm top $T_{BB}$ at the time of first appearance of various radar reflectivity values for all storms observed on 24–25 April 1975.

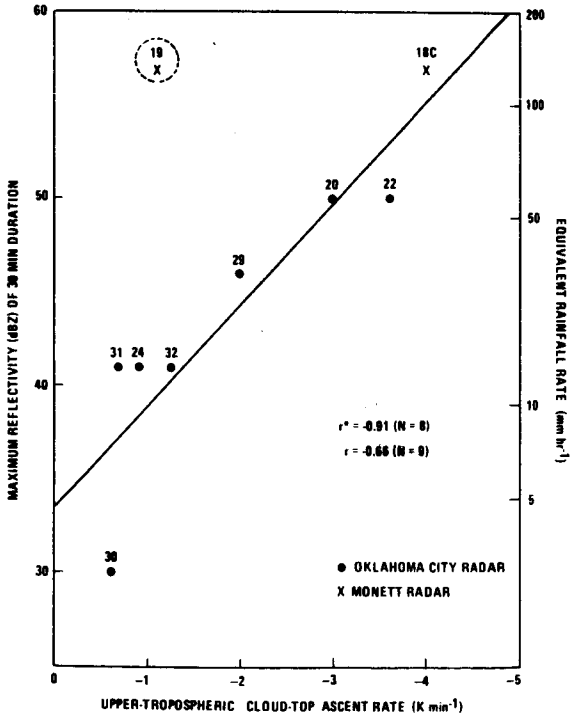


FIG. 7. Maximum observed reflectivity of 24 min duration (dBZ) versus cloud-top ascent rate (K $min^{-1}$). Each data point is an individual thunderstorm defined in both the IR and radar data. Scale on right shows equivalent rainfall rate (mm $h^{-1}$) using the relation $Z = 200R^{1.6}$.

tial area (~100 $km^2$), while the VRR is an integrated measure of the rainfall, because rain generated in the updraft may extend into areas beyond the updraft itself. These results are particularly interesting because they not only provide evidence of a very plausible physical relationship (to be addressed in subsequent research) but, if validated by further observations, provide a basis for eventual thunderstorm rainfall estimation from satellite data using a physically based method.

The flash flood potential of a thunderstorm through accumulation involves not only its instantaneous rainfall rate, but also its rate of motion. A comparison of the radar determined, accumulated rainfall for two storms with similar reflectivity patterns was undertaken. These storms are cloud 4, the large circularly shaped storm north of "D" in Fig. 1 and cloud 19, previously discussed, located in northwest Arkansas in Fig. 2. Cloud 4, whose echo centroid traveled at 18.8 m $s^{-1}$, left a narrow elongated swath of precipitation 10–20 mm deep across central Missouri, reaching a maximum of 28 mm. Cloud 19, however, moved somewhat slower (12.8 m $s^{-1}$), which allowed accumulations of 65 mm of rain along the Oklahoma-Arkansas border during the same time span. A similar difference in storm speeds is obtained by following the movement of the corresponding $T_{BB}$ minima in the satellite imagery. Thus the use of the IR data, applied on a thunderstorm scale, allows for not only the inference of storm intensity

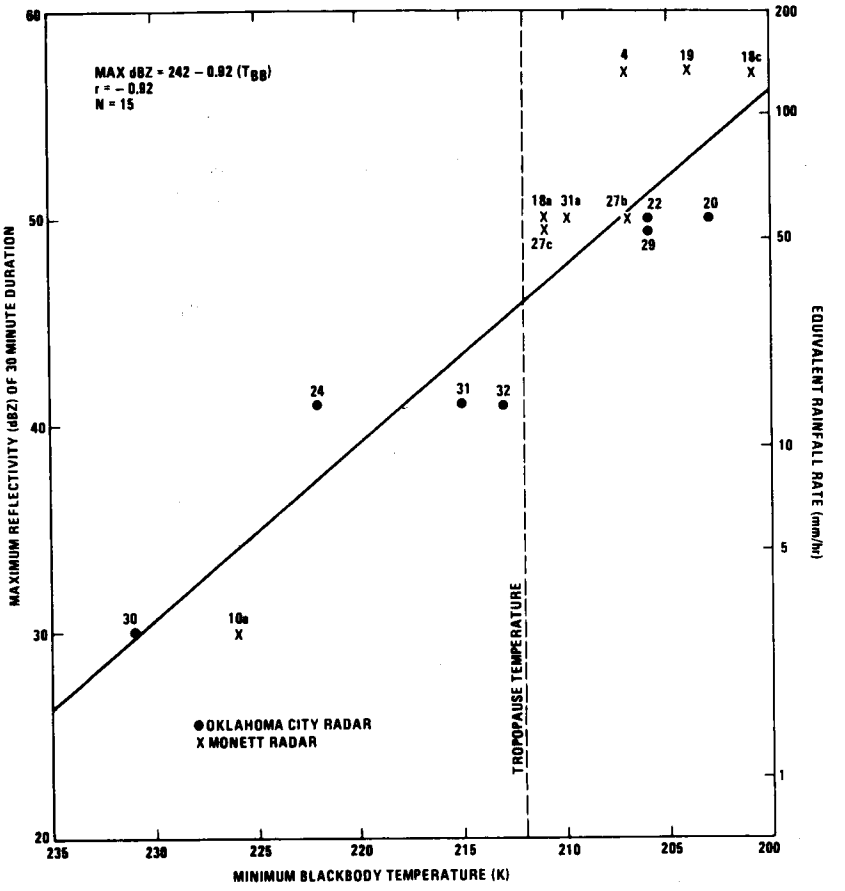


FIG. 8. Maximum observed reflectivity of 24 min duration (dBZ) versus minimum blackbody temperature. Note high reflectivities associated with tropopause penetrating storms.

but also the rate of storm motion. In addition, a new thunderstorm (cloud 31a) developed to the west of cloud 19 and by 0124 GMT maximum radar determined accumulated precipitation in parts of western Arkansas had reached 72 mm.

## 5. Conclusions

The purpose of this study was to investigate the evolution of thunderstorms of various intensities with short interval (5 min) geosynchronous digital satellite data and with digital radar data (12 min interval) to determine the potential and limitations of using geosynchronous satellite data to detect regions of convective precipitation and estimate the rainfall intensity. Thunderstorms on 24 April 1975, in eastern Oklahoma and surrounding areas were examined with SMS/GOES digital satellite data and D/RADEX digital radar data from the Oklahoma City, Oklahoma, Monett, Missouri, and Kansas City, Missouri radar sites. The radar data were remapped into satellite coordinates to facilitate display and comparison with the satellite data.

Individual thunderstorms were defined in the satellite IR data by location of relative minima in the equivalent blackbody temperature ($T_{BB}$) field. In virtually all cases, the locations of these satellite-defined thunderstorms coincided with individual radar echoes, notably in the early stages of development. This agreement allows comparison of digital satellite and radar data for individual thunderstorms.

Maximum radar reflectivity was shown to be correlated with satellite based estimates of thunderstorm intensity. Thunderstorm top ascent rates in the 235–240 K (8.8 km) region reflect intensity of the storm updraft and are correlated with the maximum storm reflectivity with weak cells ($-dT_{BB}/dt$ of 1 K min$^{-1}$) having maximum reflectivity of 30–40 dBZ (3–5 mm h$^{-1}$) and strong cells (3–4 K min$^{-1}$) having echoes of $\geq$50 dBZ (49 mm h$^{-1}$).

For mature storms, the maximum updraft intensity is estimated (in a relative sense) by the minimum $T_{BB}$ observed during the lifetime of the storm ($T_{\min}$). This satellite-based parameter is inversely related to maximum cloud height and was shown in this study

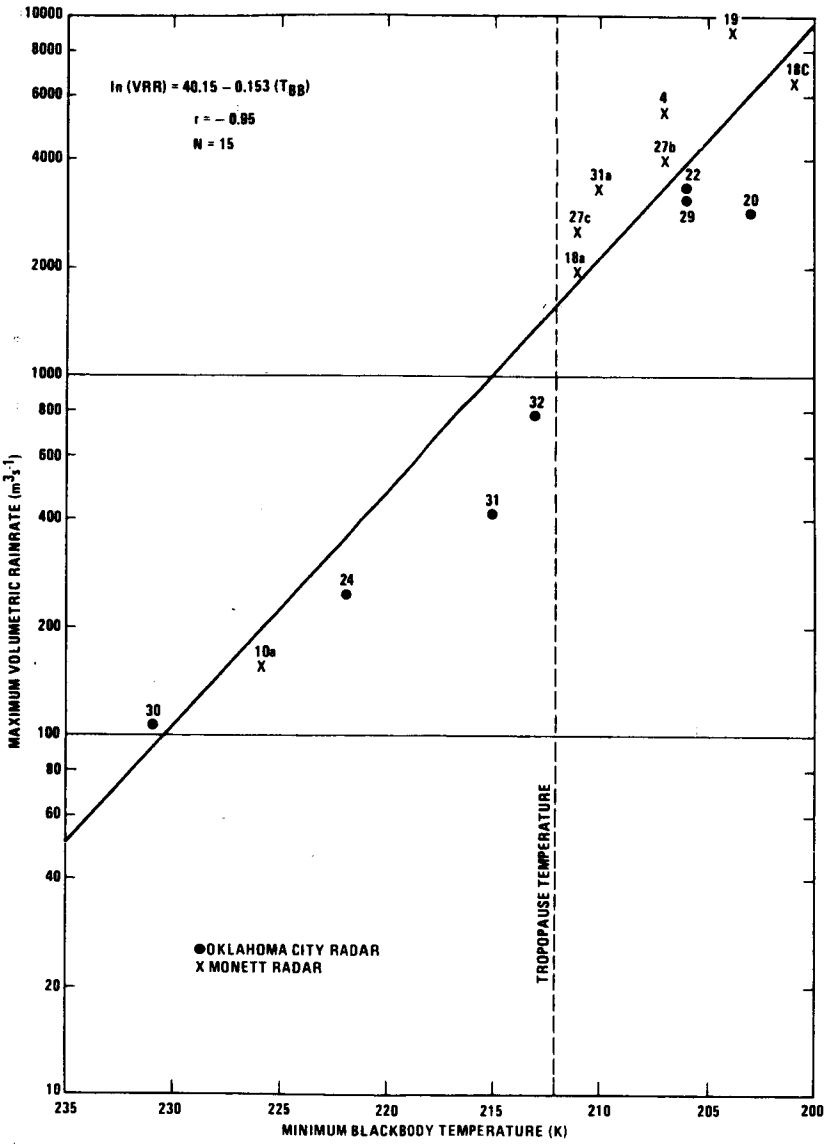


FIG. 9. Maximum volumetric rain rate ($m^3$ $s^{-1}$) versus minimum blackbody temperature ($T_{min}$). Numbers refer to individual storm identifiers. Note logarithmic ordinate scale.

to be correlated to maximum storm radar reflectivity. Storms with $T_{min}$ colder (higher) than the tropopause had the highest radar reflectivities. The parameter $T_{min}$ also is very well related to maximum volume rain rate as estimated from the radar data. Storms observed to reach temperatures lower than the tropopause temperature had volume rates of the order $10^3$ $m^3$ $s^{-1}$. A physical basis for these statistical relationships between the satellite-observed parameters and radar-estimated rainfall is currently being investigated.

The first low-level radar echo (18 dBZ) appeared when the satellite-observed cloud-top minimum $T_{BB}$ had a mean of 246 K (7.4 km). As the storms evolve, larger reflectivities appear as the cloud tops penetrate upward to colder temperatures. Larger reflectivity values (>50 dBZ) began as the storms approached and penetrated the tropopause (212 K).

These results indicate that inferences on thunderstorm updraft intensity can be made from such satellite derived quantities as $dT_{BB}/dt$ and $T_{min}$. For individual thunderstorms on 24 April 1975, such intensity measurements were related to storm precipitation rate as indicated by concurrent digital radar data. The conclusions support the effort to use satellite data to detect heavy convective precipitation

and estimate its magnitude, but emphasize the need for high time-resolution (3–5 min) data. The short interval data are necessary in order to 1) accurately define and follow individual thunderstorms unambiguously; 2) accurately measure rate of change parameters on a time scale appropriate for thunderstorms; and 3) accurately determine the minimum $T_{BB}$ achieved during the thunderstorm's lifetime. It must also be emphasized that the empirical relations between $T_{BB}$ parameters and rainfall rate derived here do not apply to *all* data points on an IR image, but only to the locations of defined thunderstorms in that image. In addition, we have examined only *one* day and only *one* area. These relationships may be qualitatively similar but quantitatively different elsewhere, notably in tropical regions.

*Acknowledgments.* The authors wish to thank Dr. David Atlas for his insightful comments and encouragement during this study. The input of Dr. Joanne Simpson is also appreciated. Much of the satellite image analysis used in this study was carried out by Douglas D. Fenn as part of a larger study. The manuscript was expertly typed by Carla Ridgeway and Janice Barnett.

## REFERENCES

Adler, R. F., and D. D. Fenn, 1979a: Thunderstorm intensity as determined from satellite data. *J. Appl. Meteor.*, **18**, 502–517.

——, and ——, 1979b: Thunderstorm vertical velocity estimated from satellite data. *J. Atmos. Sci.*, **16**, 1747–1750.

——, ——, and D. Moore, 1981: Spiral feature observed at top of rotating thunderstorm. Submitted to *Mon. Wea. Rev.*

Arkin, P. A., 1979: The relationship between fractional coverage of high cloud and rainfall accumulations during GATE over the B-scale array. *Mon. Wea. Rev.*, **107**, 1382–1387.

Atlas, D., 1966: The balance level in convective storms. *J. Atmos. Sci.*, **23**, 635–651.

Battan, L., 1963: Relationship between cloud base and initial radar echo. *J. Appl. Meteor.*, **2**, 333–336.

Browning, K. A., and D. Atlas, 1965: Initiation of precipitation in vigorous convective clouds. *J. Atmos. Sci.*, **22**, 678–683.

——, and G. B. Foote, 1976: Airflow and hail growth in supercell storms and some implications for hail suppression. *Quart. J. Roy. Meteor. Soc.*, **102**, 499–533.

Griffith, C. G., W. L. Woodley, P. G. Grube, D. W. Martin, J. E. Stout and D. N. Sikdar, 1978: Rain estimation from geosynchronous satellite imagery-visible and infrared studies. *Mon. Wea. Rev.*, **106**, 1153–1171.

Lovejoy, S., and G. L. Austin, 1979: The sources of error in rain amount estimating schemes from GOES visible and IR satellite data. *Mon. Wea. Rev.*, **107**, 1048–1054.

Maddox, R. A., L. R. Hoxit and C. F. Chappell, 1980: A study of tornadic thunderstorm interactions with thermal boundaries. *Mon. Wea. Rev.*, **108**, 322–336.

Marshall, J. S., and W. M. K. Palmer, 1948: The distribution of raindrops with size. *J. Meteor.*, **5**, 165–166.

Negri, A. J., and T. H. Vonder Haar, 1980: Moisture convergence using satellite derived wind fields; A severe local storm case study. *Mon. Wea. Rev.*, **108**, 1170–1182.

Stout, J. E., D. W. Martin and D. N. Sikdar, 1979: Estimating GATE rainfall with geosynchronous satellite images. *Mon. Wea. Rev.*, **106**, 1153–1171.

Woodley, W. L., C. G. Griffith, J. S. Griffin and S. C. Stromatt, 1980: The inference of GATE convective rainfall from SMS-1 imagery. *J. Appl. Meteor.*, **19**, 388–408.

Wylie, D. P., 1979: An application of a geostationary satellite rain estimation technique to an extratropical area. *J. Appl. Meteor.*, **18**, 1640–1648.

2B.2

Reprinted from Preprint Volume: Fourth Conference on Hydrometeorology, Oct. 7-9, 1981; Reno, Nev. Published by the American Meteorological Society, Boston, Mass.

# A SIMPLE PHYSICAL BASIS FOR RELATING GEOSYNCHRONOUS SATELLITE INFRARED OBSERVATIONS TO THUNDERSTORM RAINFALL

Robert F. Adler
Andrew J. Negri
and
David Atlas

Laboratory for Atmospheric Sciences
National Aeronautics and Space Administration
Goddard Space Flight Center
Greenbelt, MD 20771

## 1. INTRODUCTION

Estimation of convective rainfall from visible and window infrared (IR) satellite data continues to be of great interest, especially for heavy convective rain. While radar techniques provide an estimate of rainfall rate based on physical relations between the radar return signal and the cloud rainfall itself, the existing satellite-based IR and visible methods (e.g., Griffith et al., 1978, 1981; Scofield and Oliver, 1977; Stout et al., 1979) require rainfall rate information to be inferred from cloud top features and equivalent blackbody temperature ($T_{BB}$) data. The cloud/rainfall relationships used are determined empirically. The relations are derived for, and in turn applied to, time and space scales much larger than that associated with individual thunderstorms. One of the major drawbacks to such techniques is the lack of a strong physical basis, which makes it difficult to account for geographic, seasonal, and other variations.

Recently, there have been attempts to estimate the moisture budget (Park and Sikdar, 1980) and rainfall (Mack and Wylie, 1981) in large convective complexes by estimating anvil mass outflow from satellite data in order to calculate convective vertical mass transports. This information, in addition to moisture data (from rawinsonde) and an assumed entrainment factor, leads to an estimate of precipitation in the complex based on a simple model of cumulus mass and moisture transport discussed by Austin and Houze (1973). This type of approach has the potential to make physically-based estimates of large scale rainfall.

Major questions remain as to what is occurring on the scale of an individual thunderstorm and whether or not we can estimate any precipitation rate parameters on that scale. Negri and Adler (1981) have examined an admittedly small sample (15) of thunderstorms in Oklahoma and surrounding states on 1 day with short interval (5 minutes) GOES data and digital radar data. Individual thunderstorms were defined in the satellite IR data by the locations of relative minima in the equivalent blackbody temperature ($T_{BB}$) field. The feature must also maintain continuity, appear convective in the visible data and undergo a period of rapid change in $T_{BB}$ in order to be defined as a thunderstorm. In virtually all cases, the locations of these satellite-defined thunderstorms coincided with individual radar echoes, notably in the early stages of development. This agreement allows comparison of digital satellite and radar data for individual thunderstorms.

Maximum storm rainfall rate and maximum storm volume rainfall rate (VRR) were shown to be correlated with two satellite-based estimates of relative updraft intensity: the cloud top ascent rate ($-dT_{BB}/dt$) in the 235-240K (8.8 km) region, and the minimum $T_{BB}$ ($T_{min}$) achieved during the storm's lifetime.

The objective of this paper is to derive some simple expressions relating rainfall rate to thunderstorm updraft magnitude which can be interpreted in terms of the satellite observables. These expressions will then be compared to the observations presented by Negri and Adler (1981), hereafter referred to as NA. The hope is to establish the gross basis for physical relationships underlying the statistical results. Comparison of the satellite and radar observations with one-dimensional model results is also made.

## 2. RAINFALL RATE EQUATIONS

The process of rain formation in a thunderstorm is a complex interaction of storm dynamics and microphysics. However, the empirical results of NA indicate that at least for the one case study, the variation in maximum rainfall rate and maximum volume rainfall rate among storms is strongly related to the relative updraft intensity as indicated by the satellite-observed cloud top ascent rate or by $T_{min}$. The attempt in the following paragraphs will be to derive pertinent equations which can be evaluated with the satellite observations.

The total condensation rate C can be related to updraft intensity and moisture by starting with the moisture conservation equation,

assuming steady state conditions and horizontal uniformity and vertically integrating the equation from cloud base to cloud top.

$$C = -\int_A \int_{z_b}^{z_t} \rho w \frac{\partial q_s}{\partial z} \, dz da, \qquad (1)$$

where $\rho$ is the density, w is vertical velocity, $q_s$ is saturated specific humidity, and $z_t$ and $z_b$ are cloud top and base, respectively. The area A is the updraft area. Eq. (1) can also be expressed as

$$C = -\int_{q_0}^{0} \int_A \rho w \, da \, dq, \qquad (2)$$

where $q_0$ is the saturated q at cloud base (also equal to surface q, assuming unmixed ascent to cloud base) and zero is the approximate cloud top saturated q. Of course, cloud top q can be greater than zero, which should be kept in mind for generality. But for the data set of NA, the weakest, or shallowest, storm had a $T_{min}$ of 231K, or a cloud top $q_s$ of 0.4 g/kg, compared to a $q_0$ of 15 g/kg. Even for a cloud with a maximum top of only about 7 km, the cloud top $q_s$ would be approximately 10% of the cloud base value. Therefore, the assumption of q=0 at cloud top is acceptable for this exercise, but would have to be modified for shallow convection.

Since we are dealing with saturated processes in the cloud, all q's will be saturated and the subscript will be dropped for convenience. The density $\rho$ is assumed to be horizontally uniform and can be removed from inside the area integral. The updraft area integral

$$\int_A w \, da = \bar{w} A \qquad (3)$$

where $\bar{w}$ is the average w over the updraft area. The satellite observations, through the cloud top ascent rate, give us an estimate of an area-averaged w, but not simply averaged over the updraft area, but over the satellite IR Instantaneous Field of View (IFOV), approximately 10 km by 10 km. However, if w=0 outside the updraft and the satellite IFOV is always larger than the updraft area, then

$$\int_A w \, da = \bar{w} A = w_s A_s, \quad (A \leq A_s) \qquad (4)$$

where $w_s$ is the average vertical velocity over the area ($A_s$) of the satellite IFOV. Therefore, Eq. (2) becomes

$$C = -A_s \int_{q_0}^{0} \rho w_s \, dq \qquad (5)$$

The vertical coordinate q (actually $q_s$) is monotonic and has the characteristic that $\rho$ is approximately linear in q so that $\rho$ can be expressed as:

$$\rho = \alpha_0 + \alpha_1 (q/q_0) \qquad (6)$$

where $\alpha_0$ and $\alpha_1$ are constants appropriate for a particular moist adiabat $\theta_e$. The linear approximation is valid because both variables decrease exponentially with height. Figure 1 shows the relationship of $\rho$, $q_s$ and height along a moist adiabat ($\theta_e$=348K) and the linear approximation used. Along a moist adiabat $\rho$ is only a function of $q_s$ and a more complete formulation could use the derived relation.

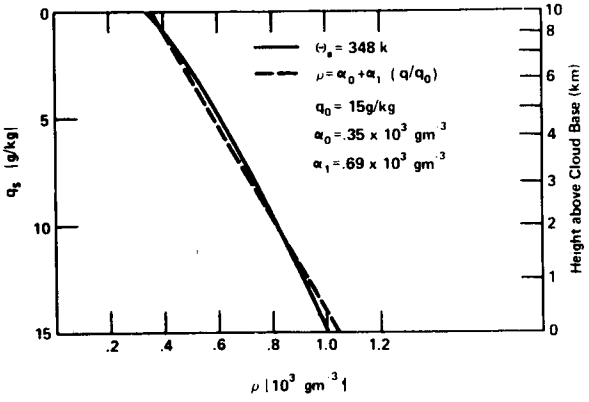


*Figure 1. Vertical profile of air density $\rho$ as a function of $q_s$ along the $\theta_e$=348K moist adiabat (solid line) and the linear approximation (dashed line) used in the calculations.*

The variable w (the subscript s is dropped for convenience) is parameterized in terms of maximum vertical velocity, $w_{max}$, so that

$$w = w_{max}(1-\beta \, q/q_0) \qquad (7)$$

This formulation gives $w=w_{max}$ at cloud top and a linear profile (with respect to $q_s$) down to $w=w_{max}(1-\beta)$ at cloud base, where $0 \leq \beta \leq 1$. The parameter $\beta$ will be determined by an additional constraint. A linear profile of w with respect to $q_s$ is a reasonable approximation as can be seen, for example, in the results of a one-dimensional cloud model run (Fig. 2). The w profile given by Eq. (7) does not include the decrease of w with height in the outflow layer at the top of the storm. However, this height region contributes very little to the condensation rate because of its low moisture values.

Substituting Eqs. (6) and (7) into Eq. (5) and integrating produces:

$$C = [(1 - \beta/2)\alpha_0 + (0.5 - \beta/3)\alpha_1] w_{max} \, q_0 \, A_s \qquad (8)$$

In this simple formulation, the total condensation rate, C, is proportional to the product of maximum updraft intensity and cloud base saturation specific humidity (also equal to surface specific humidity).

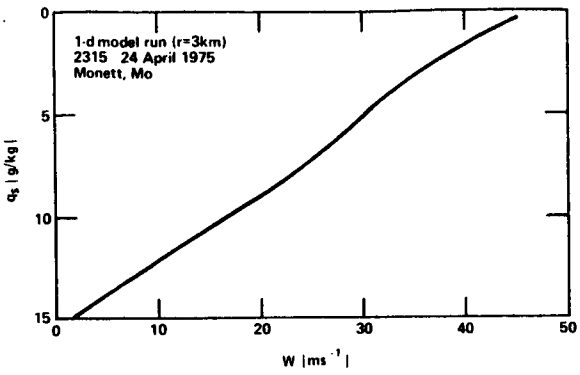


*Figure 2. Vertical profile of one-dimensional model vertical velocity plotted as a function of $q_s$ along the $\theta_e$=348K adiabat. The model velocity is nearly linear with respect to $q_s$.*

In order to determine β, we will assume that the only moisture source for the cloud is through cloud base. Since the system is assumed to be steady state, the flux of moisture through cloud base must equal the condensation rate, i.e.,

$$C = \rho_o w_o q_o A_s \qquad (9)$$

where the subscript denotes cloud base values. From Eqs. (6) and (7)

$$\rho_o = \alpha_o + \alpha_1 \text{ and} \qquad (10)$$

$$w_o = w_{max}(1-\beta) \qquad (11)$$

and Eq. (9) becomes

$$C = (\alpha_o + \alpha_1) w_{max}(1-\beta) q_o A_s \qquad (12)$$

Solving Eqs. (8) and (12) for β gives

$$\beta = \frac{\alpha_1}{\alpha_o + \alpha_1 4/3} \qquad (13)$$

For the April 24, 1975, case study appropriate constants for the density profile are $\alpha_o$=.35x10$^3$ gm$^{-3}$ and $\alpha_1$=.69x10$^3$ gm$^{-3}$. Substituting these values into Eq. (10) results in β=.54, which means that cloud base vertical velocity $w_o$=.46 $w_{max}$. At first, a vertical velocity profile with the cloud base value already nearly one-half of the maximum value seems unreasonable and would be if we were considering peak velocity values at each level. However, one must remember that we are dealing with an average value over a horizontal area larger than the updraft (the satellite IFOV ~100 km$^2$). In terms of vertical mass flux, this vertical velocity profile will give approximately constant mass flux with height, reasonable in our no entrainment model. For example, a $w_{max}$ of 4 ms$^{-1}$ (an intermediate value) corresponds to a $w_o$ of 1.8 ms$^{-1}$. Using an area of 100 km$^2$ and $\rho_o$ of 10$^3$ gm$^{-3}$ results in a cloud base mass flux estimate of 1.8x10$^{11}$ g s$^{-1}$, similar to an average value for hailstorms (2.3x10$^{11}$ g s$^{-1}$) calculated by Auer and Marwitz (1968) from aircraft data.

Substituting the values for $\alpha_o$, $\alpha_1$ and β into Eq. (8) gives

$$C = .475 \times 10^3 w_{max} q_o A_s \qquad (14)$$

where the constant has units of gm$^{-3}$.

The volume rainfall rate (VRR) will be less than the total condensation rate, C, due to various loss terms. This is expressed simply as

$$VRR = \frac{EC}{\rho_w} \qquad (15)$$

where $\rho_w$ is the density of water and E is the storm precipitation efficiency ($0 \leq E \leq 1$). Therefore,

$$VRR = .475 \times 10^{-3} E A_s w_{max} q_o \qquad (16)$$

Eq. (16) indicates that VRR is proportional to $w_{max}$. Since the area ($A_s$) is constant, this actually means that VRR is proportional to vertical mass flux. Cloud top ascent rates in the 235-240K (8.8 km) region as used by NA can be converted to estimates of equivalent $w_{max}$ through an appropriate lapse rate (Adler and Fenn, 1979). In this case, a lapse rate of 8.3 km$^{-1}$ was used which converts a cloud top ascent rate of 1K min$^{-1}$ to a $w_{max}$ of 2 ms$^{-1}$.

The 235-240K layer is used because it is intermediate to the warmer layers where the clouds are difficult to define and the colder layers where the ascent rates are affected by the tropopause. It is the layer with generally the largest ascent rates (Adler and Fenn, 1979). When we use the satellite cloud top ascent rates as a substitute for $w_{max}$ in Eq. (16) we are assuming that the ascent rate during the cloud growth stage is equal to the maximum vertical velocity (area-averaged) in the interior of the storm at a later time. This is probably not true, but the two parameters are correlated and the cloud ascent rates produce reasonable vertical mass fluxes (see previous paragraph).

Figure 3 shows the results of calculations with Eq. (16) with $q_o$=15 g/kg (a reasonable value for the case study) and E=1.0. The data points represent the eight storms in the case study (NA) where the cloud top ascent rate in the 235-240K layer could be observed along with the maximum radar-observed VRR (instantaneous) during the storm's lifetime. The calculated line follows the data reasonably well, although the more intense storms straddle the line while the weak storms fall significantly below the line. The instantaneous maximum VRR may overemphasize transient peaks in the rainfall. An average over a reasonable time period may make a better comparison with our calculated values. Therefore, a 30 minute average (3 radar observations) was calculated and plotted in Fig. 4. The calculated VRR's have been reduced by 15-20% by the time averaging.

The plots in Figs. 3 and 4, especially Fig. 4, indicate that the linear relation in Eq. (16) is a reasonable first approximation and that, for these storms, the VRR is roughly proportional to the vertical mass flux. Data points below the calculated line imply efficiencies (E) less than one. For the four intense storms, the

E value calculated from Fig. 4 is 80%, while the weak storms average 25%. Although the absolute value of the efficiencies should be treated very carefully because of all the assumptions in the derivation of the theoretical VRR and in the radar and satellite data analysis, the trend toward higher efficiencies for more intense, larger storms is realistic because of the relation of entrainment to storm or plume size (Turner, 1962).

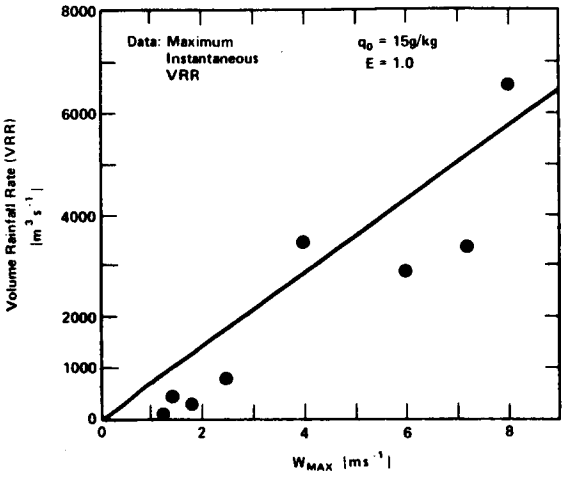


*Figure 3. Volume rainfall rate (VRR) calculated as a function of area-average $w_{max}$ from Eq. (16). Dots represent observations from NA of maximum instantaneous VRR and satellite-observed cloud top ascent rates.*

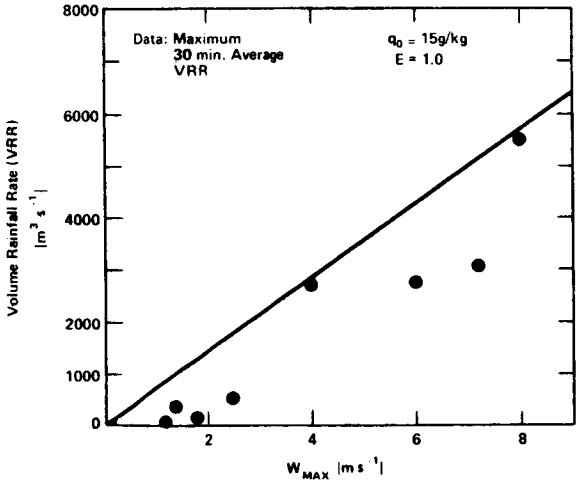


*Figure 4. Same as Fig. 3 except VRR observations (dots) are time averages over 30 minutes.*

Often a storm's cloud top ascent rate in the 9 km region cannot be measured because of anvil cirrus produced by previous convection. However, $T_{min}$, the minimum temperature achieved during a storm's lifetime, can usually be observed, especially in intense storms. Because this parameter is a relative measure of maximum storm height, it is also a proxy variable for $w_{max}$. A relation between $T_{min}$ and $w_{max}$ can possibly be derived through analysis of a one-dimensional cloud model (see section 3), or empirically derived as depicted in Fig. 5, where a curve is fitted to the satellite-based $w_{max}$ and $T_{min}$ data for eight storms. The empirical relation

$$w_{max}=5.32\times10^{-3}(237-T_{min})^2+.08 \qquad (17)$$

can then be substituted into Eq. (16) to obtain

$$VRR=4.75\times10^{-4}[5.32\times10^{-3}(237-T_{min})^2+.08]E\ q_o\ A_s \qquad (18)$$

The curve is plotted in Fig. (6) along with the 30 minute average VRR data. Again, the weak storms fall considerably below the curve while the intense storms scatter about the curve. Points falling above the curve imply efficiencies greater than 1.0, which are only possible if there is an additional source of moisture above cloud base and there are no moisture losses, such as outflow in the anvil.

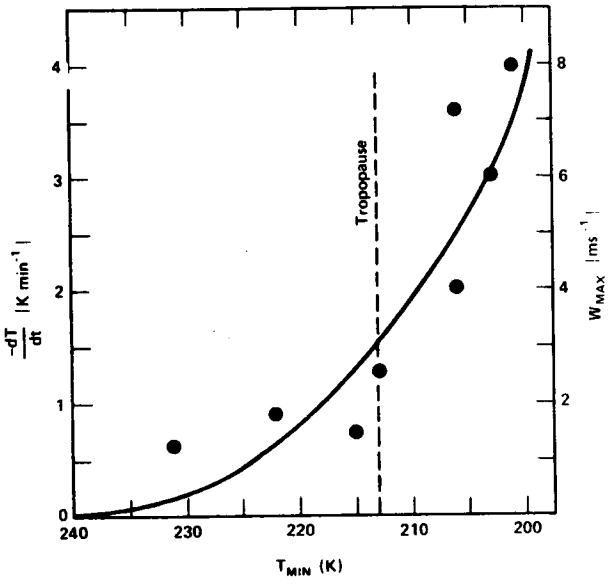


*Figure 5. Empirical relation of satellite-observed cloud top ascent rates to satellite-observed minimum $T_{BB}$, $T_{min}$, for storms in NA.*

The calculated curve, Eq. (18), generally follows the trend of the data and the increase in slope as lower $T_{min}$ values are approached. However, it does not appear to capture the sharp change in slope around the tropopause temperature (214K). This is partially because the empirical relation between $w_{max}$ and $T_{min}$ (Eq. (17)) smooths out the transition.

The apparent trend in efficiency is again present in Fig. 6. One term affecting efficiency is entrainment, and entrainment is usually parameterized as inversely proportional to cloud horizontal size. Since cloud width is related to cloud depth (as indicated by $T_{min}$),

we should be able to parameterize the entrainment and the efficiency in terms of cloud size. A modification to Eqs. (8) and (18) incorporating an entrainment parameterization has been derived, but is not presented here due to lack of space. The modification reduces the calculated rainfall for the small clouds and tends to bring the calculated values into better relative agreement with the observations.

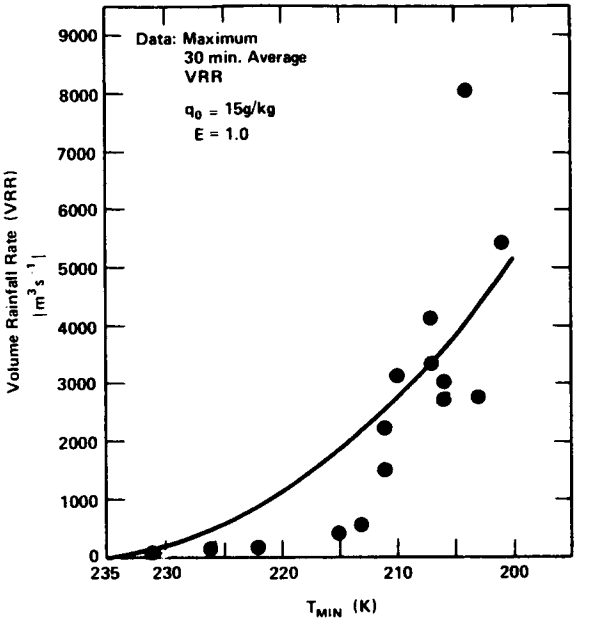


*Figure 6. Volume rainfall rate (VRR) as a function of $T_{min}$. Solid curve calculated from Eq. (18). Dots are 30 minute average maximum VRR adapted from NA.*

Other factors affecting the precipitation efficiency include vertical shear and the environmental humidity. Empirically, efficiency decreases with increasing shear (Marwitz, 1972; Foote and Fankhauser, 1973). In our case study, the shear from cloud base to tropopause is $3.3 \times 10^{-3}$, which converts to an efficiency of approximately 35%, using the diagrams in the referenced papers. This is reasonably close to the average value over the range of our case study thunderstorms, but significantly below that for our intense storms.

A dry environment decreases the efficiency in two main ways, as discussed by Brown and Klemp (1980) in their analysis of three-dimensional cloud model water budgets. Evaporation of the cloud edge and entrainment of the dry air reduces updraft size and intensity, and the cloud, therefore, processes less water. Also, the evaporation of rain before reaching the ground is greater with a drier environment. Although the two shear conditions examined in Brown and Klemp's study were not indicative of the range of possible shears, their results indicated that the moisture effect on efficiency was more important than the effect of shear.

## 3. INITIAL COMPARISONS WITH ONE-DIMENSIONAL MODEL RESULTS

The comparison of one-dimensional model calculations with the simple formulations of section 3 and with the observations in NA has two general purposes. First, it is the initial step in trying to verify the simple relations in section 2 with more complicated convection models. Ultimately, the moisture budgets of simulated three-dimensional model storms must be examined to help determine the role of various factors (e.g., shear, environmental humidity). This work has been started by Brown and Klemp (1980).

The second purpose has to do with the transportability of the relations in section 2. Eq. (16) seems to produce an upper bound for the data (see Fig. 4) and its linear form approximates that of the small data set. Therefore, the rainfall is approximately proportional to the vertical mass flux, as indicated by the area average $w_{max}$. Therefore, if we can make an estimate of a storm's vertical mass flux, we can in turn make an estimate of the upper bound in rainfall (assuming knowledge of the moisture source). However, from satellite observations, our most common measure of relative updraft intensity is $T_{min}$. With the present data set, we determined the $T_{min}$/mass flux ($w_{max}$) relation empirically (Fig. 5). However, this same relation will not hold under other climates or even under other synoptic conditions. A $T_{min}$ of 210K in mid-latitudes with a tropopause temperature of 215K implies a greater vertical velocity than the same $T_{min}$ in the tropics with a colder (higher) tropopause. The one-dimensional model may provide the basis for determining the $T_{min}$/mass flux relation applicable under particular conditions, and therefore, help make Eq. (16) transportable to different environmental conditions and usable with the satellite-observed $T_{min}$.

The Simpson-Wiggert (1969) model was run on the Monett, MO sounding for 2315 on April 25, 1975, for comparison with the data set from NA.

Five runs for different updraft radii were made to produce clouds growing to various heights. A summary of results is shown in Table 1. The peak vertical velocity ranges from 14 to 50 $ms^{-1}$. This is a reasonable range of vertical velocities for moderate to very intense thunderstorms. For comparison with the satellite cloud top ascent rates, the model $w_{max}$ is converted to an area average over 100 $km^2$, by assuming a uniform peak velocity over the updraft area and zero outside of that. This produces the $\bar{w}_{max}$ in Table 1, which has values closer to those of the satellite estimates which have a range from 1.2 to 8.0 $ms^{-1}$.

The model rainfall rate is calculated by dividing the model precipitation production by the time required for parcel ascent from cloud base to cloud top, in this case study estimated by cloud depth divided by $w_{max}/2$. The model VRR is simply the rainfall rate multiplied by updraft area. Figure 7 displays model VRR versus $w_{max}$ (model) where the line is drawn through the model calculated points (x's) and the dots are the data from NA. The model results are very similar to that shown in Fig. 4 and again indicate that the VRR is proportional to vertical mass flux under

TABLE 1. Summary of Results for One-dimensional Cloud Model Runs

| | Updraft Radius (km) | | | | |
|---|---|---|---|---|---|
| | 0.5 | 1.0 | 2.0 | 3.0 | 4.0 |
| Cloud Depth (km) | 8.6 | 11.1 | 12.6 | 13.4 | 13.8 |
| $T_{min}$ (K) | 217 | 200 | 188 | 185 | 182 |
| $w_{max}$ ($ms^{-1}$) | 14 | 22 | 36 | 45 | 50 |
| $\bar{w}_{max}$ ($ms^{-1}$) | 0.1 | 0.7 | 4.5 | 12.7 | 25.1 |
| Rainfall Rate ($mm\ h^{-1}$) | 153 | 340 | 611 | 774 | 851 |
| VRR $m^3 s^{-1}$ | 33 | 297 | 2133. | 6079. | 11882. |

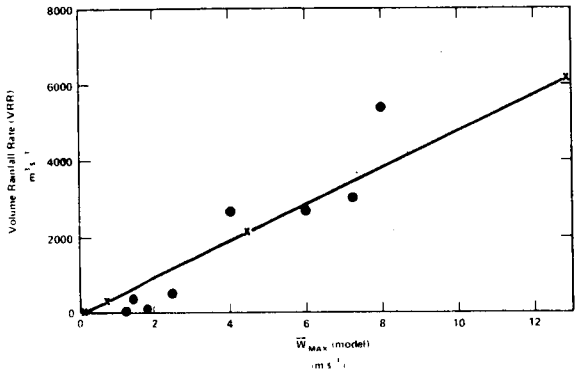


*Figure 7. Volume rainfall rate (VRR) computed from the one-dimensional cloud model output as a function of area-average (100 km$^2$) model maximum vertical velocity (solid line connecting calculation points, x's). Dots are radar VRR's and satellite cloud top ascent rates as in Fig. 4.*

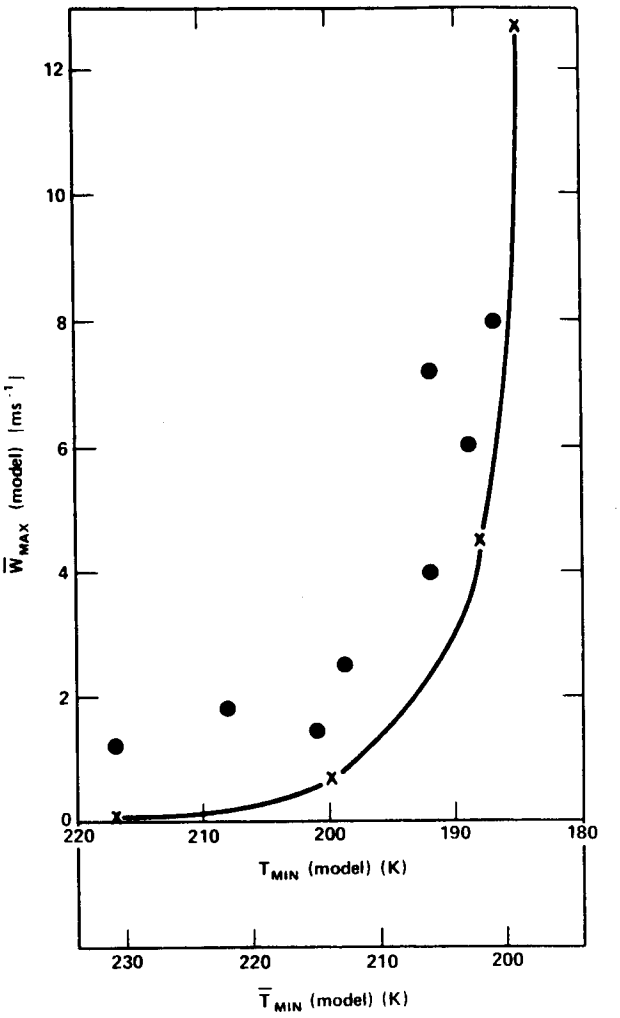


*Figure 8. Model area-average $w_{max}$ as a function of model $T_{min}$ and model $\bar{T}_{min}$ (which takes into account a temperature shift to make the model output more comparable to the satellite observations). Data points are satellite observations from Fig. 5.*

the same environmental conditions. It will be interesting to determine if a similar simple relation exists with three-dimensional model output.

The critical vertical velocity/$T_{min}$ relation is shown in Fig. 8. This curve is similar to that in Fig. 5 (satellite observations), except for the obvious difference that the model $T_{min}$'s are significantly lower than the satellite observations. This is because the model $T_{min}$ represents a very small horizontal dimension at the center of cloud top, while the satellite $T_{min}$ represents an average area over a large (100 km$^2$) area, therby being necessarily much warmer. In addition, there may be differences because the model $T_{min}$ is an updraft core temperature while an infrared radiometer will measure cloud surface temperature. The relation of satellite $T_{min}$ to smaller scale $T_{min}$ has been examined by Adler et al. (1981) using aircraft overflight data with a radiometer similar to that on SMS/GOES. The results indicate that there is roughly a 14K difference between the satellite $T_{min}$ and the small scale (100 m x 100 m) $T_{min}$ due to the area average effect. Thus, a second horizontal scale has been added to Fig. 10 with

$$\bar{T}_{min}\ (\text{model}) = T_{min}\ (\text{model}) + 14 \qquad (19)$$

to allow a better comparison of the model results with the satellite observations (plotted as dots in the figure). The magnitude of the offset is based on only a few cloud observations on one case study day, and should not be considered general.

The NA satellite data set had $T_{min}$ ranging from 231K to 201K. This gives approximate agreement with the model results ranging from updraft radius 0.5 km to a radius between 2 and 3 km. The model results for $\bar{w}$ (even with the shift of $T_{min}$ axis) are low compared to the satellite cloud top ascent rates (Fig. 8). The difference is very significant at the warm or less intense end of the range. The difference is unexplained at this time, but may be the result of the assumptions being made in order to make the variables comparable. An additional shift of 3K would produce significantly better agreement and is not out of the question according to Adler et al. (1981). However, the shape of the curve represents the trend of the data well.

Figure 9 shows the curve representing the model-computed VRR and the NA data set plotted on the $\bar{T}_{min}$ scale. The model calculations handled in this way grossly underestimate the rainfall in the intense storms, but the curve has the sharp change in slope apparent in the data.

Finally, Fig. 10 shows the VRR/$T_{min}$ relation when Eq. (16) is used and $w_{max}$ is substituted for by the $w_{max}/T_{min}$ model relation of Fig. 9 instead of the satellite empirical relation. Again, the rainfall is underestimated, but not as badly. However, since the VRR/$w_{max}$ relations of both Figs. 4 and 8 are more reasonable, the failure must be in the $w_{max}/T_{min}$ connection. Obviously, more work must go into understanding the model results (both one-dimensional and three-dimensional) and their relation to the satellite observations.

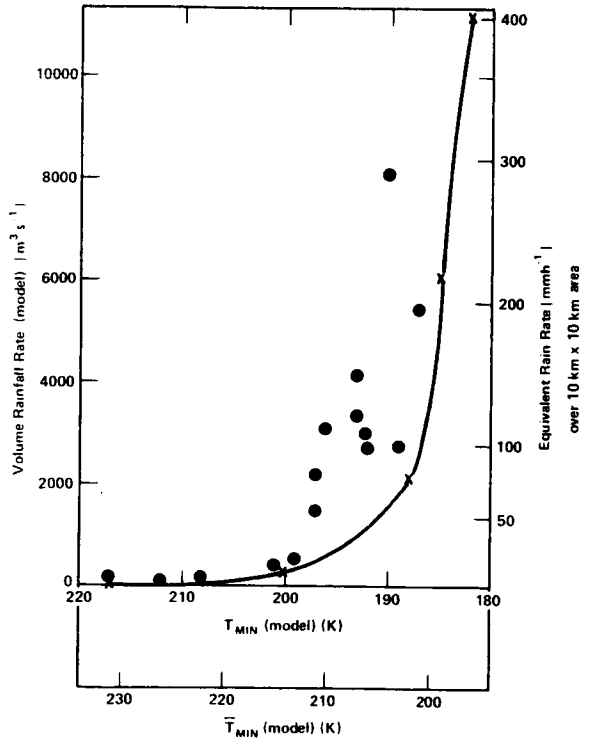


*Figure 9. Model volume rainfall rate (VRR) as a function of model $T_{min}$ with the data points plotted on the $\bar{T}_{min}$ scale.*

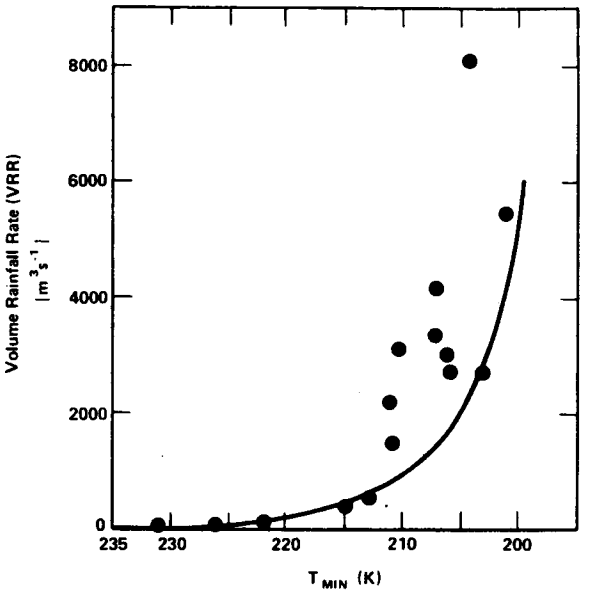


*Figure 10. Volume rainfall rate (VRR) calculated from Eq. (16) and using the model $\bar{w}_{max}/T_{min}$ relation to convert to $T_{min}$. Data points are same as in Figs. 6 and 9.*

A primary test of the use of the model results will be the testing of the relations under different climatological and synoptic conditions. One such test will be with radar results of maximum echo height (convertible to $T_{min}$) versus rainfall by Konrad (1977), Wilk (1981) and Gagin and Lopez (personal communication) for various climatological regimes. Analysis by one of the authors (Atlas) already indicates significant climatological differences.

## 4. SUMMARY AND CONCLUSIONS

The production of precipitation in thunderstorms is a complex combination of cloud dynamics and microphysics and the interaction of the storm with its environment. However, in section 2 the simple steady state condensation rate equation is used to derive some formulations relating to volume rainfall rate (VRR) to satellite observables indicative only of relative updraft intensity. These relations reproduce the case study results of Negri and Adler (1981) to a first approximation. They emphasize that the VRR is roughly proportional to the area-average vertical velocity or mass flux (assuming the moisture source is constant). A satellite-based estimate of vertical mass flux in a thunderstorm, coupled with knowledge of the low-level moisture source (from surface conventional data) may be combined into an estimate of the total condensation rate--an upper bound for the VRR. The parameter $T_{min}$ can be used as a proxy for the vertical mass flux through an empirical relation. Thus, we have a physically-based relation between $T_{min}$ and storm rainfall.

Analysis of one-dimensional model results also indicates that model-based VRR is linearly related to the vertical mass flux. An important model result is that the model-generated relation between w and $T_{min}$ is similar to the empirical (satellite-based) relation and gives support to the idea of using the model results to establish $T_{min}$/mass flux relations for various climatic or synoptic conditions, thus making the approach transportable. The idea of using the one-dimensional model to aid in interpreting the satellite observations appears plausible, but needs a deeper examination with reference to more sophisticated (three-dimensional) models and additional data sets.

The authors have been pleased with the generally positive results presented in this paper. However, they are acutely aware that the simple relations tested here against one data set must be evaluated against additional sets for confirmation. Analysis of past radar data sets points out differences in rainfall/maximum height relations depending on climatological or, possibly, storm type variables. These will have to be taken into account for a successful result.

Because of the complexity of the rainfall process, it is unlikely that the approach presented in this paper will result in a deterministic satellite/rainfall relation. However, the approach may produce a basis for statistical relations for each climatological regime or storm type.

REFERENCES


Adler, R. F. and D. D. Fenn, 1979: Thunderstorm vertical velocities estimated from satellite data. J. Atmos. Sci., 36, 1747-1754.

Adler, R. F., D. D. Fenn, and W. S. Shenk, 1981: Thunderstorm top structure observed by aircraft overflights with an infrared radiometer. SESAME 1979 Preliminary Results Workshop, Huntsville, AL, 60-62.

Auer, A. H. and J. D. Marwitz, 1968: Estimates of air and moisture flux into hailstorms on the high plains. J. Appl. Met., 7, 196-198.

Austin, P. M. and R. A. Houze, Jr., 1973: A technique for computing vertical transports by precipitating cumuli. J. Atmos. Sci., 30, 1100-1111.

Brown, J. M. and J. B. Klemp, 1980: Water budgets of numerically simulated cumulonimbus clouds. Eighth Conference on Weather Forecasting and Analysis, 212-219.

Foote, G. G. and J. C. Fankhauser, 1978: Airflow and moisture budget beneath a northeast Colorado hailstorm. J. Appl. Met., 12, 1330-1353.

Griffith, C. G., W. L. Woodley, P. G. Grube, D. W. Martin, J. Stout, and D. N. Sikdar, 1978: Rain estimation from geosynchronous satellite imagery-visible and infrared studies. Mon. Wea. Rev., 196, 1153-1171.

Griffith, C. G., J. A. Augustine, and W. L. Woodley, 1981: Satellite rain estimation in the U.S. High Plains. J. Appl. Met., 20, 53-66.

Konrad, T. G., 1977: Statistical models of summer rain showers derived from fine-scale radar observations. Report No. APL/JHU CP 056, Johns Hopkins University, 67 pp.

Mack, R. A. and D. P. Wylie, 1981: An estimation of the condensation rates in three severe storm systems from satellite observations of the convective mass flux. Submitted to Mon. Wea. Rev.

Marwitz, J. D., 1972: Precipitation efficiency of thunderstorms on the High Plains. Preprints 3rd Conference on Weather Modification, Rapid City, SD, Amer. Meteor. Soc., 245-247.

Negri, A. J. and R. F. Adler, 1981: Relation of satellite-based thunderstorm intensity to radar-estimated rainfall. J. Appl. Met., 20, 288-300.

Park, S. and D. N. Sikdar, 1980: An application of a simple diagnostic cloud model to the May 20, 1977, storms over the Oklahoma mesonetwork, Tellus, vol. 32, 326-339.

Scofield, R. A. and V. J. Oliver, 1977: A scheme for estimating convective rainfall from satellite imagery. NOAA Technical Memorandum NESS 86, 47 pp.

Simpson, J. and V. Wiggert, 1969: Model of precipitation cumulus towers. Mon. Wea. Rev., 97, 471-489.

Stout, J. E., D. W. Martin, and D. N. Sikdar, 1979: Estimating GATE rainfall with geosynchronous satellite images. Mon. Wea. Rev., 107, 595-598.

Turner, J. S., 1962: The starting plume in neutral surroundings. J. Fluid Mech., 13, 356-367.

Wilk, K. E., 1981: FAA radars and their display of severe weather (thunderstorms). Report No. FAA-RD-80-65 (in press).

Reprinted from JOURNAL OF APPLIED METEOROLOGY, Vol. 20, No. 11, November 1981
American Meteorological Society
Printed in U. S. A.



# Satellite-Observed Cloud-Top Height Changes in Tornadic Thunderstorms

ROBERT F. ADLER

*Laboratory for Atmospheric Sciences, National Aeronautics and Space Administration, Goddard Space Flight Center, Greenbelt, MD 20771*

DOUGLAS D. FENN[1]

*GE/MATSCO, Beltsville, MD 20705*

11 August 1980 and 1 August 1981

ABSTRACT

Short-interval geosynchronous infrared satellite data are used to examine 11 cases of tornadic thunderstorms with respect to cloud-top temperature (height) variations relative to tornado touchdown times, and in three cases relative to the initial observation of mesocyclones by Doppler radar. The scale of the updrafts observable with the satellite infrared data is ~10 km. The cases are limited to those with relatively intense tornadoes. In 8 of the 11 cases there is a period of rapid cloud-top ascent 30–45 min prior to tornado touchdown. This upward growth appears to be associated with the formation of the mesocyclone. This ascent is followed by a period of no growth or even a drop in cloud-top height preceding, or at the time of, tornado touchdown. In the three remaining cases cloud-top ascent is evident in the satellite data at tornado touchdown.

## 1. Introduction

The study of thunderstorm top height changes near the time of tornadoes is important in order to help understand the relation of cloud dynamics to mesocyclogenesis and tornado touchdown. Also, since the storm top is the only portion of the cloud observable with satellite data, it is important to determine what tornado-related characteristics can be inferred from current satellite observations.

Radar observations (e.g., Lemon *et al.*, 1978) indicate that tornado touchdown is often accompanied by a decrease in echo maximum height and a decrease in the height of the Bounded Weak Echo Region (BWER). Both decreases are indicative of a weakening of the updraft. Fujita (1973)[2] proposed that the collapse of overshooting thunderstorm tops is associated with tornado generation and touchdown. Purdom (1971)[3] showed examples of a pause in the rate of anvil expansion (measured from satellite image data) at the times of tornado touchdown. More recently, five tornado bearing clouds on 6 May 1975 were discussed by Adler and Fenn (1979a). An examination of the five clouds elements, having eight tornadoes clearly associated with them, indicated that in seven of the eight cases the first report of the tornado took place during, or just after, a rapid expansion of cloud-top areas defined by equivalent blackbody temperature ($T_{BB}$) isotherms. This rapid expansion of areas within isotherms implies ascent on a scale of ~30 km, even larger than the scale of an individual infrared (IR) data point (10 km).

In this paper, eleven tornadic storms, including five cases from Adler and Fenn (1979a), are evaluated with respect to cloud top temperature changes relative to tornado touchdown, and in three cases relative to initial reports of Doppler radar observed mesocyclones.

## 2. Analysis of 11 tornadic thunderstorms

Digital image data from SMS/GOES geosynchronous satellites were analyzed on four case study days (see Table 1) with the aid of an interactive computer/image analysis system called AOIPS (Atmospheric and Oceanographic Information Processing System). Data were from times when the satellite was operated in the short-interval mode, images produced every 3–7.5 min over a swath of limited north–south extent. This high time resolution is necessary to observe rapidly changing convective storms. The digital infrared (IR) data which are the basis of this study have a spatial resolution of ~10 km (depending on location relative to the subsatellite point) and an effective temperature resolution of 1–2 K.

The set of tornadic thunderstorms was limited, for this study, to storms with relatively strong tornadoes. All but one of the storms had tornadoes of intensity F2, or greater [on an intensity scale of F0 through F5 as described by Fujita (1973)]. Kelley

[1] Present affiliation: Office of Hydrology, National Weather Service, Silver Spring, MD 20010.

[2] Fujita, T. T., 1973: Proposed mechanism of tornado formation from rotating thunderstorms. *Preprints 8th Conf. Severe Local Storms*, Denver, Amer. Meteor. Soc., 191–196.

[3] Purdom, J. F. W., 1971: Satellite imagery and severe weather warnings. *Preprints 7th Conf. Severe Local Storms*, Kansas City, Amer. Meteor. Soc., 120–137.

0021-8952/81/111369-07$05.75

TABLE 1. Tornadic thunderstorm case study days.

| Date | Area | Spacecraft |
|---|---|---|
| 6 May 1975 | Nebraska | SMS-2 |
| 24 April 1975 | Missouri | SMS-2 |
| 20 March 1976 | Illinois | GOES-1 |
| 20 May 1977 | Oklahoma | GOES-1 |

*et al.* (1978) have shown from climatology that while only 38% of tornadoes are F2 or above, they account for 98% of tornado fatalities. In a few cases where more than one tornado was produced from a storm, only the data relative to the time of the most intense tornado was examined. One storm with only an F1 tornado was included in the sample because of its long tornado path. This procedure was designed to concentrate the analysis on so-called "supercell" storms (Browning and Foote, 1976), which are the main producers of relatively strong tornadoes (Lemon and Doswell, 1979). It also eliminates the relatively weak tornadoes, for which the time of occurrence is often suspect.

The results of the 11 storms are shown in Fig. 1. If there is more than one tornado associated with a cloud, only the most intense tornado is considered. Such is the case in Figs. 1a, 1c, 1d and 1f.

Fig. 1 depicts the variation with time of the satellite-observed minimum $T_{BB}$ for each storm relative to the time of the associated tornado. Decreases in $T_{BB}$ imply cloud-top ascent and increases in $T_{BB}$ imply descent. Because of the relatively coarse spatial and temperature resolution in the IR data, small or temporary changes in $T_{BB}$ or in the slope of the $T_{BB}$ curve should be considered suspect and may be artifacts of the data. For example, in Fig. 1i there is a brief stairstep at −40 min, which is probably a data artifact due to the coarse temperature resolution. These stairsteps are common in the data set and usually do not represent pauses in the ascent (or descent), as

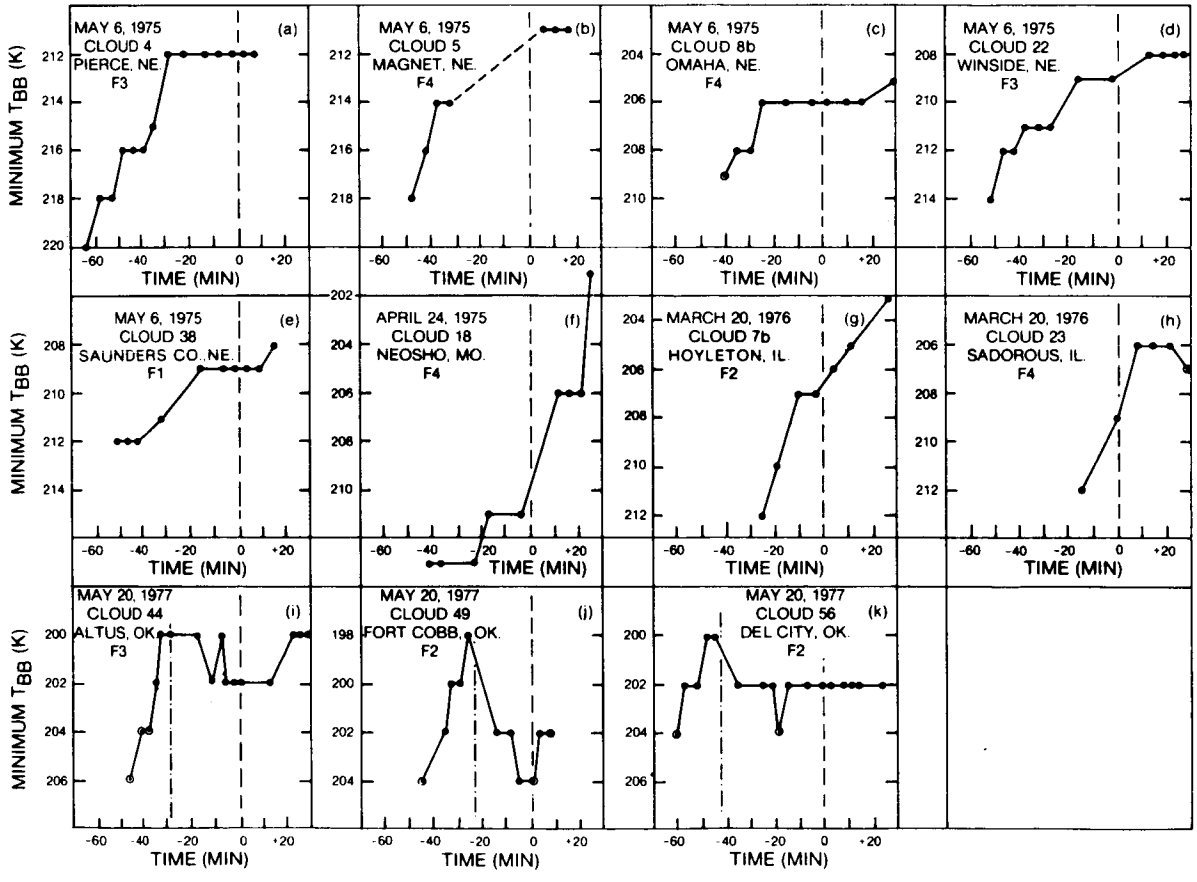


FIG. 1. Minimum cloud-top temperature ($T_{BB}$) as a function of time relative to the time of tornado touchdown in 11 cases of relatively strong tornadoes. The circled dots indicate the cases of the lowest temperature not being associated with a closed $T_{BB}$ isotherm. The time of the tornado touchdown is noted by the vertical dashed line at the time equal to zero. In three cases ($i, j, k$) the initial times of mesocyclones observed by Doppler radar of the National Severe Storms Laboratory in Norman, Oklahoma are shown by the vertical dash-dot lines.

can be seen by the continued expansion of the number of data points within the minimum $T_{BB}$ isotherm during a period of constant minimum $T_{BB}$. The relation of $T_{BB}$ isotherm expansion near cloud-top center to vertical velocity and divergence has been discussed by Adler and Fenn (1979a).

Another problem is related to the coarse spatial resolution (~10 km) and the position of the satellite IFOV relative to the cloud top. A thunderstorm top will produce a slightly lower observed $T_{BB}$ if the top is centered in an IFOV instead of being split between two adjacent views. Successive satellite views of a constant height storm may occasionally show an observed change in $T_{BB}$, implying a false height change. An example of this may be the oscillation in panel *i* at −10 min.

In general, because of these data problems, small or short-lived changes in $T_{BB}$ or its slope should be ignored. Changes of 3 K (4 K for the 20 May 1977 storms) can be considered significant, along with smaller variations if they are supported by more than one data point at each end of the change.

Eight of the 11 storms (Figs. 1a, 1b, 1c, 1d, 1e, 1i, 1j and 1k) had an associated rapid decrease of cloud top $T_{BB}$ (as observed from satellite) ~30–45 min before tornado touchdown. This implies a rapid upward movement of the cloud top. These storms also had their period of most rapid area expansion within $T_{BB}$ isotherms prior to the touchdown. On most of these eight storms the rapid decrease in temperature was followed by a reduction in the slope of the temperature-time profile, and in the 20 May cases (Figs. 1i, 1j and 1k) a warming, indicating a cessation in upward growth or a slight drop in maximum cloud height. The Fort Cobb case (Fig. 1g) exhibits a substantial 6 K warming or cloud-top collapse.

The sequence of events at the cloud top can be pictured as being associated with storm evolution in the following way. A period of rapid upward growth at cloud top is associated with or possibly precedes the formation of the mesocyclone at mid-levels in the storm. Tornado touchdown is usually associated with a decreasing or near constant maximum cloud top. This sequence of events at cloud top is consistent with radar studies (e.g., Lemon *et al.*, 1978) and with hypotheses proposed by Fujita (1973)[2] which were based on aircraft observations.

Three storms (Figs. 1f, 1g and 1h) showed decreasing cloud top $T_{BB}$ (increasing height) at the time of the tornado touchdown. The tornadoes from all three of these storms were intense with Fujita/Pearson scale ratings (Fujita, 1973) of F4, F2 and F4 for the storms in Figs. 1f, 1g and 1h, respectively.

The Neosho, Missouri storm (Fig. 1) is the most obvious exception to the other eight storms. While the tornado was on the ground, the cloud-top minimum temperature dropped nearly 10 K [over an area of ~100 km$^2$, one instantaneous field-of-view (IFOV)], indicating strong ascent. It is possible that the strong growth was associated with a new cell, adjacent to the tornadic cell, but this does not seem to be the case from the satellite analysis and examination of available radar data. The cloud top ascended during the first 25 min of the tornado until the time the short-interval data ended.

The Hoyleton, Illinois tornado (Fig. 1g) of 20 March 1976 also was on the ground while the satellite-viewed cloud top was ascending. However, the Hoyleton storm did show rapidly increasing height from 40 to 10 min before tornado touchdown, until a brief height plateau was reached at 207 K, just before tornado touchdown. During that constant temperature period, the area within the 207 K $T_{BB}$ isotherm decreased from 200 to 100 km$^2$, which is equivalent to a change from two IFOV's to one IFOV. This area decrease at constant temperature implies cloud top collapse, or at least constant height. This sequence is similar to an occurrance noted with the Omaha tornado on 6 May 1975 (Fig. 8, Adler and Fenn, 1979a). However, in the Hoyleton case, the storm resumed its upward climb, and continued to ascend during the lifetime of the tornado.

Fig. 1h shows the Sadorous storm with rapid ascent during tornado touchdown, followed by a period of constant height and then descent. The largest area within the 206 K isotherm occurred at the first observation, and then decreased, indicating that maximum storm height happened just after tornado touchdown. Fujita *et al.* (1976) have analyzed this storm and indicate that the tornado reached F4 intensity ~20 min after touchdown. Perhaps, in this case, the cloud-height decrease was associated with the intensification of the tornado vortex and not touchdown itself.

Therefore, a majority of the storms analyzed had rapid ascent of cloud tops 30–45 min before tornado touchdown, persumably during formation of the mesocyclone (documented in three cases). A minority of the storms, however, had ascending cloud tops (at the scale of the satellite observation) at the time of tornado touchdown.

The indicated characteristic cloud-top evolution of the majority of tornadic storms means that we have a first link between satellite observations and tornadic activity. It does not mean, however, that we now have a way to discriminate between tornadic and non-tornadic thunderstorms with satellite data. Intense, non-tornadic storms examined also have a period of rapid growth above the tropopause, followed by relatively steady heights.

The magnitude of the vertical velocities are reasonable when the horizontal scale (10 km) on which they are applicable is considered. A typical rate of temperature ($T_{BB}$) decrease in Fig. 1 is 0.4 K min$^{-1}$. Using an appropriate lapse rate, the temperature

change rate can be converted to an equivalent vertical velocity or cloud-top ascent rate. Hasler and Adler (1980)[4] have compared satellite observed height (from satellite stereo analysis) and IR temperatures for thunderstorm tops. For overshooting tops (above the tropopause) they find a temperature-height relation of 2.5 K km$^{-1}$, which was approximately midway between ambient and adiabatic for the particular case. However, the horizontal scale of the two observations are different, with 10 km for the IR temperature and 1–3 km for the stereo-determined height, depending on the size and definition of the feature in the visible data. If the two measurements were made at the same scale, the calculated lapse rate would shift toward adiabatic. Therefore, using the 2.5 K km$^{-1}$ lapse rate in Eq. (1)

$$w = -\left(-\frac{\partial T}{\partial z}\right)^{-1} \frac{dT_{BB}}{dt} \tag{1}$$

produces a vertical velocity $w$ appropriate on a horizontal scale of 1–3 km, roughly equivalent to radar resolution at thunderstorm top. Using a 2.5 K km$^{-1}$ value for the lapse rate gives an equivalent vertical velocity of 2.7 m s$^{-1}$. This is nearly equal in magnitude to the echo top rise rate above the tropopause indicated for the Union City Storm (Burgess and Lemon, 1976[5], Fig. 5.6; Lemon *et al.*, 1978, Fig. 13). However, larger cloud top ascent rates (up to 8 m s$^{-1}$) have been calculated from satellite IR data for intense convection penetrating through the upper troposphere (Adler and Fenn, 1979b).

In Fig. 1 only panels 1i, 1j and 1k show a $T_{BB}$ increase (indicating descent or cloud top collapse) prior to, or at the time of, tornado touchdown. The 6 May cases (Figs. 1a–1c) show a constant temperature with time at the time of the tornado. This difference (between the two days) may be related to the difference in larger scale cloud structure between the two cases and the satellite sensor's response characteristics. The 6 May storms appeared in the satellite images as a narrow line lying along a generally north–south oriented cold front. The east–west extent of the storm's anvils increased with time. As the satellite IR sensor scans from left to right across the scene it moves abruptly from a warm target (ground) to a cold target (thunderstorm top). With a narrow cirrus shield, the sensor may not have enough time to accurately respond to the minimum $T_{BB}$, especially since it is often located near the left, or upwind side of the anvil. That is, for narrow (in the left-to-right direction) cirrus anvils, the minimum $T_{BB}$ is probably overestimated (i.e., estimated to be warmer than it is). However, as the originally narrow anvil expands with time, the amplitude of the temperature overestimation should decrease as the distance from the left anvil edge to the storm center increases. If, while the anvil is expanding, the actual minimum $T_{BB}$ is warming slightly, this could be obscured by the varying overestimation effect, with the result being a near-constant observed $T_{BB}$ with time. For example, cloud 4 in Fig. 1a has a 35 min period of constant $T_{BB}$ (212 K) while the anvil is expanding. The distance from the left anvil edge (denoted by the 226 K isotherm) to the center of the area of coldest $T_{BB}$ increases from two data points to nine data points over the 35 min time period. Work on a technique to remove this sensor response effect is planned.

On 20 May 1977, the storms (Figs. 1i, 1j and 1k) were imbedded in a very large cirrus shield with a large distance between the left edge and the storms' centers. Thus, the sensor response problem in terms of estimating the minimum $T_{BB}$ should not exist. In these cases, a warming was observed.

## 3. 20 May 1977 storms

The three intense tornadic storms observed on 20 May 1977 are the best analyzed storms to this date with respect to Doppler radar coverage. A complete analysis of the cases with satellite, Doppler radar reflectivities and velocities, and other data is underway by the authors and others. Preliminary results based primarily on satellite data will be discussed in this section.

### *a. Altus storm*

The Altus, Oklahoma storm was actually a combination of two related thunderstorms which could be identified in both the satellite and radar data. The National Severe Storms Laboratory (NSSL) Doppler radar log indicated only one mesocyclone, but an examination of the positions of the mesocyclone, reflectivity maxima and satellite features showed that two mesocyclones, associated with two storms, were involved. The temperature-height versus time diagram for both cells is shown in Fig. 2. Cloud 37 (the numbering system is from a larger study) was first defined as penetrating the cirrus shield just after 1840 GMT (1140 CST) at 207 K. The background cirrus $T_{BB}$ was 209 K, approximately equal to the tropopause temperature. With dense cirrus shields already existing, such as in this case, the new thunderstorms cannot be detected in the satellite IR data until they significantly penetrate the cloud deck at very cold temperatures.

Cloud 37 peaked at 198 K and remained well defined at 200 K as it traveled north-northeastward. A mesocyclone was first noted at 1932 GMT in the

[4] Hasler, A. F., and R. F. Adler, 1980: Cloud-top structure of a tornadic thunderstorm from 3 min interval stereo satellite images compared with radar and other observations. *Preprints 19th Conf. Radar Meteorology*, Miami, Amer. Meteor. Soc., 405–412.

[5] Burgess, D. W., and L. R. Lemon, 1976: Union City Storm history, the Union City, Oklahoma tornado of 24 May 1973, R. A. Brown, Ed. NOAA Tech. Memo ERL NSSL-80, 35-51.

Doppler radar observation log, colocated with the satellite feature. The radar-observed circulation, marked as M37 in Fig. 2, perhaps existed earlier, but was not detected because of the relatively long distance (220 km) from the radar to the storm. This mesocyclone remained relatively weak, and was dissipating at the 1952 GMT observation.

At about 1940 (all times GMT unless indicated otherwise), evidence of a second storm (Cloud 44) was observed in the satellite data approximately 30 km to the southeast of cloud 37 and colocated with a second radar reflectivity maximum. Cloud 44 ascended rapidly to 200 K (~4 km above the tropopause) by 1950. An associated mesocyclone was first observed at 1952 by the Doppler radar. Thus, the initiation of the cyclonic rotation appears associated with rapid cloud top ascent and, therefore, a strong updraft. After a relatively stable 15 min period the cloud top temperature oscillated and then warmed. The oscillation around 2010 may not reflect an actual cloud height fluctuation, but an effect of sensor resolution and the location of the satellite data point relative the highest part of the cloud top. However, between 2005 and 2020 there was a slight storm top decrease, just preceding the reported tornado touchdown. The storm top ascended again just after tornado dissipation, a feature also seen in the following two cases.

*b. Fort Cobb storm*

The Fort Cobb, Oklahoma storm developed to the southeast of the Altus storm and also had two associated cold features in the satellite IR data. One of the features, identified as cloud 49, was first defined at 2045 and reached a temperature of 202 K, then weakened and became difficult to define in the IR field until 2210. At that time (see Fig. 3), the time sequence of IR images showed a sharp cloud top ascent from 204 to 198 K in 18 min. A mesocyclone (mesocyclone A) was initially observed at the time of maximum height. The next observation of the storm was 12 min later and the storm top has warmed 4 K, or ~2 km, based on a lapse rate halfway between ambient and adiabatic. After 2240 the cold feature in the IR data became more difficult to follow and may have been just a piece of outflow debris. The times of the associated tornadoes are shown in Fig. 3 based on analysis presented by Johnson *et al.* (1980).[6] The touchdown of the Fort Cobb tornado occurred at the end of a period of sharp decrease in the satellite-observed height with a temperature change from 198 to 204 K.

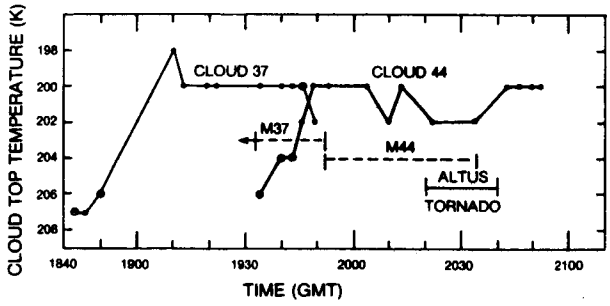


FIG. 2. Minimum cloud top temperature as a function of time for cloud elements associated with the Altus, Oklahoma tornado of 20 May 1977.

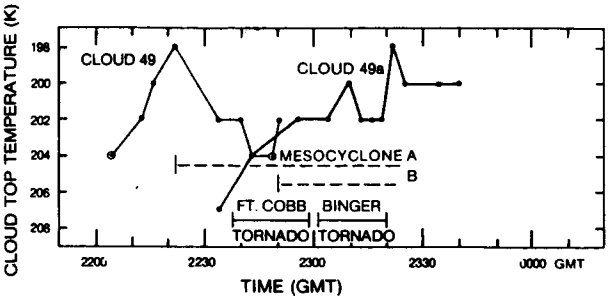


FIG. 3. Minimum cloud top temperature as a function of time for cloud elements associated with Fort Cobb, Oklahoma storm of 20 May 1977.

As the first IR feature (cloud 49) became indistinct and disassociated from the main radar echo (and mesocyclone A) at approximately 2230, another $T_{BB}$ minimum (cloud 49a) was defined 30–40 km to the southwest of the mesocyclone position. This new feature in the IR field had an associated radar reflectivity maximum. Between 2230 and 2300, the satellite data indicated cloud-top ascent as this new updraft center (as defined in the $T_{BB}$ field) raced toward the northeast at 30 m $s^{-1}$, finally catching up to the location of the original reflectivity maximum at approximately 2250. The new IR feature, labeled 49a, became dominant and was located near both mesocyclones (which are approximately 8 km apart), although it was probably related to the updraft associated with mesocyclone B. A detailed study of the complex evolution of radar and satellite-observed features during this period is underway.

The top of cloud 49a continued to ascent until 2310. The apparent flattening of the curve between 2255 and 2305 is an artifact of the poor vertical (temperature) resolution (2 K) in the satellite data. Although the minimum temperature remained constant at 202 K the number of IR data points at that temperature increased from two to ten, indicating continued ascent. The second tornado, associated with mesocyclone B and an updraft along the gust front (Ray *et al.*, 1981), touched down during this period of apparent cloud-top ascent. Again, as in the Altus case, the cloud top rose after tornado dissipation.

[6] Johnson, B. C., K. W. Johnson, P. S. Ray, J. S. Bradberry, J. J. Stephens and W. C. Bumgarner, 1980: The morphology of some tornadic storms. *Preprints 19th Conf. Radar Meteorology*, Miami, Amer. Meteor. Soc., 311–316.

*c. Del City storm*

The Del City storm also involved two thunderstorms, identified in the satellite data as clouds 53 and 56 (see Fig. 4). Cloud 53, which had a period of rapid growth at 2240 to a minimum temperature of 200 K is referred to as the "hailstorm" in the study by Ray *et al.* (1981). As cloud 53 collapsed another storm (cloud 56) appeared to the south, grew, moved northward, and caught up and merged with the hailstorm. Cloud 56, the main feature, reached a temporary height maximum at 202 K at 2305–2325, then descended slightly to 204 K. A new surge in the updraft was noted between 2335 and 2355 as the storm top reached 200 K. This period of cloud top ascent was coincident with the formation of the mesocyclone.

The cloud-top temperature fell back to 202 K, then remained nearly constant for one hour as the storm moved in a northeast direction. Although this period was marked by constant temperature, the position of the cold feature was twice redefined slightly southeastward in a non-continuous manner. This redefinition is probably related to the effect of the IR cold area beginning to represent debris from the updraft and moving off from the storm core and radar echo until a new surge in the vertical velocity reestablishes the IR cold point over the updraft itself.

No cloud-top collapse was noted in association with tornado touchdown in this case. Although there is a 30 min absence of data centered at 0015 GMT, there is evidence supporting cloud top rise after tornado dissipation. This was also evident in the Altus and Fort Cobb cases, and may represent reintensification of the storm through a new updraft on the storm flank, or revitalization of the original updraft.

## 4. Mechanisms for rotation generation and intensification

The mechanisms by which certain thunderstorms produce the initial storm-scale rotation, or mesocyclone, and the mechanisms by which this rotation is concentrated to produce a tornado are not completely understood. However, recent research using observations from Doppler radars (e.g., Heymsfield, 1978) and results of three-dimensional numerical models (e.g., Schlesinger, 1980) have indicated that the two dominant terms in the vorticity equation related to vorticity changes following a fluid parcel are the concentration or stretching term, and the tilting term, shown in Eq. (2) as the two terms to the right side of the equal sign:

$$\frac{d\zeta}{dt} = -\zeta(\nabla_H \cdot \mathbf{V}) + \left(\frac{\partial w}{\partial y}\frac{\partial u}{\partial z} - \frac{\partial w}{\partial x}\frac{\partial v}{\partial z}\right). \quad (2)$$

The vertical component of relative vorticity is given by $\zeta$, while $u$, $v$ and $w$ are the components of the vector velocity V. This formulation neglects the solenoidal term, the frictional torque term, and terms involving the earth's vorticity. Although the stretching and tilting terms are the most important, Lemon and Doswell (1979) suggest that the solenoidal term may also be a significant, but secondary, contributor.

The satellite observations presented in this paper cannot, by themselves, answer the vorticity mechanism question, but do complement the studies based on radar observations and other data. A majority (8/11) of the satellite cases indicate that during the development of the mesocyclone the thunderstorm top is rapidly ascending, implying intensification of the storm updraft. This relation confirms radar case study observations (e.g., Lemon *et al.*, 1978) of echo top height increases during mesocyclonesis. Lemon and Doswell (1979), in developing a descriptive model of mesocyclone evolution, indicate that the Bounded Weak Echo Region (BWER), which implies updraft, is colocated with the mesocyclone in its early stages. If the vorticity center is indeed colocated with the updraft at this stage, the implication is that the vorticity increase associated with mesocyclone generation occurs through the vertical stretching of the air column in the rapidly intensifying updraft. However, the tilting term must also be important, at least along the updraft edges, where the gradient of vertical velocity is large. Although numerical model results (e.g., Schlesinger, 1980) in-

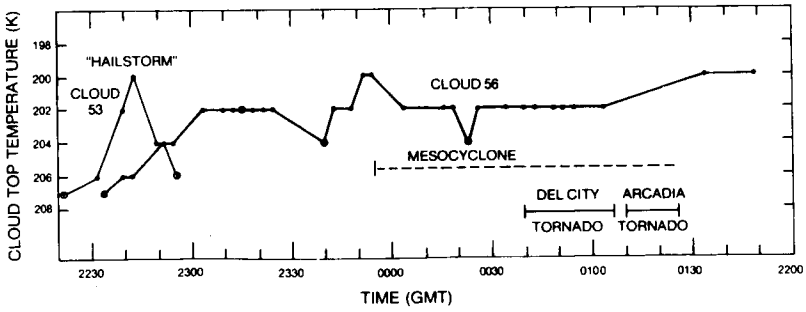


FIG. 4. Minimum cloud top temperature as a function of time for cloud elements associated with the Del City, Oklahoma storm of 20 May 1977.

dicate dominance by the tilting term in this early stage, this dominance is artificial because the models eliminate stretching at the earliest time by assuming no ambient vorticity (vertical component) in the initial flow field.

Tornado touchdown was associated (in a majority of cases) with satellite-observed constant or decreasing cloud top height. These observations are in agreement with radar echo-top information such as in the Union City tornado case (Lemon *et al.*, 1978). Lemon and Doswell (1979), synthesizing observations from a number of cases, conclude that the vortex intensification and tornadogenesis is associated with updraft weakening, downdraft formation upwind of the updraft and a shift of the vortex center from the updraft center to the updraft-downdraft boundary. This implies that the tilting term may be dominant at this stage, as weakly indicated by observations (Ray *et al.*, 1976; Lemon and Doswell, 1979), and strongly indicated in model results (Schlesinger, 1980). The satellite data merely emphasize that vortex intensification is apparently related to updraft weakening in most cases. Although this observation also fits the "vortex valve" concept of vortex-updraft interaction (Lemon, 1976,[7] Lemon *et al.*, 1978; Brandes, 1978), observations of the intense vortex being situated on an updraft-downdraft boundary (e.g., Brandes, 1978) appear to eliminate this theory.

The majority of storms depicted in Fig. 1, therefore, agree with previous observations of echo top behavior in tornadic storms and the conceptual model of Lemon and Doswell (1979). The three exceptions (Figs. 1f, 1g and 1h) may be just slight variations of the model (this is plausible with Figs. 1g and 1h), or may be radical departures (likely for Fig. 1f). The Neosho term (Fig. 1f) displays rapid cloud-top ascent during and following touchdown of a very intense tornado (F4). This may imply that the stretching term may still be very important at this stage, in this case.

## 5. Summary

Infrared geosynchronous satellite data have been analyzed to determine thunderstorm top height variations relative to the time of tornado touchdown. In eight of eleven cases of relatively strong tornadoes, there was a period of rapid height increase (temperature decrease) 30–45 min prior to tornado touchdown. A typical value for this temperature decrease above the tropopause is 0.4 K $min^{-1}$, which is equivalent to a cloud top ascent rate of ~3 m $s^{-1}$. In three cases where Doppler radar observations were available, this period of rapid cloud top ascent coincided with the development of the mesocyclone. In the same eight cases, the time of tornado touchdown was a period of nearly constant height, or slight height decrease (temperature increase). This sequence of satellite-observed events in the evolution of these tornadic thunderstorms is similar to radar-observed echo top changes noted in other tornadic thunderstorms and is consistent with a conceptual model (Lemon and Doswell, 1979) in which the mesocyclone vorticity is generated primarily through the stretching of the vertical air column in a rapidly intensifying updraft. The intensification and descent of the vortex to form a tornado is related to a weakening of the updraft, formation of a downdraft, and a shift of the vortex to the updraft-downdraft boundary, so that the tilting term becomes dominant in the generation of vorticity.

*Acknowledgment.* The authors thank the personnel at the National Severe Storms Laboratory for supplying the Doppler radar log and radar data used in this study. Douglas A. Moore, Raymond Wexler, and other colleagues provided numerous insights into the 20 May 1977 case.

[7] Lemon, L. R., 1976: Tornadic storm evolution: Vortex value hypothesis. Appendix G, the Union City, Oklahoma Tornado of 24 May 1973, R. A. Brown, Ed. NOAA Tech. Memo. ERL NSSL-80, 229–234.

## REFERENCES

Adler, R. F., and D. D. Fenn, 1979a: Thunderstorm intensity as determined from satellite data. *J. Appl. Meteor.*, **18**, 502–517.

——, and ——, 1979b: Thunderstorm vertical velocities estimated from satellite data. *J. Atmos. Sci.*, **36**, 1747–1754.

Brandes, E. A., 1978: Mesocyclone evolution and tornadogenesis: Some observations. *Mon. Wea. Rev.*, **106**, 995–1011.

Browning, K. A., and G. B. Foote, 1976: Airflow and hail growth in supercell storms and some implications for hail suppression. *Quart. J. Roy. Meteor. Soc.*, **102**, 499–534.

Fujita, T. T., 1973: Tornadoes around the world. *Weatherwise*, **26**, 56–62, 78–83.

——, G. S. Forbes and T. A. Umenhofer, 1976: Close-up view of March 20, 1976 tornadoes: Sinking cloud tops to suction vortices. *Weatherwise*, **29**, 116–131.

Heymsfield, G. M., 1978: Kinematic and dynamic aspects of the Harrah tornadic storm analyzed from dual-Doppler radar data. *Mon. Wea. Rev.*, **106**, 233–254.

Kelly, D. L., J. T. Schaefer, R. P. McNulty and C. A. Doswell III, 1978: An augmented tornado climatology. *Mon. Wea. Rev.*, **106**, 1172–1183.

Lemon, L. R., and C. A. Doswell III, 1979: Severe thunderstorm evolution and mesocyclone structure as related to tornadogenesis. *Mon. Wea. Rev.*, **107**, 1184–1197.

——, D. W. Burgess and R. A. Brown, 1978: Tornadic storm airflow and morphology derived from single-Doppler radar measurements. *Mon. Wea. Rev.*, **106**, 48–61.

Ray, P. S., C. E. Hane, R. P. Davies-Jones and R. L. Alberty, 1976: Tornado-parent storm relationship deduced from a dual-Doppler radar analysis. *Geophys. Res. Lett.*, **3**, 721–723.

——, B. C. Johnson, K. W. Johnson, J. S. Bradberry, J. J. Stephens, K. K. Wagner, R. B. Wilhelmson and J. B. Klemp, 1981: The morphology of several tornadic storms on 20 May 1977. *J. Atmos. Sci.*, **38**, 1643–1663.

Schlesinger, R. E., 1980: A three-dimensional numerical model of an isolated thunderstorm. Part II: Dynamics of updraft splitting and mesovortex couplet evolution. *J. Atmos. Sci.*, **37**, 395–420.

Reprinted from Preprint Volume: 12th Conference on Severe Local Storms, Jan. 11-15, 1982; San Antonio, Tex. Published by the American Meteorological Society, Boston, Mass.

4.16

# SATELLITE INFRARED, STEREO AND RADAR OBSERVATIONS OF TORNADIC THUNDERSTORMS ON APRIL 10, 1979

Andrew J. Negri
Laboratory for Atmospheric Sciences (GLAS)
Goddard Space Flight Center
National Aeronautics and Space Administration
Greenbelt, MD 20771

and

Robert Mack
GE/MATSCO
Beltsville, MD 20705

## OBJECTIVES

Investigate the cloud top height structure of the Wichita Falls tornadic storm of April 10, 1979 (and other tornadic storms on this day) from 0.5 micron observations from two satellites (stereography).

Identify individual convective elements in the 10 km resolution, 3 min interval infrared data and monitor the temporal change in minimum cloud-top temperature (CTT), with particular regard to time of tornado genesis and echo area expansion.

Investigate the limitations imposed by infrared field of view in defining individual thunderstorms in GOES digital imagery.

Compare stereographically determined cloud-top heights with simultaneous infrared observations and low-level reflectivity data to better understand the dynamics of storm development.

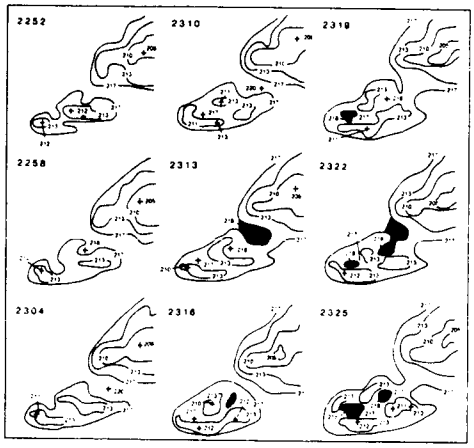


*Figure 1. Cloud-top temperature (CTT) analyses (K) of storms on April 10, 1979, 2252-2325 GMT. Areas of local temperature maxima and minima are identified by crosses, while interior temperature maxima (warm regions) are shaded. Analysis of individual thunderstorms often requires 3 min interval data and full radiometric resolution (1K). The CTT minima associated with the Wichita Falls, Pilot Point and Harrold tornadoes are respectively, the points 212K, 212K, and 206K, aligned southwest to northeast in the 2252 GMT panel.*

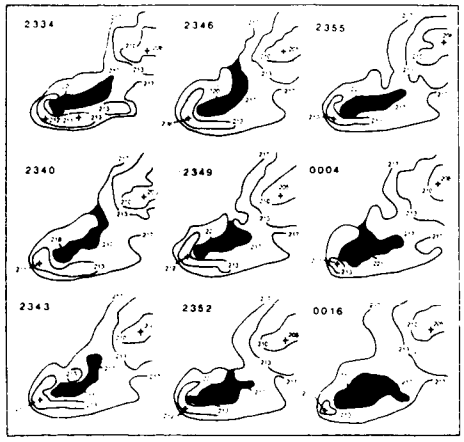


*Figure 2. Same analysis as Figure 1 except 2334-0016 GMT 10-11 April 1979. A pronounced region of warmer temperature (217-221K) has formed downwind of a region of colder (208-213K) "V" shaped region. The minimum temperature of this region is the storm top associated with the Seymour-Wichita Falls tornado. Possible explanations for this warm region are:*

*a) an eddy produced by the obstruction of the environmental flow around the main updraft, entraining warmer cloud material from the anvil edge,*

*b) warming produced by subsidence of air in the lee of the ascending tower, and*

*c) ejection of cirrus particles by the overshooting top into the (warmer) stratosphere.*

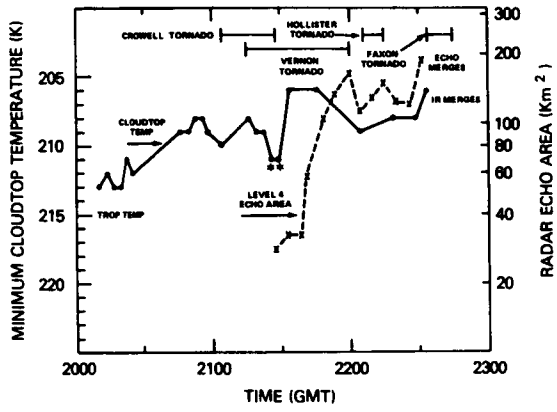


*Figure 3. Comparison of minimum CTT and radar reflectivity area for the Crowell-Lawton tornadic storm. Coincident with the appearance and expansion of the level 4 (45 dBz) echo area was a cooling of the minimum CTT from 211K to 206K in 3 min. The first reported tornado (at Crowell) was preceded by a slow cooling (4K/27min), followed by a 2K warming. After 2230 GMT, both the level 4 echo area and the minimum CTT became indistinguishable from similar areas of neighboring storms. Occasionally a temperature minima will dissappear into the broader temperature structure of the anvil. These points are denoted by an asterisk(*). Tropopause temperature from OKC at 2000 GMT is 215K.*

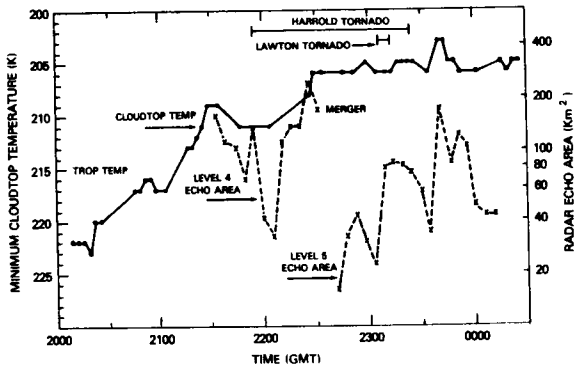


*Figure 4. Comparison of minimum CTT and radar reflectivity area for the Harrold-Grandfield storm. A significant cooling of the cloud-top (8K/27 min) was followed by a 2K warming just prior to tornado onset. This was followed by another period of cooling (5K/24 min) during which the level 4 (45 dBz) echo area increased by an order of magnitude and merged with another storm. Pulsations in the level 5 (55 dBz) echo area after 2230 GMT appear to be manifested at cloud top, with distinct episodes of cooling (1-3K) associated with each maximum in echo area. Small temperature changes at cloud top, when considered with respect to the large (100 km²) view of the IR sensor, may be indicative of substantial changes in storm volumetric rain rate as observed by radar. Minimum CTT for this storm was 203K, coincident with the largest areal extent of the level 5 echo at 2341 GMT.*

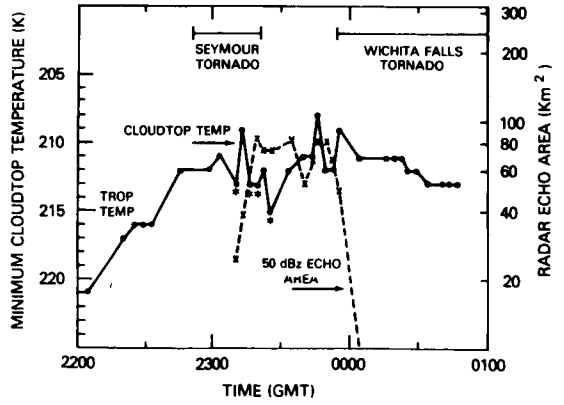


*Figure 5. Comparison of minimum CTT and radar reflectivity area for the Seymour-Wichita Falls tornadic storm. A cloud-top ascent (cooling) rate of 9K/46min followed by a warming of 2K/6 min preceded the onset of the Seymour tornado. A cooling of 7K/21 min followed by a 3K/3 min warming preceded the Wichita Falls tornado. The rapid fluctuation in minimum CTT between 2300 and 0000 GMT appears to be related to the IR field of view viewing a small feature on the extreme upwind anvil edge. This would lead to an overestimate (warming) of the minimum CTT. (See discussion of Figures 7-10.)*

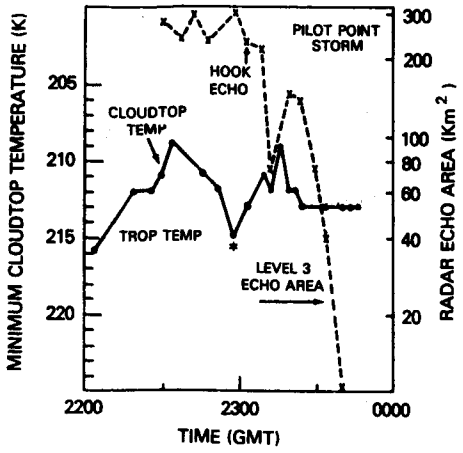


*Figure 6. Comparison of minimum CTT and radar reflectivity area for the Pilot Point tornadic storm. This storm underwent two periods of cooling and warming, one prior to, the other after, the identification of a hook echo in the low-level reflectivity. This was apparently a short-lived and weak tornadic storm.*

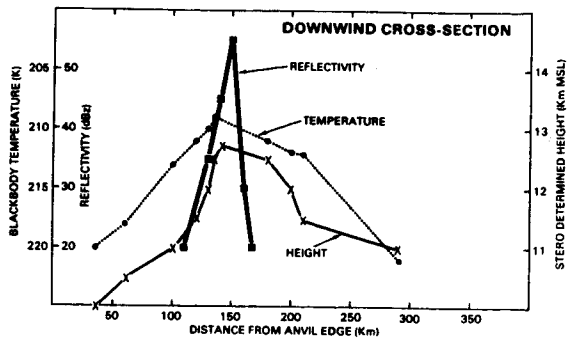


*Figure 8. Comparison of infrared derived temperature (K), stereo derived height (km) and low-level radar reflectivity for the cross-section D-D' in Figure 7 (2345 GMT). Distance scale starts at the northern anvil edge. These mature, downwind storms reveal a narrow, intense band of precipitation centered beneath a symmetric region of CTT/height. Nearly colocated peaks are 55 dBz, 209K, and 12.7 km.*

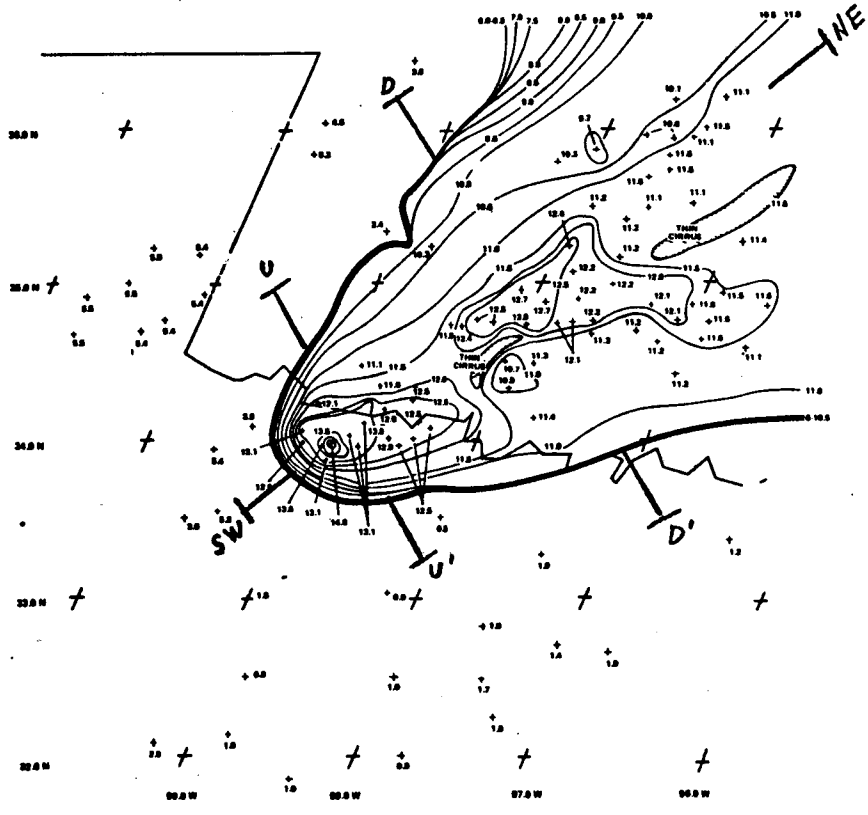


*Figure 7. Stereographically derived cloud-top heights, (km, MSL) from GOES East and West images at 2345 GMT on April 10, 1979. The satellites were inadvertently synchronized to within 4s. Highest top on the image was that associated with the Wichita Falls storm (14.6 km). Absolute accuracy of the heights is approximately 1 km, relative accuracy about 0.5 km. Cross-sections of height, temperature and low-level radar reflectivity are portrayed in Figure 8 (Downwind, D-D'), Figure 9 (Upwind, U-U') and Figure 10 (SW-NE section).*

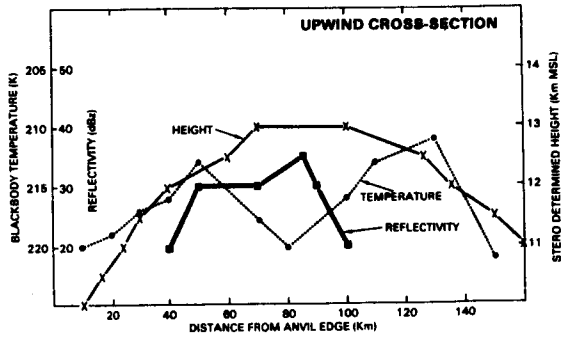


*Figure 9. Similar analysis as Figure 8 for the cross-section U-U' in Figure 7. Maximum reflectivity in this section was 35 dBz, located at the midpoint of a broad area of constant cloud-top height (13 km), but also located beneath the local warm area (220K) which formed in the lee of the "V-Notch." The data implies that above the tropopause (215K) no unique relationship exists between cloud-top height and temperature.*

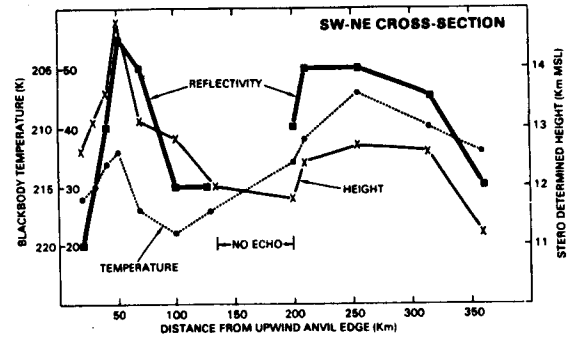


*Figure 10. Similar analysis as Figure 8 for the cross-section SW-NE in Figure 7. The Wichita Falls storm (50 km) showed excellent spatial agreement between maximum reflectivity (55 dBz), maximum height (14.8 km) and minimum CTT (212K), however, significant rain extends into the warm region (219K). The coldest CTT at this time was 207K for the storm at 250 km, associated with a local height maximum, but not with the absolute height maximum. It is postulated that the IR sensor is underestimating the magnitude of the convection (warm bias) for storms at the extreme upwind anvil edge. The data suggests that while points of maximum rainfall may be inferred from cloud-top height maxima (CTT minima) no unique relationship exists between all pixels at a given height (temperature) and rainfall beneath that pixel.*

## CONCLUSIONS

Analysis of individual thunderstorms in GOES IR imagery for severe weather applications requires 3 min interval data at full radiometric resolution (one degree at cold end).

The farthest upwind storm (Wichita Falls storm) was denoted by a minimum in temperature located at the apex of a "V" shaped cold area. A local warm area developed immediately downwind of this tower, ultimately attaining a temperature 12° warmer than the ascending tower at 2346 GMT.

Three explanations were proposed for the downwind warm area: an eddy formed in the wake of air diverging around the ascending tower; subsidence of air in the lee of the tower; and ejection of cirrus particles into the stratosphere.

Immediately preceding each of five distinct tornado touchdowns was a rapid cooling, then warming, of the minimum cloud-top temperature.

Small temperature changes in CTT above the tropopause may be indicative of fluctuation in storm volumetric rain rate as observed by radar.

Stereographic analysis revealed the Wichita Falls storm top to be at 14.6 $\pm$0.5 km at 2345 GMT, the highest point on the image. Minimum CTT at this time was 212K, 7° warmer than the coldest CTT; an apparent overestimate of temperature for a small feature near the upwind anvil edge.

No stereo height minimum could be found in the downwind warm area, implying no unique relationship between temperature/height above the tropopause.

Cross-sectional analysis suggests that while areas of maximum rainfall may be inferred from cloud-top height maxima, no relationship exists between all pixels at a given height and rainfall beneath that pixel.

## ACKNOWLEDGEMENTS

The authors would like to thank Dr. Robert Adler and Dr. Joanne Simpson for their continued support and suggestions, and acknowledge the expert typing of Carla Ridgeway.



☆ U.S. GOVERNMENT PRINTING OFFICE: 1982—546-071/211

Reprinted from MONTHLY WEATHER REVIEW, Vol. 108, No. 4, April 1980
American Meteorological Society
Printed in U. S. A.

# Predicting Tropical Cyclone Intensity Using Satellite-Measured Equivalent Blackbody Temperatures of Cloud Tops

R. CECIL GENTRY[1]

*Department of Physics and Astronomy, Clemson University, Clemson SC 29631*

EDWARD RODGERS

*Laboratory for Atmospheric Science (GLAS), NASA/Goddard Space Flight Center, Greenbelt, MD 20771*

JOSEPH STERANKA

*General Electric Space Division (MATSCO), Beltsville, MD 20705*

WILLIAM E. SHENK

*Laboratory for Atmospheric Science (GLAS), NASA/Goddard Space Flight Center, Greenbelt, MD 20771*

(Manuscript received 14 December 1978, in final form 17 December 1979)

ABSTRACT

A relationship between maximum winds and satellite-measured equivalent blackbody temperatures near tropical cyclones is investigated with data from both the Atlantic and western North Pacific areas. This investigation revealed not only a significant correlation between satellite-derived equivalent blackbody temperatures and maximum winds but also a strong lag relationship between these temperatures and maximum winds. From this latter relationship a regression technique was developed to forecast 24 h changes of the maximum winds for weak (maximum winds $\leq$ 65 kt) and strong (maximum winds $>$ 65 kt) tropical cyclones by utilizing the equivalent blackbody temperatures around the storm alone, and together with changes in maximum winds during the preceding 24 h and the current maximum winds. Testing of these equations with independent data showed that the mean errors of forecasts made by the equations are lower than the errors in forecasts made by persistence techniques.

## 1. Introduction

Hurricane caused damages in the United States average over $600 million per year (Gentry, 1966).[2] Damages from tropical cyclones are even much greater in many other countries on the western borders of tropical cyclone basins when expressed as a percentage of the gross national product. Forecasts of where and when a hurricane will strike are obviously of great importance.

Observations and forecasts of the maximum winds in hurricanes are also very important because damages caused by hurricanes vary exponentially with the maximum wind speeds. While the force of the wind varies with the square of the speed, some of the historical surveys of total storm damage suggest that the damage varies with a higher power of the wind speed, i.e.,

$$D = KV^n, \tag{1}$$

where $D$ (total damage) is the total damage caused by the storm, $K$ a constant, $V$ the maximum wind speed, and $n$ some number between 2 and 5 (Howard *et al.*, 1972). This relationship emphasizes the importance of knowing and predicting the intensity of a tropical cyclone. Furthermore, contrary to the improvements made in predicting tropical cyclone movement, relatively little progress has been made in the last 20 years in developing improved objective techniques for forecasting maximum winds of these storms. Except in special situations, forecasters still rely very heavily on persistence and climatological techniques when forecasting tropical cyclone intensity. As a result, operational skill in forecasting maximum wind speeds in hurricanes remains low.

In spite of the need for knowledge of tropical cyclone intensity by the hurricane forecast services, aircraft reconnaissance of these storms on the average is being reduced for economic reasons. Efforts

[1] Formerly associated with General Electric Space Division (MATSCO), Beltsville, MD 20771.

[2] Updated using records at the National Hurricane Center, Miami, Florida.

0027-0644/80/040445-11$06.75

have been increased in recent years, therefore, to use satellite data to observe and predict the intensity of tropical cyclones. Results from these efforts have been very encouraging and they keep improving as satellite data of better quality become more readily available with each new satellite series.

While satellite and other platforms usually provide sufficient information to identify the current intensity of tropical cyclones, relatively few satellite data (visible, infrared or passive microwave) have been utilized in predicting changes in intensity, and then primarily in a qualitative sense. Satellite measured equivalent blackbody temperatures ($T_{BB}$) of cloud tops in tropical cyclones are believed to contain useful information about storm intensity and expected changes of intensity. Latent heat released when the warm moist tropical air ascends in major cumulus towers of hurricanes is the primary fuel for the storms (Dunn and Miller, 1960), and its availability is indicated by the amount and vigor of the convection within the cyclone. This can be deduced from satellite $T_{BB}$ measurements.

The hurricane is a prolific producer of clouds. The convective towers build far into the troposphere and sometimes penetrate the lower stratosphere, thus producing very cold cloud tops. The high-level shearing and outward spiraling winds spread the cold cirrus over a large area beyond the region of most active convection. This air subsides as its spirals away from the storm center causing the cirrus to begin dissipating as the air warms adiabatically. These effects are easily observable in satellite imagery and can be quantified through measurement of cloud-top temperatures. Thus, areal distribution of $T_{BB}$ provides information on the extent and strength of the convection which serve as indices of the latent heat released and indicate the extent to which the clouds of the storm are organized into patterns.

The latent heat is ultimately converted to the kinetic energy which causes the extreme winds of the tropical cyclones (Riehl, 1954). For this to take place, however, complex processes are involved including, among other things, conversion of the heat to potential and available energy. Finally, the kinetic energy has to be concentrated by the flow patterns usually into relatively narrow bands, for the storm to become truly destructive. All these processes take time and there should be a lag between changes in convective activity and changes of maximum winds in the storm.

The results of theoretical-numerical model experiments simulating development and maintenance of tropical cyclones support the reasoning and suggest that maximum vertical motion, i.e., maximum convection precedes the highest winds by 1–3 days (Rosenthal, 1978; Kurihara and Tuleya, 1974). Riehl (1954) and Rosenthal (1978) have also emphasized that the convection needs to be organized by some larger scale system into a suitable pattern (e.g., spiral bands and eye-wall) before rapid intensification of the tropical cyclone takes place.

Dvorak and earlier investigators at the National Environmental Satellite Service have developed techniques to use satellite imagery to identify the present intensity of the tropical cyclone and to suggest future changes of the intensity (Dvorak, 1975; Hubert *et al.*, 1969). While these techniques have shown skill and the latest Dvorak technique is in widespread use in the tropics worldwide, it still involves considerable subjectivity especially in the forecasting of storm intensity. Dvorak (1975) utilized the degree of pattern organization to identify the current storm intensity from satellite imagery. He found that the size of the central dense overcast of cirrus and the degree to which the spiral bands of convective clouds encircled the storm center to be important factors. Others who recently have studied the relationship between satellite measurements of clouds and tropical cyclone intensity, convection or rainfall include Arnold (1977) and Griffith *et al.* (1978).

Based on the heuristic reasoning just presented, results from the theoretical experiments, results of using Dvorak's technique under operational conditions, and other research, the authors have developed a hypothesis tested by the experiments reported in this paper. It says 1) the $T_{BB}$ of the tropical cyclone cloud tops provide a measure of the convection and an index of the latent heat released for eventual conversion into kinetic energy; 2) the $T_{BB}$ areal distribution serves as an index of the organization of the storm's convective activity; and 3) the lower (higher) the mean $T_{BB}$ of the cloud tops over a moderate sized area, the stronger (weaker) and more (less) persistent is the convection and the more likely that the maximum winds in the storm will increase (decrease) with time.

## 2. The data and the analysis

The infrared (11.5 $\mu$m, window channel) $T_{BB}$ for a number of tropical cyclones over open ocean areas were analyzed using data from the western Atlantic for 1969 and the western Pacific for 1970, 1973 and 1974. The 1969 $T_{BB}$ were measured by the Medium Resolution Infrared Radiometer (MRIR) sensor on Nimbus 3 with a spatial resolution of 55 km at nadir. Those in 1970, 1973 and 1974 were measured by the Temperature Humidity Infrared Radiometer (THIR) sensor on Nimbus 4 and 5 with a spatial resolution of 8 km at the subpoint. Further details of the Nimbus 3, 4 and 5 satellites and their instrumentations are provided in the Nimbus 3, 4 and 5 *User's Guides* (Nimbus Project 1969, 1970, 1972). These data were analyzed using the scheme illustrated

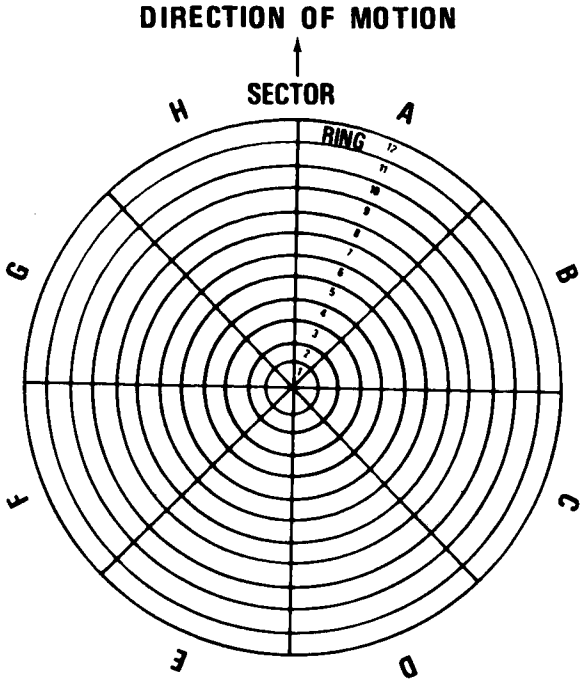


FIG. 1. Grid used in analyzing the temperature data. The concentric rings are spaced 111 km apart. The center of this grid coincides with the center of the tropical cyclone.

in Fig. 1 in order to obtain a measure of the intensity, expanse and organization of the storm. The concentric circles are 111 km apart and the rings they bound are numbered outward from 1 to 12. The mean $T_{BB}$ was computed for each ring with the center of the diagram coinciding with the center of the storm. In addition, the mean $T_{BB}$ was calculated for each octant of each ring (hereafter referred to as a sector) with the top of the diagram being oriented both toward the north and also along the direction of motion of the storm.[3] To get a further measure of how well the convective towers were distributed symmetrically and concentrated about the storm center, the standard deviations of the mean sector temperatures were computed for rings 1–5 and for various combinations of rings. With these data it is feasible to study the expanse and also the organization of the storm as well as the intensity of the convection.

The wind data for each Atlantic storm were obtained from the best track records maintained at the National Hurricane Center. The wind data for each Pacific storm were obtained from the best track and warning information compiled by the Joint Typhoon Warning Center, Guam (U.S. Fleet Weather Central, Joint Typhoon Warning Center, 1970, 1973, 1974). A linear interpolation of wind was made when satellite observation time occurred between the best track data times.

### 3. $T_{BB}$ and storm intensity

The first tests made in this investigation were with 1969 Atlantic tropical cyclones. This investigation determined how well the cloud top $T_{BB}$ demonstrated an index of convection. The mean data for the rings composited for 16 hurricanes are compared with similar data for 19 storms of less than hurricane intensity (three of the tropical cyclones were still at depression stage) in Fig. 2. For rings 1–4 (Fig. 1) the mean $T_{BB}$ were 7–10°C lower in the hurricanes than in the weaker storms, but in rings

[3] Since all results reported in this paper used the entire ring of data, storm orientation is of no concern.

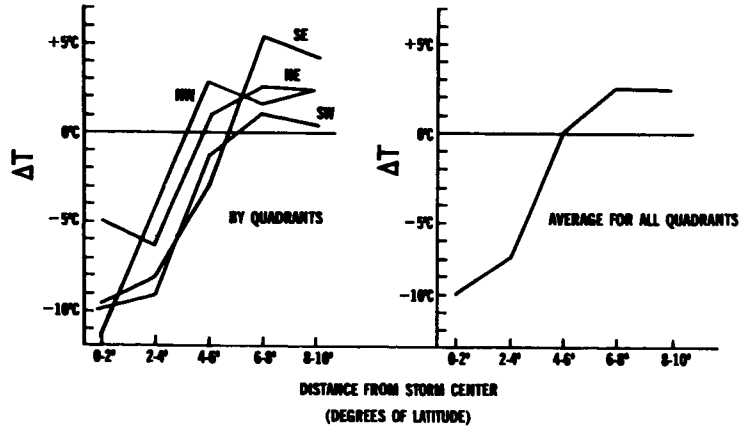


FIG. 2. Comparison of mean temperatures of cloud tops around 16 hurricanes with mean temperatures from 19 storms of less than hurricane intensity, all in 1969. The tropical cyclones all occurred in the western North Atlantic in 1969. The $\Delta T$ values are positive when the temperatures in the hurricanes are higher.

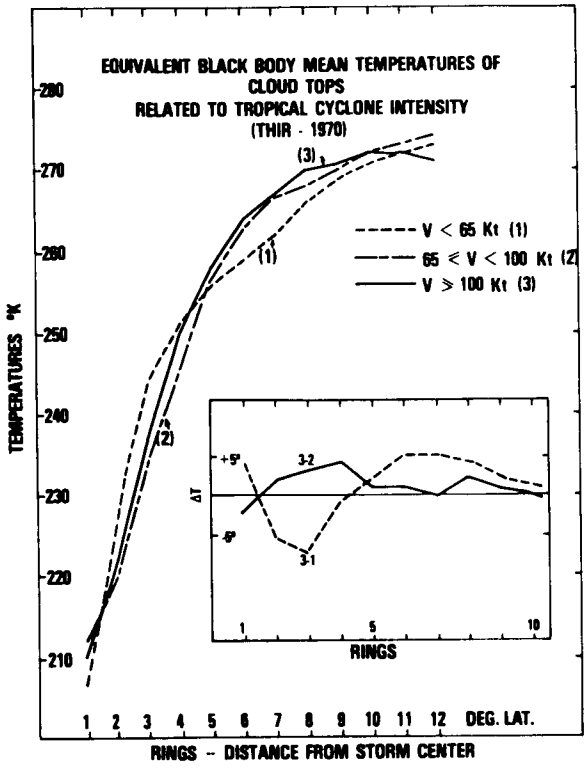


FIG. 3. Comparison of mean temperatures of cloud tops around 1970 tropical cyclones of the western North Pacific: 15 storms with maximum winds < 65 kt (broken line); 13 typhoons with maximum winds < 100 kt (dashed-dotted line); and 14 typhoons with maximum winds equal or > 100 kt (solid line). The insert contains graphs of the differences in temperatures of the latter and the two weaker categories. The rings are illustrated in Fig. 1.

6–10, the hurricanes had higher mean $T_{BB}$. That is, the $T_{BB}$ imply that hurricanes have stronger convection near the core and stronger subsidence in the environment surrounding the storm. Both the convective and subsidence areas have been observed frequently by aircraft reconnaissance and in satellite imagery (Shenk and Rodgers, 1978). The subsidence dissipates many of the clouds at distances > 650 km from the center and the higher mean $T_{BB}$ in these regions are observed because the satellite sensor measures the $T_{BB}$ of the sea surface in areas of no clouds.

A similar test was made with the 1970 Pacific Ocean tropical cyclones. The composited mean $T_{BB}$ for 14 typhoons (current maximum wind $V_0 \geq 100$ kt), 13 typhoons (65 kg $\leq V_0 <$ 100 kt) and 15 weaker storms ($V_0 < 65$ kt) are compared in Fig. 3. The comparison between the weak storms and those with maximum winds > 99 kt is similar to that of the 1969 Atlantic storms except for ring 1 where the $T_{BB}$ for typhoons are higher. This reflects the large cloud-free eyes of several of the typhoons and the fact that the Nimbus 4 THIR had higher resolution than the Nimbus 3 MRIR. If values for ring 1 are ignored, intense storms are again colder for the inner four rings and warmer at greater radii (dashed line, Fig. 3 insert).

The comparison between the typhoons of moderate intensity with the very intense typhoons (solid line, Fig. 3 insert), however, gave contradictory information. An examination of the individual cases involved showed the moderate intensity storms were biased toward intensification and the intense storms toward weakening or little change. This is especially significant because it suggests that the mean $T_{BB}$ are also an index of the rate of change of storm intensity.

The relationship of $T_{BB}$ to rate of change of storm intensity was investigated by stratifying the storms according to wind intensity changes. Fig. 4 shows composited $T_{BB}$ means for cyclones stratified according to intensity changes during the succeeding 24 hours. Four categories are used: 1) intensifying ($V_0$ increase ≥ 10 kt), 12 cases; 2) weakening

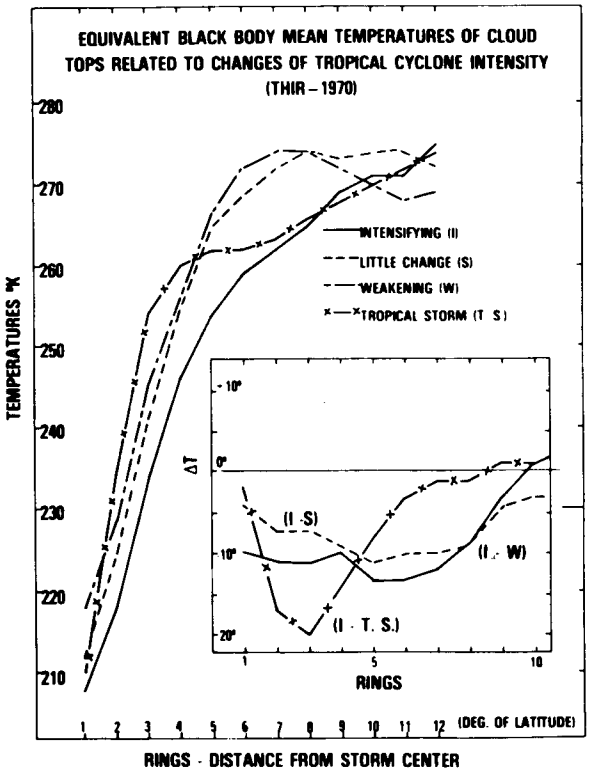


FIG. 4. As in Fig. 3 except that the data are stratified according to change of intensity during next 24 h: maximum winds increasing 10 or more kt (I), maximum winds changing less than 10 kt (S), maximum winds decreasing 10 or more kt (W), and storms which never reached hurricane intensity (T.S.). Only storms located south of 30°N were included. The insert shows that the intensifying storms have much colder cloud tops within 8° (888 km) of the storm center than the others.

($V_0$ decrease $\geq$ 10 kt), four cases; 3) little change ($V_0$ change $<$ 10 kt), six cases; and 4) five tropical cyclones which did not reach typhoon intensity. The cases in categories 1, 2 and 3 all reached typhoon intensity. We can note that the storms with the greater rate of intensification are associated with the lower mean $T_{BB}$ in all rings outward through ring 9. The intensifying storms are ~18 K colder in rings 2–4 than the storms that never reached typhoon intensity, ~10 K colder in rings 1–8 than the weakening storms and 5–10 K colder than the storms with little change in intensity.

The time lag between the mean $T_{BB}$ and maximum wind of several tropical cyclones examined further supports the hypothesis that $T_{BB}$ serves as a predicator of wind changes. Fig. 5 illustrates a time lag between the $T_{BB}$ and the change of the maximum winds in 1970 Pacific Typhoons Billie and Hope. The lowest mean $T_{BB}$, which may be said to represent maximum convection, of Billie occurred two days before the wind maximum was reached and that of Hope occurred more than one day prior to the wind maximum. Similar data examined in other storms suggest that the wind changes lag the $T_{BB}$ changes by 24–36 h.

Fig. 6 is adapted from a simulation experiment with a theoretical model by Rosenthal (1978). The vertical velocities at 900 mb and the maximum winds are plotted against time. Here vertical velocity, rather than temperature as in Fig. 5, represents convection. There is a striking similarity in the time lag between maximum convection and the maximum winds of the storm in the two illustrations.

The results of these comparisons of the mean $T_{BB}$ and storm intensity strongly suggest that the cloud top $T_{BB}$ near the tropical cyclone center may serve as an index for both 1) current storm intensity, and 2) future storm intensity. This dual relationship is further explored in the succeeding section where equations are developed for predicting storm intensities 24 h in advance.

## 4. Development of predictive equations

Results of the analyses reported in Section 3 demonstrate that both current and future storm intensities are a function of the mean $T_{BB}$. These results also suggest that the relationship between the mean $T_{BB}$ and the future intensity varies with at least the latitude of the storm, season of the year, sea temperatures, lapse rate in the ambient atmosphere and past changes in storm intensity. Therefore, it appears there is a need to either stratify the data into several classes or use several predictors to account for the various effects.

The limited number of cases for which good data were available emphasized the need, however, for special care in selection of techniques used in developing the predictive equations. Instead of using a strictly statistical approach in seeking a solution, potential predictors were preselected after use of a combination of physical reasoning based on re-

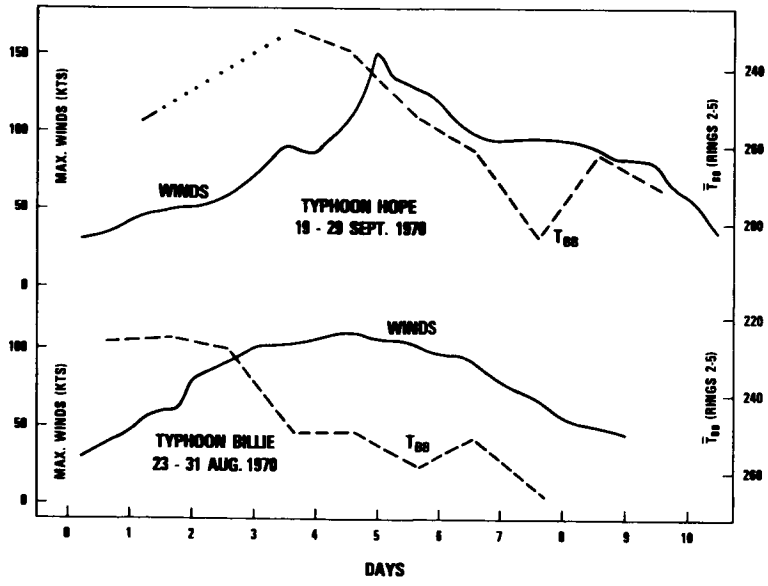


FIG. 5. Temporal changes of mean equivalent blackbody temperatures (rings 2–5, Fig. 1) and maximum winds of Typhoons Hope (September 1970) and Billie (August 1970). The maximum wind changes lag the temperature changes in both cases. The temperature scale is inverted to show the lower temperatures at the top of the graph.

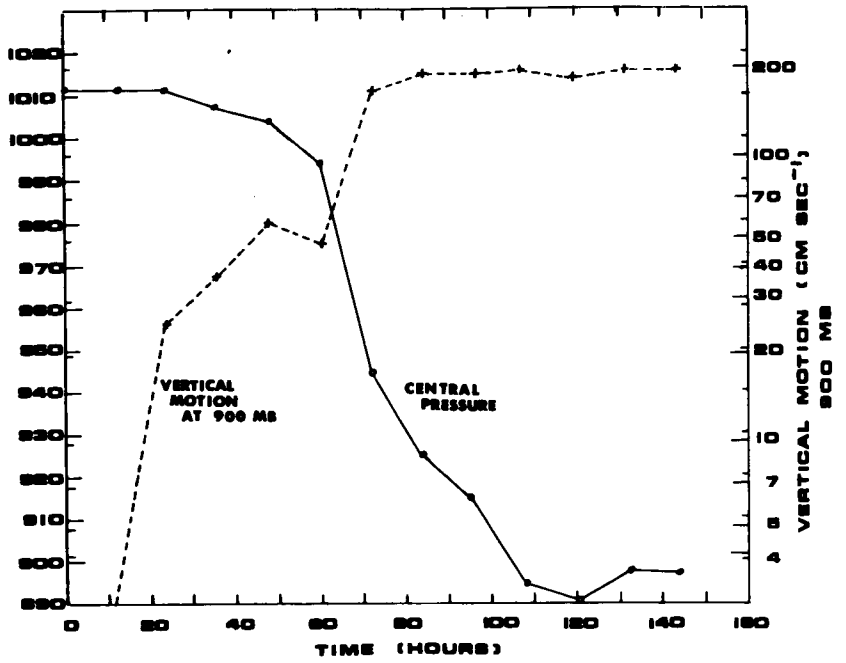


FIG. 6. Comparison of vertical motion and central pressure in a model hurricane showing lag with time (Rosenthal, 1978).

sults of research on tropical cyclones of the last 20 years and statistical type analyses such as those presented in Section 3. Furthermore, because of the concern that the use of a large number of predictors in the equations would lead to unstable solutions which would provide poor forecasts when the predictive equations were applied to independent data, the arbitrary decision was made that not more than four predictors would be used.[4] This required special care in selecting the predictors. The mean $T_{BB}$ parameter to be used in each case was identified by examining data arranged in a systematic fashion (e.g., such as in Fig. 4) or by study of previously calculated correlation coefficients.

It was believed that by using only predictors that seem to have a close physical relationship with the parameter to be predicted that the predictive equations developed with even a relatively few cases would likely be stable and apply to other storms. To further insure that the predictors selected on the basis of physical reasoning and statistical deductions were truly related with the parameter to be predicted and not just correlated by chance, all forecast equations developed were tested with independent data (i.e., data not used in the preliminary analyses to preselect the predictors nor used in the development of the regression equations).

[4] In equations tested and used in this report, three predictors at most were used.

Besides the mean $T_{BB}$ parameter, the current maximum wind ($V_0$) and the change in maximum winds during the preceding 24 h ($\Delta V_{-24}$) were used as predictors. In addition, parameters putting additional emphasis on the degree of organization of the convection were considered in some of the equations. This was usually a parameter measuring the variability of the mean $T_{BB}$ in one or more of the rings ($\sigma_{n,m}$, where the subscripts refer to the identifiers of rings). Once the predictors had been preselected, a modified screening regression approach was used in developing the equations in order to determine which of the terms contributed most and also to determine just how much reduction in variance occurred as each new predictor was added to the equation.

Stratification of the storms into two groups ($V_0 \leq 65$ kt and $V_0 > 65$ kt) produced better results than single grouping of all storms. Fifty-eight cases from the 1970 western North Pacific tropical cyclones were used as dependent data for developing the following equations. The first three regression equations are:

$$\text{Weak storms} \quad \Delta V_{+24_w} = 143.75 - 0.594\bar{T}_{2,3} + 0.389\Delta V_{-24} \quad (2)$$

$$\text{Strong storms} \quad V_{+24_s} = 227.86 - 0.76\bar{T}_{1,2,3} + 0.499\Delta V_{-24} + 0.398V_0 \quad (3)$$

All storms $$V_{+24_a} = 146.6 - 1.669\sigma_{1,2} + 0.855V_0 - 0.513\bar{T}_1. \quad (4)$$

Because of the strength of the relationship of $V_{+24}$ with the satellite measured mean $T_{BB}$, several equations were developed for use with satellite data alone:

Strong storms $$V_{+24_s} = 378.51 - 1.225\bar{T}_{1,2,3} \quad (5)$$

Strong storms $$V_{+24_s} = 390.72 - 1.246\bar{T}_{1,2,3} - 0.506\sigma_3 \quad (6)$$

Weak storms $$\Delta V_{+24_w} = 167.16 - 0.682\bar{T}_{2,3} \quad (7)$$

All storms $$V_{+24_a} = 200.51 - 2.213\sigma_{1,2} - 0.381\bar{T}_{2,3}. \quad (8)$$

Here the symbols are defined as follows:

- $\Delta V_{+24_w}$ predicted change in maximum wind speed (kt) during a 24 h period after satellite observation for storm whose current maximum winds are ≤65 kt
- $V_{+24_s}$ predicted maximum wind speed (kt) 24 h after satellite observation for storm whose current maximum winds are >65 kt
- $V_{+24_a}$ predicted maximum wind speed (kt) 24 h after satellite observation for storms of any intensity
- $\bar{T}_1$ mean $T_{BB}$(K) for area 0–111 km about the storm center (ring 1)
- $\bar{T}_{2,3}$ mean $T_{BB}$(K) for area 111–333 km about the storm center (rings 2 and 3)
- $\bar{T}_{1,2,3}$ mean $T_{BB}$(K) for area 0–333 km about the storm center (rings 1, 2 and 3)
- $\Delta V_{-24}$ change in maximum wind speeds (kt) of the storm during the 24 h preceding satellite observation
- $V_0$ the current maximum wind speed (kt) in the storm at the time of satellite observation
- $\sigma_{1,2}$ the standard deviation (K) of the mean $T_{BB}$ of all sectors contained in rings 1 and 2
- $\sigma_3$ the standard deviation (K) of the mean $T_{BB}$ of all sectors contained in ring 3.

TABLE 1. Correlation coefficients for weak storm cases dependent data (independent data).

| | $V_{+24}$ | $\Delta V_{+24}$ | $V_0$ | $\Delta V_{-24}$ |
|---|---|---|---|---|
| $\bar{T}_{2,3}$ | −0.547 (−0.472) | −0.647 (−0.300) | −0.068 (−0.273) | −0.291 (0.393) |
| $\Delta V_{-24}$ | 0.504 (0.482) | 0.450 (0.213) | | |
| $V_0$ | 0.625 (0.465) | 0.177 (0.275) | | 0.304 (0.398) |

Reduction in variance of $\Delta V_{+24_w}$ dependent data

| Predictors | $\bar{T}_{2,3}$ | $\bar{T}_{2,3}$; $\Delta V_{-24}$ |
|---|---|---|
| Reduction in variance | 0.42 | 0.49 |

TABLE 2. Correlation coefficients for strong storms dependent data (independent data).

| | $V_{+24}$ | $\Delta V_{+24}$ | $V_0$ | $\Delta V_{-24}$ |
|---|---|---|---|---|
| $\bar{T}_{1,2,3}$ | −0.781 (−0.725) | −0.589 (−0.642) | −0.392 (−0.274) | −0.489 (−0.548) |
| $\sigma_3$ | −0.056 | −0.286 | −0.197 | −0.407 |
| $\Delta V_{-24}$ | 0.662 (0.697) | 0.655 (0.446) | 0.130 (0.475) | |
| $V_0$ | 0.551 (0.556) | −0.191 (−0.144) | | 0.130 (0.475) |

Reduction in variance of $V_{+24_s}$ dependent data

| Predictors | $\bar{T}_{1,2,3}$ | $\bar{T}_{1,2,3}$; $\Delta V_{-24}$ | $\bar{T}_{1,2,3}$; $\Delta V_{-24}$; $V_0$ |
|---|---|---|---|
| Reduction in variance | 0.61 | 0.71 | 0.77 |

Table 1 lists the correlations between the various parameters used as predictors with the quantities to be predicted, and with each other for the weaker storms. Table 2 lists the correlation data for intense storms. Eqs. (2) and (7) were developed to predict the change in maximum wind speeds during the next 24 h rather than the maximum wind speed for two reasons: 1) the correlation between $\bar{T}_{2,3}$ was higher with $\Delta V_{+24}$ than with $V_{+24}$ and 2) in the typhoon service, operational procedures are such that for weak storms the forecaster is believed in many cases to have a better estimate of whether a storm is intensifying than of the absolute value of the maximum winds. Of course, by adding $V_0$ to both sides of the equations, one can put them in the same format as the other equations.

The great value of Eqs. (4)–(8) is that no past history of the storm is needed. This provides a means of making reliable forecasts over isolated ocean basins. The current satellite imagery can be used for a general classification (over/under 65 kt) and the infrared data may be used to develop the necessary $T_{BB}$ parameters. By using the Dvorak technique (Dvorak, 1975), one can also obtain $V_0$ from satellite data [Eq. (4)].

Errors of forecasts made with the equations were compared with those obtained by techniques frequently used in tropical cyclone intensity forecasting: persistence (NC) [assumes no change during the forecast period], and persistence of change (P) [assumes the change during forecast period is the same rate as the change during the preceding period]. Results of this comparison for both the dependent and independent data series are summarized in Table 3. The independent series were from the 1973 and 1974 western North Pacific tropical cyclones.

## 5. Discussion of results

In the weak tropical cyclone set, Table 3 reveals that Eqs. (2) and (7) produce better forecast results compared to those from persistence techniques not only for the dependent data which would be expected but also for the independent data sets. The difference between regression and persistence (NC)

TABLE 3. Mean errors of forecasts.

| Equation | Dependent data (1970 storms) | | | | Independent data (1973 and 1974 storms) | | | |
|---|---|---|---|---|---|---|---|---|
| | $n$ | E | E − NC | E − P | $n$ | E | E − NC | E − P |
| Weak tropical cyclones ($V_0 \leq 65$ kt) | | | | | | | | |
| 2 | 24 | 8.6 | −4.0 | −4.2 | 33 | 12.6 | −4.2* | −0.6 |
| 4 | 24 | 10.2 | −2.4 | −2.6 | 33 | 14.2 | −2.4 | 1.0 |
| 7 | 24 | 9.6 | −3.0 | −3.2 | 33 | 12.8 | −4.0* | −0.4 |
| 8 | 24 | 24.9 | 12.3 | 12.1 | 33 | 25.0 | +8.2 | +11.8 |
| Intense tropical cyclones ($V_0 > 65$ kt) | | | | | | | | |
| 3 | 34 | 9.4 | −7.5 | −2.6 | 20 | 16.1 | −3.1 | −6.9* |
| 3 (−11 kt) | | | | | 20 | 11.8 | −7.4* | −11.2* |
| 4 | 34 | 12.1 | −4.8 | 0.1 | 20 | 14.7 | −4.5* | −8.3** |
| 5 | 34 | 11.4 | −5.5 | −0.6 | 20 | 18.8 | 2.0 | 5.6 |
| 5 (−11 kt) | | | | | 20 | 15.6 | −3.6 | −7.4* |
| 6 | 34 | 10.8 | −6.1 | −1.2 | 20 | 18.7 | 1.9 | 5.5 |
| 6 (−11 kt) | | | | | 20 | 14.9 | −4.3 | −8.1* |
| 8 | 34 | 21.1 | 4.2 | 9.1 | 20 | 17.4 | −1.8 | −5.6 |
| All storms | | | | | | | | |
| 2 & 3 | 58 | 9.1 | −6.0 | −3.2 | 53 | 13.9 | −3.8* | −3.0** |
| 4 | 58 | 11.4 | −3.7 | −0.9 | 53 | 14.4 | −3.3* | −2.5 |
| 8 | 58 | 22.7 | 7.6 | 10.4 | 53 | 22.1 | 4.4 | +5.2 |

Notes: E is mean error of forecasts made by indicated regression equation.
E − NC is mean difference in errors of forecasts made by regression equation and by assuming no change in wind speed during forecast period.
E − P is mean difference in errors of forecasts made by regression equation and by assuming the change in wind speed in the next 24 h would be the same as the change during the previous 24 h.
* Differences significant at 1% level.
** Differences significant at 5% level.

results in the independent data set is significant at the 1% level. Eq. (8) yielded only fair results; Eq. (4), however, produced strikingly good results considering that satellite data alone were used in forecast parameters[5] and that this equation applied to both weak and strong storms.

The intense tropical cyclone [Eqs. (3), (5) and (6)] provide good forecasts in the dependent data set but only Eq. (3) gives results better than persistence with the independent data set. However, a bias (see Section 6) is believed to exist in the wind information of the independent set and causes the intensity forecasts by the regression equations to be about 11 kt too high in the mean. When this bias is removed from the forecasts for the independent data set, Eqs. (3), (5) and (6) are better than persistence. Significance at the 1% level is prominent in several comparisons. Eq. (4) shows superiority even without the bias removed.

For all storms combined Eq. (4) gives better results than persistence techniques. They are only slightly weaker than results from Eqs. (2) and (3) combined. This is particularly significant in that forecasts from Eq. (4) can be made using only satellite data. Eq. (8) does not produce results of comparable quality.

The regression equations for the intense and weak tropical cyclones have yielded results throughout the dependent data set which are −0.1 to 7.5 kt better than the persistence results [Eq. (8) excepted]. The independent data set results are −5.6 to 8.3 kt better. When the bias error is applied for Eqs. (3), (5) and (6) in the independent data set the regression results are 3.6–11.2 kt better than the persistence results.

One of the objectives of this investigation was to determine whether the mean $T_{BB}$ were strongly related to the current and future wind speeds and whether they had predictive value. The fact that the regression equations outperform persistence for the independent series suggests that the $T_{BB}$ do contain predictive information over and above that contained in the current and previous wind data. Nevertheless, the fact that equations using $\Delta V_{-24}$ and $V_0$ produced superior forecasts to those which used only the mean $T_{BB}$ and its derivatives, makes it pertinent to ask if the skill shown in Eqs. (2), (3) and (4) is primarily due to the use of wind information. The answer to this question is contained in Tables 1 and 2.

For the weak storms in the dependent data series,

[5] Assumes that $V_0$ can be obtained by the Dvorak or some similar technique.

the highest correlation with the winds was between $\bar{T}_{2,3}$ and $\Delta V_{+24}$. For the independent data the highest correlations was with $V_{+24}$ and there were relatively little difference in correlations between it and with $\bar{T}_{2,3}$, $\Delta V_{-24}$ or $V_0$. The reduction in variance was 0.42 when $\bar{T}_{2,3}$ was the sole predictor. Adding $\Delta V_{-24}$ as a predictor increased the reduction in variance to 0.49.

$\bar{T}_{2,3}$ is poorly correlated with $\Delta V_{-24}$ in the weak series so they should contribute independently to the skill of the regression equation. Note that the sign of this correlation changes between dependent and independent data.

For the strong storms dependent data (Table 2) the correlation between $\bar{T}_{1,2,3}$ with $V_{+24}$ (−0.781) is stronger than that between $V_{+24}$ and either $\Delta V_{-24}$ (0.662) or $V_0$ (0.551). While the correlation between $\bar{T}_{1,2,3}$ and either $V_0$ or $\Delta V_{-24}$ is considerably higher than for the weak storms, these correlations are still lower than the correlations between $\bar{T}_{1,2,3}$ and either $V_{+24}$ or $\Delta V_{+24}$ (−0.781 and −0.589 vs −0.392 and −0.489) data. These relationships also hold for the independent data.

In the tests of significance of the differences in the errors by the regression equations and the errors by persistence techniques, consideration was given to the size of the samples of the independent data. There were 33 cases for the weak category selected from 20 different storms from two years. There were 20 cases for the strong category selected from 9 different storms from two years. Most of the cases from the same storm were spaced at intervals $\geq$ 24 h. There were, however, five cases from one storm and three cases from another storm in the strong sample which were approximately at 12 h intervals. For the weak storms there were five storms that contributed two cases and one storm that contributed three cases where the interval was approximately 12 h. Examination of these cases revealed that the standard deviation of the errors of the regression forecasts were much larger for the strong storm cases with the 12 h intervals than for the entire sample. For the weaker storms there was little difference between the standard deviation of the errors for the cases of 12 h intervals and for the entire sample. That is, the data from the individual cases were sufficiently convincing that there was relatively little autocorrelation between the storm cases spaced at 12 h intervals and their inclusion did not alter the effective sample size.

## 6. Bias in forecast results

The forecast results from Eq. (3) are better for the independent data than those obtained from persistence. However, examination of the errors reveals that the regression equation forecasts maximum winds 11.3 kt too high in the mean for the independent cases of 1973 and 1974. This bias was calculated by taking the algebraic mean[6] of the forecast errors. The equations and data were tested to determine the cause of the bias. The following were checked for possible biasing effects: 1) satellite sensor calibration variation; 2) time of year of storm occurrence; 3) location of storm; and 4) operation and best track estimates of maximum wind speeds.

To check the sensitivity of results from the equations to possible bias corrections, the constant term of Eq. (3) was reduced by various amounts ranging from 8 to 17 kt. This variation caused only minor variations in the mean of the absolute values of the errors for the independent series (12.7–11.6 kt which compares with 16.1 kt when no bias was applied). This suggests that a bias correction in the range 8–17 kt that was well substantiated might be used to adjust the constant in Eq. (3) when it was used with data from the 1973 and 1974 seasons. Other equations were tested with similar results.

The biasing effect caused by using $T_{BB}$ observations from different satellites was minimum. The upper and lower limits of the mean $T_{BB}$ values and their range in the tropical cyclones as measured in the storms by Nimbus 3, 4 and 5 agreed within $\ll$2°C.

Seasonal, latitudinal and longitudinal variation between the dependent and independent data sets resulted in differences which would account for only a few knots (−2 to 4 kt) difference in forecast for the dependent and independent data and even then only for a few storms. The effect of these factors is not believed, therefore, to be of sufficient magnitude to account for the large bias found to exist.

The operational estimates of maximum wind, however, could account for the bias. Atkinson and Holliday (1977) discuss the "considerable uncertainty involved in existing equations" for estimating maximum winds and report changes in procedures at the Joint Typhoon Warning Center at Guam (JTWC) that may affect results of our experiment. Table 4 compares the maximum wind calculated for a range of central pressures ($P_c$) from the following three equations (Atkinson and Holliday, 1977):

Equation by Atkinson and Holliday

$$V_{m_1} = 6.7(1010 - P_c)^{0.644} \tag{9}$$

Equation by Takahashi

$$V_{m_2} = 13.4(1010 - P_c)^{0.5} \tag{10}$$

Equation by Takahashi (high lat.)

$$V_{m_3} = 11.5(1010 - P_c)^{0.5}. \tag{11}$$

Here $P_c$ is the central pressure (mb) of the storm and $V_m$ the maximum wind speed (kt). When these

[6] The errors listed in Table 3 are all means of absolute values of individual errors.

TABLE 4. Relations between minimum central pressure and maximum winds in tropical cyclones.

| $P_c$ | $V_{m_1}$ | $V_{m_2}$ | $V_{m_3}$ |
|---|---|---|---|
| 1000 | 30 | 42 | 36 |
| 990 | 46 | 60 | 51 |
| 980 | 60 | 73 | 63 |
| 970 | 72 | 85 | 73 |
| 960 | 83 | 95 | 81 |
| 950 | 94 | 104 | 89 |
| 940 | 103 | 112 | 96 |
| 930 | 113 | 120 | 103 |
| 920 | 122 | 127 | 109 |
| 910 | 130 | 134 | 115 |
| 900 | 138 | 141 | 121 |
| 890 | 146 | 147 | |

equations are applied to the independent data set cases the mean difference between the results from Takahashi's and Atkinson and Holliday's equations is near 10 kt. Holliday[7] reports that Eq. (9) was used for developing most of the "best track" information for the 1973 and 1974 years while Eqs. (10) and (11) were used in 1970. These results suggest that the changes in procedures at JTWC for estimating wind maxima may account for most of the bias found.

To further test the hypothesis that the bias is due to change in procedures for obtaining maximum winds, the 1973, 1974 data were used dependently to develop equations similar to Eqs. (3) and (6). These new equations

$$V_{+24_i} = 243.91 - 0.885\bar{T}_{1,2,3} + 0.385\Delta V_{-24} + 0.424V_0, \quad (12)$$

$$V_{+24} = 395.3 - 1.333\bar{T}_{1,2,3} - 0.404_{\sigma_3}, \quad (13)$$

were substracted from Eq. (3) and (6), respectively, and the results simplified to provide

$$V_{+24_s} - V_{+24_i} = 8.5 + 0.125(\bar{T}_{1,2,3} - 210) + 0.114\Delta V_{-24} - 0.026(V_0 - 65), \quad (14)$$

$$V_{+24_s} - V_{+24_i} = 13.078 + 0.087(\bar{T}_{1,2,3} - 210) - 102(\sigma_3 - 6). \quad (15)$$

When Eq. (14) is solved using representative values ($\bar{T}_{1,2,3}$ = 230 K, $V_0$ = 90 kt) the result is 10.9 kt. When Eq. (15) is solved using representative values ($\bar{T}_{1,2,3}$ = 230 K, $\sigma_3$ = 10 K) the result is 13.7 kt. Forecasts made by Eq. (3) with the constants reduced by 11.3 and those made with Eq. (12) have a correlation coefficient of 0.99. These various numbers compare favorably with the 11.3 kt bias found and are all within the range 8–17 kt. Thus, the results lend strong support to the contention that much of the bias in Eq. (3) exist due to the change in procedures for estimating wind maxima when preparing the "best track" information at JTWC.

[7] Personal communication.

## 7. Simulated operational test results

Simulated operational tests were made using the regression equations (2), (3) and (4). Wind data from typhoon advisories for the 1973, 1974 storms were incorporated as input parameters in place of best track winds. The results produced even greater increases in errors in persistence forecasts than in the regression forecasts. The regression results could not be readily compared with the JTWC forecasts for these test cases. JTWC advisory (forecast) times did not coincide exactly with satellite observation times and not all JTWC forecasts were available. To the extent information was available, it was possible to determine that the JTWC forecast errors of the test cases greatly exceeded their mean absolute error of 13.5 kt for the entire 1973 and 1974 seasons. The JTWC forecast errors were also larger than the mean errors of the regression equations for the cases where adequate comparisons could be made. It appears from these results as well as those discussed in Section 5 that the regression equations will yield better forecasts than other techniques being used.

## 8. Conclusions

This investigation demonstrated that there is a strong relationship between satellite measured $T_{BB}$ of cloud tops near the core of the tropical cyclones and both the current and future storm intensity. This was demonstrated for four different seasons of data (one in the Atlantic and three in the Pacific area). The statistical correlation, moreover, reveals that the future intensity ($V_{+24}$) is more closely related than the current intensity ($V_0$) to the mean $T_{BB}$ (correlation −0.781 vs 0.392, Table 2).

The regression equations provided forecasts superior to those of persistence techniques when applied to independent data. The equations produced better results than other techniques in simulated operational tests. The results are sufficiently convincing to warrant use of the equations as experimental forecast tools. It is particularly important that such good results are obtained from quantified $T_{BB}$ data, a parameter readily obtainable from a single satellite observation.

Further testing is recommended before implementing the technique in operational forecasting routines because of the limited sample size which was available in this investigation. It would be desirable to expand the investigation to include more cases as well as other tropical cyclone basins. The data contained in this report appear convincing,

however, that there is a relationship between $T_{BB}$ and future maximum winds in tropical cyclones that is strong enough to have predictive value.

## REFERENCES


Arnold, E. P., 1977: Tropical cyclone cloud and intensity relationships. Atmos. Sci. Paper No. 277, Colorado State University, 154 pp.

Atkinson, G. D., and C. R. Holliday, 1977: Tropical cyclone minimum sea level pressure/maximum sustained wind relationship for the western North Pacific. *Mon. Wea. Rev.*, **105**, 421–427.

Dvorak, V. R., 1975: Tropical cyclone intensity analysis and forecasting from satellite imagery. *Mon. Wea. Rev.*, **103**, 420–430.

Dunn, G. E., and B. I. Miller, 1960: *Atlantic Hurricanes*. Louisiana State University Press, 123 pp.

Gentry, R. C., 1966: Nature and scope of hurricane damage. *Proceedings Hurricane Symposium*, Amer. Soc. Oceanogr., 229–254.

Griffith, C. G., W. L. Woodley, P. G. Grube, D. W. Martin, J. Stout and D. N. Sikdar, 1978: Rain estimation from geosynchronous satellite imagery—visible and infrared studies. *Mon. Wea. Rev.*, **106**, 1153–1171.

Howard, R. A., J. E. Matheson and D. W. North, 1972: The decision to seed hurricanes. *Science*, **176**, 1191–1201.

Hubert, L. A., A. Timchalk and S. Fritz, 1969: Estimating maximum wind speed of tropical storms from high resolution infrared data. ESSA Tech. Rep. NESC50, 33 pp.

Kurihara, Y., and R. E. Tuleya, 1974: Structure of a tropical cyclone developed in a three-dimensional numerical simulation model. *J. Atmos. Sci.*, **31**, 893–919.

*Nimbus 3 User Guide*, 1969: Nimbus Project, National Space Science Data Center, Goddard Space Flight Center, Greenbelt, MD, 237 pp.

*Nimbus 4 User Guide*, 1970: Nimbus Project, National Space Science Data Center, Goddard Space Flight Center, Greenbelt, MD, 214 pp.

*Nimbus 5 User Guide*, 1972: ERTS/Nimbus Project, National Space Science Data Center, Goddard Space Flight Center, Greenbelt, MD, 162 pp.

Riehl, H., 1954: *Tropical Meteorology*. McGraw-Hill, 392 pp.

Rosenthal, L., 1978: Numerical simulation of tropical cyclone development with latent heat release by the resolvable scales. I: Model description and preliminary results. *J. Atmos. Sci.*, **35**, 258–271.

Shenk, W. E., and E. B. Rodgers, 1978: Nimbus 3/ATS 3 observations of the evolution of Hurricane Camille. *J. Appl. Meteor.*, **17**, 453–476.

U.S. Fleet Weather Central/Joint Typhoon Warning Center, 1970: Annual Typhoon Report. U.S. Navy Report, Guam, 220 pp.

——, 1973: Annual Typhoon Report. U.S. Navy Report, Guam, 94 pp.

——, 1974: Annual Typhoon Report, U.S. Navy Report, Guam, 113 pp.